



1-1-2023

The Impacts Of Airborne Cloud Microphysical Instrumentation Mounting Location On Measurements Made During The Observations Of Aerosols And Clouds And Their Interactions (ORACLES) Project

Joseph Robert O'Brien

[How does access to this work benefit you? Let us know!](#)

Follow this and additional works at: <https://commons.und.edu/theses>

Recommended Citation

O'Brien, Joseph Robert, "The Impacts Of Airborne Cloud Microphysical Instrumentation Mounting Location On Measurements Made During The Observations Of Aerosols And Clouds And Their Interactions (ORACLES) Project" (2023). *Theses and Dissertations*. 5322.
<https://commons.und.edu/theses/5322>

This Dissertation is brought to you for free and open access by the Theses, Dissertations, and Senior Projects at UND Scholarly Commons. It has been accepted for inclusion in Theses and Dissertations by an authorized administrator of UND Scholarly Commons. For more information, please contact und.common@library.und.edu.

THE IMPACTS OF AIRBORNE CLOUD MICROPHYSICAL INSTRUMENTATION
MOUNTING LOCATION ON MEASUREMENTS MADE DURING THE
OBSERVATIONS OF AEROSOLS AND CLOUDS AND THEIR INTERACTIONS
(ORACLES) PROJECT

by

Joseph Robert O'Brien

Bachelor of Science, Millersville University, 2013

Master of Science, University of North Dakota, 2016

A Dissertation

Submitted to the Graduate Faculty

of the

University of North Dakota

in partial fulfillment of the requirements

for the degree of

Doctor of Philosophy

Grand Forks, North Dakota

August

2023

Copyright 2023 Joseph R. O'Brien

This dissertation, submitted by Joseph R. O'Brien in partial fulfillment of the requirements for the Degree of Doctor of Philosophy from the University of North Dakota, has been read by the Faculty Advisory Committee under whom the work has been done and is hereby approved.

David J. Delene – Chairperson

Michael R. Poellot

Greg M. McFarquhar

Andrew Detwiler

Frank Bowman

This dissertation is being submitted by the appointed advisory committee as having met all of the requirements of the School of Graduate Studies at the University of North Dakota and is hereby approved.

Chris Nelson
Dean of the School of Graduate Studies

Date

PERMISSION

Title: The Impacts of Airborne Cloud Microphysical Instrumentation Mounting Location on Measurements Made During the Observations of Aerosols above Clouds and their Interactions (ORACLES) Project

Department: Atmospheric Sciences

Degree: Doctor of Philosophy

In presenting this dissertation in partial fulfillment of the requirements for a graduate degree from the University of North Dakota, I agree that the library of this University shall make it freely available for inspection. I further agree that permission for extensive copying for scholarly purposes may be granted by the professor who supervised my dissertation work or, in his absence, by the Chairperson of the department or the dean of the School of Graduate Studies. It is understood that any copying or publication or other use of this dissertation or part thereof for financial gain shall not be allowed without my written permission. It is also understood that due recognition shall be given to me and to the University of North Dakota in any scholarly use which may be made of any material in my dissertation.

Joseph R. O'Brien

27 July 2023

TABLE OF CONTENTS

LIST OF FIGURES	vi
LIST OF TABLES	vii
ACKNOWLEDGEMENTS	viii
ABSTRACT	x
CHAPTER	
INTRODUCTION	1
ORACLES FIELD PROJECT	3
NASA P-3 ORION	8
BACKGROUND	14
AIRFLOW INVESTIGATIONS	14
COMPUTATIONAL FLUID DYNAMICS	17
INCOMPRESSIBLE FLUID FLOW COMPUTATION	23
COMPRESSIBLE FLUID FLOW COMPUTATION	25
MOTIVATION	27
OBJECTIVE	28
METHODOLOGY	30
COMPUTATIONAL FLUID DYNAMICS - OPENFOAM	30
OPENFOAM – NASA P-3 CASES	31
OPENFOAM – PRE-PROCESSING	32
OPENFOAM - SOLVER	36
OPENFOAM - POSTPROCESSING	40
RESULTS	45
MESH QUALITY	47
SOLUTION RESIDUALS	49

NAVY PYLON SIMULATIONS	51
EXTENDED PYLON SIMULATIONS	68
CLOUD DROPLET PROBE – SAMPLE VOLUME	77
LAGRANGIAN PARTICLES	86
DISCUSSION	89
THE MYTH OF IN-SITU FREESTREAM OBSERVATIONS	89
LIMITATIONS IN INSTRUMENT PLACEMENT	91
LIMITATIONS WITHIN THE NASA P-3 MODEL	91
RELATEABILITY OF SIMULATIONS TO OBSERVATIONS	94
SUMMARY AND CONCLUSIONS	98
CONSIDERATIONS FOR FUTURE AIRCRAFT	101
REFERENCES	105
APPENDIX A – <i>snappyHexMesh</i> CONFIGURATION FILES	112
APPENDIX B – <i>thermoPhysicalProperties</i> CONFIGURATION FILES	120
APPENDIX C – BOUNDARY CONDITIONS CONFIGURATION FILES	122
APPENDIX D – SYSTEM DIRECTORY CONFIGURATION FILES	128

LIST OF FIGURES

Figure	Page
1. NASA P-3 Orion intensive operations period flight paths for September 2016 (red), August 2017 (not shown yet), and October 2018 (green).....	4
2. ORACLES Science Team in front of the NASA P-3 Orion in Sao Tome and Principe in August 2018.....	5
3. Domain discretization for the simplified example of horizontal wind flow across a building (shown in green), with structured (B) and unstructured mesh (C) and associated centroids.....	19
4. Cloud Droplet Probe (CDP) mounting locations with respect to the leading with Respect to the leading edge of the wings on-board the NASA P-3 Orion during ORACLES 2018 field experiment in Sao Tome. Figure 1a (Figure 1b) contains the Navy (Extended) pylon design with the Langley Airborne Research Center (Uni. of Hawaii) CDP.....	28
5. Three-dimensional computer-aided design (CAD) models of the NASA P-3 Navy pylon configuration (Figure 2-A) and Extended pylon configuration (Figure 2-B). Each configuration contains designs for the Cloud Droplet Probe and “bullet” canister used during ORACLES 2018.....	33
6. Example of the mesh generation from the snappyHexMesh meshing utility, detailing the structure outline (a), splitting of the domain around this structure (b), removal of interior cells (c), and incorporation into the domain (d). Figure is a modification of Figure 5.8, Figure 5.10, Figure 5.11, and Figure.13 within Greenshields 2016).....	34

7. Mach Number for the NASA P-3 Orion during in-situ cloud sampling throughout ORACLES. Shading for each violin plot represents data distribution of Mach Number. Red (black) lines represent the mean (median) of the distribution.....	35
8. Static pressure (hectopascal) for the NASA P-3 Orion during in-situ cloud sampling throughout ORACLES. Shading for each violin plot represents data distribution of static pressure. Red (black) lines represent the mean (median) of the distribution.....	36
9. Static air temperature (Celsius) for the NASA P-3 Orion during in-situ cloud sampling throughout ORACLES. Shading for each violin plot represents data distribution of static air temperature. Red (black) lines represent the mean (median) of the distribution.....	37
10. True Air Speed for the NASA P-3 Orion during in-situ cloud sampling throughout ORACLES. Shading for each violin plot represents data distribution. Red (black) lines indicate mean (median) of the distribution.....	39
11. Directory structure for the OpenFOAM solver, rhoSimpleFoam, for the NASA_P3_extendedPylon_v2_tas120_aoa0_900T33 case. Listed are all required files for processing. Names listed within brackets indicate a directory...	41
12. Residual plot of the dependent variables within the rhoSimpleFoam solver for the Navy Pylon solution (True Air Speed – 120 m/s; Angle of Attack = 0°; Pressure = 900 mb, Temperature = 33C boundary conditions).....	50
13. NASA P-3 Orion Navy Pylon configuration showcasing velocity magnitudes with a two-dimensional slice through the solution with a view point along the wing (into the page is towards the fuselage). For this simulation, boundary conditions are: freestream airspeed 120 meters per second, angle of attack zero	

degrees, freestream pressure 900 millibars and temperature 33 degrees Celsius. Contours represent every 3.33 meters per second difference in velocity.....	52
14. NASA P-3 Orion Navy Pylon configuration showcasing velocity magnitudes with a two-dimensional slice through the solution with a view point along the wing (into the page is towards the fuselage). For this simulation, boundary conditions are: freestream airspeed 120 meters per second, angle of attack zero degrees, freestream pressure 900 millibars and temperature 33 degrees Celsius. Contours represent every 3.33 meters per second difference in velocity.....	53
15. NASA P-3 Orion Navy Pylon configuration showcasing velocity magnitudes with a two-dimensional slice through the center line of the fuselage For this simulation, boundary conditions are: freestream airspeed 120 meters per second, angle of attack zero degrees, freestream pressure 900 millibars and temperature 33 degrees Celsius. Contours represent every 3.33 meters per second difference in velocity.....	54
16. NASA P-3 Orion Navy Pylon configuration showcasing atmospheric pressure with a two-dimensional slice through the center line of the Cloud Droplet Probe. For this simulation, boundary conditions are: freestream airspeed 120 meters per second, angle of attack zero degrees, freestream pressure 900 millibars and temperature 33 degrees Celsius. Contours represent every 133.3 Pa difference in pressures.....	55
17. NASA P-3 Orion Navy Pylon configuration showcasing atmospheric pressure with a two-dimensional slice across the leading edge of the aircraft wing. For this simulation, boundary conditions are: freestream airspeed 120 meters per second, angle of attack zero degrees, freestream pressure 900 millibars and temperature 33 degrees Celsius. Contours represent every 133.3 Pa difference in pressures.....	56

18. NASA P-3 Orion Navy Pylon configuration showcasing atmospheric pressure with a two-dimensional slice through the centerline of the fuselage. For this simulation, boundary conditions are: freestream airspeed 120 meters per second, angle of attack zero degrees, freestream pressure 900 millibars and temperature 33 degrees Celsius. Contours represent every 133.3 Pa difference in pressures.....	57
19. NASA P-3 Orion Navy Pylon configuration showcasing total temperature with a two-dimensional slice through the center of the Cloud Droplet Probe. For this simulation, boundary conditions are: freestream airspeed 120 meters per second, angle of attack zero degrees, freestream pressure 900 millibars and temperature 33 degrees Celsius. Contours represent every 1.5 Kelvin difference in temperature.....	58
20. NASA P-3 Orion Navy Pylon configuration showcasing total temperature with a two-dimensional slice along the leading edge of the aircraft wing. For this simulation, boundary conditions are: freestream airspeed 120 meters per second, angle of attack zero degrees, freestream pressure 900 millibars and temperature 33 degrees Celsius. Contours represent every 1.5 Kelvin difference in temperature.....	59
21. NASA P-3 Orion Navy Pylon configuration showcasing total temperature with a two-dimensional slice along centerline of the aircraft fuselage. For this simulation, boundary conditions are: freestream airspeed 120 meters per second, angle of attack zero degrees, freestream pressure 900 millibars and temperature 33 degrees Celsius. Contours represent every 1.5 Kelvin difference in temperature.....	60
22. NASA P-3 Orion Navy Pylon configuration showcasing velocity magnitudes with a two-dimensional slice through the solution with a view point along the wing (into the page is towards the fuselage). For this simulation, boundary	

conditions are: freestream airspeed 120 meters per second, angle of attack positive four degrees , freestream pressure 900 millibars and temperature 33 degrees Celsius. Contours represent every 3.33 meters per second difference in velocity.....	61
23. NASA P-3 Orion Navy Pylon configuration showcasing atmospheric pressure with a two-dimensional slice through the center line of the Cloud Droplet Probe. For this simulation, boundary conditions are: freestream airspeed 120 meters per second, angle of attack positive four degrees, freestream pressure 900 millibars and temperature 33 degrees Celsius. Contours represent every 133.3 Pa difference in pressures.....	62
24. NASA P-3 Orion Navy Pylon configuration showcasing velocity magnitudes with a two-dimensional slice through the solution with a view point along the wing (into the page is towards the fuselage). For this simulation, boundary conditions are: freestream airspeed 120 meters per second, angle of attack negative four degrees, freestream pressure 900 millibars and temperature 33 degrees Celsius. Contours represent every 3.33 meters per second difference in velocity.....	63
25. NASA P-3 Orion Navy Pylon configuration showcasing velocity magnitudes with a two-dimensional slice through the solution with a view point along the wing (into the page is towards the fuselage). For this simulation, boundary conditions are: freestream airspeed 120 meters per second, angle of attack negative four degrees, freestream pressure 900 millibars and temperature 33 degrees Celsius. Contours represent every 3.33 meters per second difference in velocity.....	64
26. NASA P-3 Orion Extended Pylon configuration showcasing velocity magnitudes with a two-dimensional slice through the solution with a view point along the wing (into the page is towards the fuselage). For this	

simulation, boundary conditions are: freestream airspeed 120 meters per second, angle of attack zero degrees, freestream pressure 900 millibars and temperature 33 degrees Celsius. Contours represent every 3.33 meters per second difference in velocity.....	65
27. NASA P-3 Orion Extended Pylon configuration showcasing total temperature with a two-dimensional slice along the leading edge of the aircraft wing. For this simulation, boundary conditions are: freestream airspeed 120 meters per second, angle of attack zero degrees, freestream pressure 900 millibars and temperature 33 degrees Celsius. Contours represent every 3.33 meters per second difference in velocity.....	66
28. NASA P-3 Orion Extended Pylon configuration showcasing atmospheric pressure with a two-dimensional slice through the center line of the Cloud Droplet Probe. For this simulation, boundary conditions are: freestream airspeed 120 meters per second, angle of attack zero degrees, freestream pressure 900 millibars and temperature 33 degrees Celsius. Contours represent every 133.3 Pa difference in pressures.....	68
29. NASA P-3 Orion Extended Pylon configuration showcasing total temperature with a two-dimensional slice along centerline of the aircraft fuselage. For this simulation, boundary conditions are: freestream airspeed 120 meters per second, angle of attack zero degrees, freestream pressure 900 millibars and temperature 33 degrees Celsius. Contours represent every 1.5 Kelvin difference in temperature.....	69
30. NASA P-3 Orion Extended Pylon configuration showcasing velocity magnitudes with a two-dimensional slice through the solution with a view point along the wing (into the page is towards the fuselage). For this simulation, boundary conditions are: freestream airspeed 120 meters per second, angle of attack positive four degrees, freestream pressure 900 millibars	

and temperature 33 degrees Celsius. Contours represent every 3.33 meters per second difference in velocity.....	70
31. NASA P-3 Orion Extended Pylon configuration showcasing atmospheric pressure with a two-dimensional slice through the center line of the Cloud Droplet Probe. For this simulation, boundary conditions are: freestream airspeed 120 meters per second, angle of attack positive four degrees, freestream pressure 900 millibars and temperature 33 degrees Celsius. Contours represent every 133.3 Pa difference in pressures.....	71
32. NASA P-3 Orion Extended Pylon configuration showcasing velocity magnitudes with a two-dimensional slice through the solution with a view point along the wing (into the page is towards the fuselage). For this simulation, boundary conditions are: freestream airspeed 120 meters per second, angle of attack negative four degrees, freestream pressure 900 millibars and temperature 33 degrees Celsius. Contours represent every 3.33 meters per second difference in velocity.....	72
33. NASA P-3 Orion Extended Pylon configuration showcasing atmospheric pressure with a two-dimensional slice through the center line of the Cloud Droplet Probe. For this simulation, boundary conditions are: freestream airspeed 120 meters per second, angle of attack negative four degrees, freestream pressure 900 millibars and temperature 33 degrees Celsius. Contours represent every 133.3 Pa difference in pressures.....	73
34. NASA P-3 Orion Extended Pylon configuration showcasing airflow velocity with a two-dimensional slice along centerline of the aircraft fuselage. For this simulation, boundary conditions are: freestream airspeed 120 meters per second, angle of attack zero degrees, freestream pressure 900 millibars and temperature 33 degrees Celsius. Contours represent every 3.33 meters per second.	74

35. NASA P-3 Orion Extended Pylon configuration showcasing pressure field with a two-dimensional slice along centerline of the aircraft fuselage. For this simulation, boundary conditions are: freestream airspeed 120 meters per second, angle of attack zero degrees, freestream pressure 900 millibars and temperature 33 degrees Celsius. Contours represent every 133.3 Pa.	75
36. Subset of the velocity field through the mesh leading up to the Cloud Droplet Probe sample volume for the Navy Pylon solutions with the boundary conditions of 120 meters per second freestream and all simulated angle of attacks.....	77
37. Subset of the velocity field through the mesh leading up to the Cloud Droplet Probe sample volume for the Navy Pylon solutions with the boundary conditions of 140 meters per second freestream and all simulated angle of attacks.....	78
38. Subset of the velocity field through the mesh leading up to the Cloud Droplet Probe sample volume for the Extended Pylon solutions with the boundary conditions of 120 meters per second freestream and all simulated angle of attacks.....	79
39. Subset of the velocity field through the mesh leading up to the Cloud Droplet Probe sample volume for the Extended Pylon solutions with the boundary conditions of 140 meters per second freestream and all simulated angle of attacks.....	80
40. Subset of the velocity field through Cloud Droplet Probe sample volume (marked by vertical blue line) for the Navy Pylon solutions with the boundary conditions of 120 meters per second freestream and all simulated angle of attacks.....	81

41. Subset of the velocity field through Cloud Droplet Probe sample volume (marked by vertical blue line) for the Extended Pylon solutions with the boundary conditions of 120 meters per second freestream and all simulated angle of attacks.....	82
42. Subset of the velocity field through Cloud Droplet Probe sample volume (marked by vertical blue line) for the Extended Pylon solutions with the boundary conditions of 140 meters per second freestream and all simulated angle of attacks.....	83
43. Simulated Lagrangian particles (10 micron in diameter, 100 #/cc concentration) for the compressible flow simulation of airflow around a Particle Measurement System canister used during ORACLES. Particles are shaded with calculated horizontal velocities, with a departure from freestream centered in front of the canister.....	86
44. Kernel Density Estimation for simulated particles (10 microns, 100 #/cc) within the compressible flow simulation around the Navy Pylon configuration. Left side of figure contains kernel density for the simulation inlet, while right side of figure contains estimate for particles directly in front of the Cloud Droplet Probe canister. Contoured are 99% of all particles.....	87
45. Kernel Density Estimation for simulated particles (10 microns, 100 #/cc) within the compressible flow simulation around the Extended Pylon configuration. Left side of figure contains kernel density for the simulation inlet, while right side of figure contains estimate for particles directly in front of the Cloud Droplet Probe canister. Contoured are 99% of all particles.....	88
46. Distribution of observed true air speed (meters per second) from the Cloud, Aerosol, Precipitation Spectrometer during ORACLES for specific cloud	

<p>sampling profiles. For ORACLES 2016, the Cloud, Aerosol, Precipitation Spectrometer was mounted on the Navy pylon configuration, while it was mounted on the Extended Pylon for ORACLES 2017 and ORACLES 2018...</p>	94
<p>47. Comparison of true air speed observations between the Cloud, Aerosol, and Precipitation Spectrometer and NASA P-3 fuselage. For ORACLES 2016, the Cloud, Aerosol, Precipitation Spectrometer was mounted to the Navy Pylon on the port side outboard pylon. For ORACLES 2017, at the same location, the Cloud, Aerosol, Precipitation Spectrometer was mounted to the Extended Pylon.....</p>	95
<p>48. Comparison of Cloud and Aerosol Spectrometer with two Cloud Droplet Probes during the sawtooth cloud profiles from ORACLES 2018. Within this figure, New Pylon refers to the Extended Pylon configuration, while Old Pylon refers to Navy Pylon configuration.....</p>	96

LIST OF TABLES

Table	Page
<p>1. In-situ Cloud Microphysical instrumentation operated by the University of North Dakota and the University of Oklahoma during the ORACLES field campaigns. For ORACLES 2017 and ORACLES 2018, a second Cloud Droplet Probe was included within this suite. The CAS and CIP instruments are a part of the Cloud and Aerosol Spectrometer (CAPS). The CAS, 2DS, and HVPS-3 fundamental measurement is two-dimensional particle images from which the size distribution is derived.....</p>	9
<p>2. Selected OpenFOAM boundary conditions default values for compressible flow simulations. For each default velocity, flow angle is adjusted to simulate three separate angle of attacks.....</p>	42
<p>3. Results of the OpenFOAM checkMesh utility topology tests for the Navy and Extend Pylon configurations. Shown are the number of points and faces used to represent the domain and geometry for each simulation. The total number of cells, points and faces are consistent between pylon configurations and thus, summarized for each configuration below.....</p>	48
<p>4. Results of the OpenFOAM checkMesh utility geometry tests for the Navy and Extend Pylon configurations.....</p>	49
<p>5. Final residuals of the dependent variables within the rhoSimpleFoam solver for the final iteration for each NASA P-3 solution.....</p>	51

6. Extracted velocity values for the nearest centroid to the Cloud Droplet Probe sample volume within the Extended Pylon Simulations and calculated percent of freestream for the magnitude of velocity.....	84
7. Extracted velocity values for the nearest centroid to the Cloud Droplet Probe sample volume within the Navy Pylon Simulations and calculated percent of freestream for the magnitude of velocity. Additionally, extracted velocity values for simulation of the NASA P-3 without pylons for the Cloud Droplet Probe sample volume locations within the Navy and Extended Pylon simulations.....	85

ACKNOWLEDGEMENTS

I wish to express my sincere appreciation to Dr. Katelyn Barber for the first proofreading of this manuscript, offering endless encouragement and support, assistance with the display and calculation of Lagrangian particle tracking (finally!), and patience during this process.

I wish to express my sincere appreciation to the members of my advisory Committee for their guidance and support during my time in the Doctor of Philosophy program at the University of North Dakota.

I wish to express my sincere appreciation to Professor Mike Poellot and Dr. David Delene for the opportunity to conduct research across the globe and for starting a lifelong fascination with airborne meteorology.

I wish to express my sincere appreciation for Dr. Scott Collis, Adam Theisen, Dr. Robert Jackson, Zachary Sherman and Maxwell Grover for the endless enthusiasm for open-source science and the weekly ‘check this out’ chats at Argonne National Laboratory. These chats saved this analysis and made this work possible.

Finally, I wish to express my sincere appreciation to everyone involved with the ORACLES field campaign that are overlooked in publications, citations, or conference presentations, but were there in the trenches during the annual 15 weeks at Wallops integrating instrumentation or slamming away at data quality assurance with me. This work would not be possible without all our hard work. Thank you.

To my family,
Thank you for the support and encouragement these many years.
Thank you for encouragement to follow my curiosity.
As you will see, it eventually brought me around the world and back.

To the many teachers, mentors, friends, and colleagues,
Thank you for the support and encouragement to finish this.

ABSTRACT

ORACLES (ObseRvations of Aerosols above CLouds and their intEractionS) was a five-year NASA investigation into the climate impacts of Southern Africa's biomass burning aerosols. The University of North Dakota, in coordination with the Cooperative Institute for Severe and High-Impact Weather Research and Operations, the University of Oklahoma and University of Illinois at Urbana-Champaign integrated and operated a suite of in-situ cloud microphysical instrumentation into the NASA P-3 Orion aircraft to study aerosol-cloud interactions within this region. However, during the course of the individual ORACLES campaigns, the accuracy of the cloud microphysical observations were uncertain due to the mounting location of instruments with respect to the aircraft wing. To address these concerns, an additional wing-mounted pylon design was created and was installed moving the instruments ahead of the leading edge of the aircraft wing in order to sample freestream conditions for ORACLES-2017 and ORACLES-2018. To study the impact of mounting location on cloud microphysical observations taken during ORACLES, a computational fluid

dynamical analysis of the NASA P-3 Orion with both pylon designs is performed. Utilizing the OpenFOAM software package, a Eulerian-Lagrangian framework is utilized to simulate compressible flow with particle tracking around the aircraft, mounting locations, and instrumentation. Simulations of the predominant ORACLES vertical cloud sampling profiles, known as sawtooths, and multiple environmental factors are considered. Within the simulated Cloud Droplet Probe sample volume, the departure of the velocity field from freestream conditions was found to vary by up to twelve percent during sawtooth maneuvers for the NASA P-3 original pylon design. While the new pylon design did not achieve freestream conditions, it did minimize this distortion in flow caused by the sawtooth maneuvers, with a five percent difference in the departure of the velocity field from freestream between ascent and descent sawtooth profiles. Overall, the original NASA P-3 pylon design observed the closest velocities to freestream conditions across all simulations.

CHAPTER I

INTRODUCTION

One of the largest remaining uncertainties within anthropogenic climate forcing are the impacts of atmospheric aerosols. Within the atmosphere, aerosols can affect the radiation balance of the Earth-atmosphere system through the scattering and absorption of solar radiation (Liou 2002). The radiative properties of aerosols are dependent on their radiative indices as functions of the incident wavelength and on the size, shape and chemical composition of the aerosol. Direct radiative forcing of aerosols, or estimates of the change in energy flux within the atmosphere due to natural or anthropogenic factors of climate change, is dependent on the ratio of absorption to total extinction and also relies on the albedo of the underlying surface-atmosphere layer (Coakley and Chylek 1975; Redemann et al. 2021). The Fifth Assessment Report by the Intergovernmental Panel on Climate Change (IPCC) assessed the direct radiative forcing of aerosols as -0.35 W m^{-2} $[-0.85 \text{ to } +0.15 \text{ W m}^{-2}]$, with a negative radiative forcing indicting a cooling effect in the atmosphere due to the backscattering of incident solar radiation (Boucher et al. 2013; Bellouin et al. 2020).

Among the uncertainties within the radiative forcing of aerosols are interactions between clouds and aerosols produced through biomass burning, which refers to the burning of living and dead vegetation through human-induced burns, as well as natural lightning induced fires. The capacity of biomass burning aerosols to absorb and scatter incident solar radiation is dependent on the nature of the burned biomass and burning conditions (Brioude et al. 2009). One of the emissions of biomass burning are black carbon soot aerosols, the strongest absorbing aerosol within the atmosphere (Redemann et al. 2021). Previous investigations have found that the sign of the direct aerosol forcing is dependent on location of the biomass burning

aerosols with respect to underlying clouds as the black carbon aerosol decrease the albedo of the underlying cloud (Chand et al. 2009).

Two additional aerosol cloud interactions that contribute to the uncertainties within the radiative forcing of aerosols are the indirect and semi-direct aerosol effect. The aerosol indirect effect refers to the processes which involve aerosols acting as cloud condensation nuclei, with the two most prominent theories being the Twomey and Albrecht effects (Lohmann and Feichter 2005). Twomey (1977) investigated the role of aerosols (through natural and anthropogenic causes) on droplet activation within fixed cloud water amounts, and found that with increasing cloud condensation nuclei, smaller, more numerous cloud droplets were formed. The increase in cloud droplets resulted in increased cloud albedo, enhancing the reflectance of solar radiation and producing a slight negative radiative forcing at the top of the atmosphere. Albrecht (1989) investigated the Twomey effect in varying cloud water amounts with marine stratocumulus, proposing a link between cloud lifetime and aerosols through precipitation. Albrecht (1989) argued that while the Twomey effect creates more numerous, smaller droplets (with increasing aerosol concentrations), the result of a decrease in distribution variability is the reduction in collision-coalescence and precipitation efficiency. Albrecht (1989) suggested that the decrease in precipitation efficiency would increase cloud liquid water and fractional cloudiness, resulting in brighter, longer lasting marine stratocumulus.

The semi-direct aerosol effect refers to the interactions between absorbing aerosols and clouds within the same vertical column of atmosphere, where the heating of mid-troposphere by aerosol solar absorption influences cloud dynamics (Hansen et al. 1997). Hansen et al. (1997) theorized that the presence of black carbon aerosols within the marine boundary layer would lead to increased heating, a reduction in relative humidity and large scale cloud cover.

Reduction in cloud cover would result in the decrease of planetary albedo and a positive radiative forcing. Conversely, using large-eddy simulations of the marine stratocumulus off the Californian coast, Johnson et al. (2004) showed that the sign of the radiative forcing of the semi-direct effect depends on the vertical location of the aerosol plume with respect to the marine stratocumulus. Johnson et al. (2004) was also able to show that marine stratocumulus geometric thickness was influenced by the vertical distribution of the aerosol and cloud layers, with an increase in liquid water path when these are vertically separated due to the relaxation of the entrainment of dry mid-tropospheric air into the marine boundary layer. With the uncertainty of the sign and magnitude of the radiative forcing of biomass burning aerosols, investigations into the interactions between biomass burning aerosols and underlying cloud populations are needed.

ORACLES FIELD PROJECT

ORACLES (ObseRvations of Aerosols above CLouds and their intEractionS) was a five-year NASA investigation into the climate impacts of Southern Africa's biomass burning aerosols (Redemann et al. 2021). The southern African continent accounts for almost one third of the Earth's total biomass burning emissions, with burned areas in southern Africa increasing even with the decreasing trend in global biomass burning (Andela et al. 2017; Redemann et al. 2021). Biomass burning aerosol emissions from southern Africa are routinely transported west off the continent and over one of the world's three semi-permanent marine stratocumulus cloud decks. These regions, in which the annual mean marine stratocumulus cloud cover is between 40-60%, reside in the subtropical eastern oceans, roughly 5-10° longitude to the west of North America, South America, and Africa (Wood 2012). The abundance of biomass burning aerosols, marine stratocumulus cloud

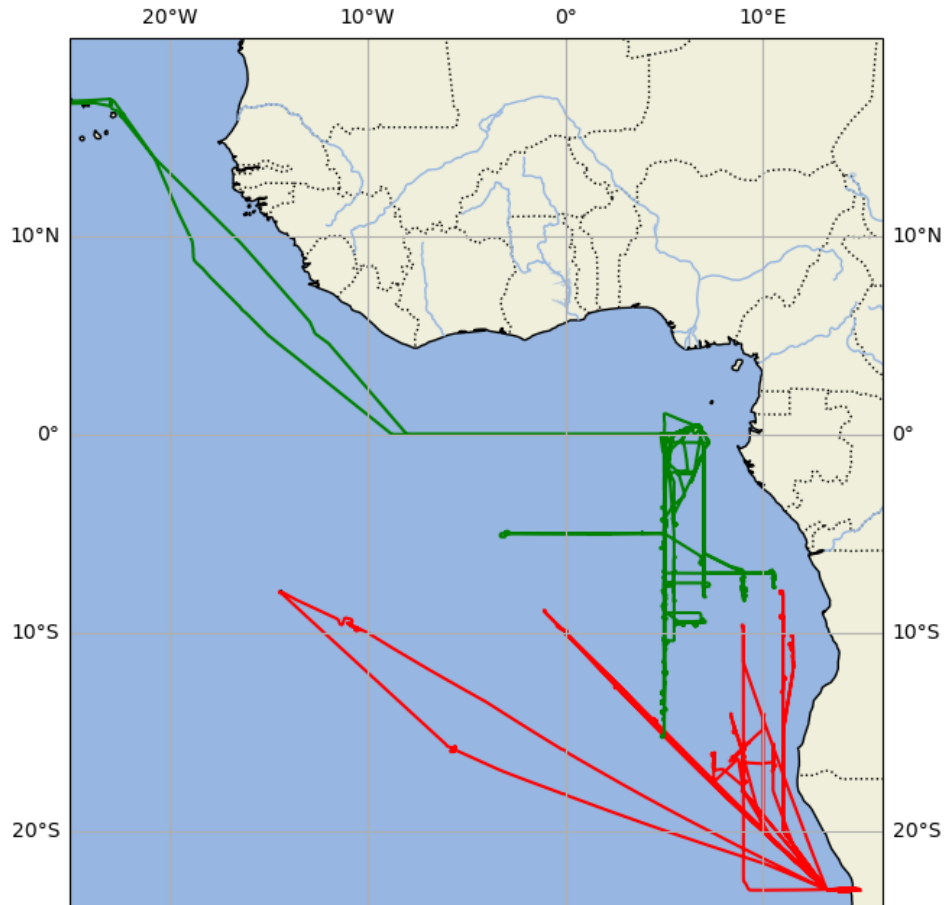


Figure 1: NASA P-3 Orion Intensive Operations Period flight paths for September 2016 (red) and October 2018 (green).

coverage, and limited previous in-situ observational experiments made the southeast Atlantic region advantageous to investigate aerosol-cloud interactions.

Investigation into these aerosol-cloud interactions were separated into three specific science objectives centered around the direct, indirect and semi-direct aerosol effects. The first scientific objective of ORACLES was to determine the direct radiative effect of the African biomass burning aerosol layer in clear and cloudy sky conditions over the southeast Atlantic (Redemann et al. 2021). Central to this objective was determination of the evolution of the biomass burning aerosol radiative properties as it is transported away from the continent and assessment of the key factors that control seasonal variations in aerosol direct effects (Redemann et al. 2021). ORACLES second scientific objective was to determine how the



Figure 2: ORACLES Science Team in front of the NASA P-3 Orion in Sao Tome and Principe in August 2018. Photo is courtesy of NASA Earth Science Project Office (ESPO).

absorption of solar radiation by the African biomass burning aerosol layer affects atmospheric stability and cloud properties by exploring the seasonally varying vertical distribution of aerosol and cloud properties as a function of distance from shore (Redemann et al. 2021). The third scientific objective focused on how biomass burning aerosols affected marine stratocumulus microphysical properties, precipitation and lifetime through exploration of aerosol mixing mechanisms into the marine boundary layer (Redemann et al. 2021). As shown in the flight tracks within Figure 1, three separate field experiments were conducted off the coast of Africa, utilizing the NASA P-3 aircraft (shown in Figure 2) in September 2016, August 2017, and October 2018 to achieve these scientific goals.

For ORACLES-2016, the NASA P-3 and NASA ER-2 aircraft were stationed in Walvis Bay, Namibia ($22^{\circ}57'S$ $14^{\circ}30'E$). Intensive operations periods were separated into two

categories: routine flights and flights of opportunity. For routine flights, a flight path along a the diagonal with endpoints of 20°S/10°E and 10°S/0°E from Walvis Bay was selected to transect the biomass burning aerosol plume and allow for observations near an area with variable marine stratocumulus cloud fraction (Redemann et al. 2021). Routine flights contain a constant flight profile to provide consistency to the observations and allow for monthly to seasonal trends in aerosol cloud interactions to be studied. The routine flight profile would consist of level flight legs within the aerosol plume at constant altitude, a spiral descent into the marine boundary layer at the furthest extent of the flight path, cloud and aerosol in-situ sampling at various altitudes ramping back up to maximum altitude and return at altitude to Walvis Bay. Cloud and aerosol in-situ sampling were separated into two distinct maneuvers: ‘sawtooth’ profiles and level legs. For ‘sawtooth’ profiles, the NASA P-3 would descend from above the aerosol plume and through the marine stratocumulus cloud layer. From below cloud base, the NASA P-3 would ascend back through the top of the aerosol layer and restart the profile. Depending on the environmental conditions, these ‘sawtooth’ profiles would routinely result in four to six full vertical profiles observations of the vertical distributions of the cloud and aerosol layers. Typically following ‘sawtooth’ profiles, the NASA P-3 would conduct constant altitude flight legs a hundred meters below cloud, within cloud, and within the aerosol plume above cloud. Flights of opportunity were deviations from these routine flights to target unique features or events, such as profiles closer to the African continent to observe more recently emitted biomass burning aerosol plumes. In total, the NASA P-3 Orion aircraft flew 350.6 flight hours in 44 science operations flights between ORACLES-2016 and ORACLES-2018, resulting in 329 cloud profiles transecting the vertical distribution of marine stratocumulus (Redemann et al. 2021; Gupta et al. 2022).

For ORACLES-2017 and ORACLES-2018, the NASA P-3 was stationed in Sao Tome and Principe (0°20'N 6°44'E), a small African island nation located west of Gabon and south of Nigeria along the equator. As the NASA ER-2 only deployed during ORACLES-2016, modifications to the NASA P-3 instrument configuration were made to accommodate the addition of the NASA Langley High Spectral Resolution Lidar 2 (HSRL-2) (Müller et al. 2014), the addition of a counterflow virtual impactor to the aircraft fuselage, and changes to the configuration of the in-situ cloud microphysical instrumentation (Redemann et al. 2021). These modifications, along with the geographic change in location, resulted in a methodology change to flight plans. Routine flights were flown along the 6°E meridian from Sao Tome, with the goal of sampling the maximum of the biomass burning aerosol plume. In contrast to ORACLES-2016, high altitude transit legs were flown above the biomass burning aerosol plume to maximize the effectiveness of the HSRL-2. Additionally, changes to 'sawtooth' profiles were made to allow for twenty-kilometer level legs at the top and bottom of each profile to allow for observations of above cloud aerosol optical depth. During ORACLES-2017, flights of opportunity were focused on transits from Sao Tome to Ascension Island (7°56'S 14°25'W) for cooperation and intercomparison with the Cloud-Aerosol-Radiation Interaction and Forcing (CLARIFY-2017) campaign and the Department of Energy's Atmospheric Radiation Measurement Program's Layered Atmospheric Smoke Interactions with Clouds (LASIC) campaign (Barrett et al. 2022). Transit flights to Ascension Island also allowed for the evaluation on the evolution of the biomass burning aerosol plume as a distance from the continent. For ORACLES-2018, flights of opportunity were focused on remaining scientific objectives, such as LaGrangian tracking of the biomass burning aerosol plume.

NASA P-3 ORION

The University of North Dakota, in coordination with the Cooperative Institute for Severe and High-Impact Weather Research and Operations, the University of Oklahoma and University of Illinois at Urbana-Champaign (hereafter ‘Cloud Probes team’), integrated and operated a suite of in-situ cloud microphysical instrumentation into the NASA P-3 Orion aircraft for all ORACLES deployments. Shown in Figure 2, the NASA P-3 Orion is a four-engine turboprop aircraft that has been transitioned from the U.S Navy to the NASA Airborne Science Program. Operated out of the NASA Goddard Space Flight Center’s Wallops Flight Facility Aircraft Office, the NASA P-3 Orion has been extensively modified to support various NASA Airborne Science Program science objectives, including the addition of zenith and nadir ports, ten wing mounted locations, a fuselage port for a dropsonde launcher, and an isokinetic inlet for cabin instruments, among others. The NASA P-3 Orion was a desirable platform for ORACLES due to its ability to conduct long duration flights (8-14 hours), carry large science payloads, conduct low altitude flights over the ocean surface, reach flight altitudes up to 28,000 feet, and cover large spatial distances with flight true airspeeds up to 400 knots. For ORACLES, the Cloud Probes team maintained and operated seven instruments mounted to the NASA P-3 Orion wing mounting locations. The research objectives of the Cloud Probes team were to investigate the impact of aerosols on cloud properties and precipitation, primarily the aerosol indirect effect in precipitation suppression and cloud lifetime (Albrecht 1989; Twohy et al. 2005; Lohmann and Feichter 2005, Fan et al. 2016; Gupta et al. 2021, 2022).

The suite of instrumentation operated by the Cloud Probes team, shown in Table 1, allowed for observation of the number of particles in a given volume, or the particle number concentration, for the biomass burning aerosol plume and marine stratocumulus. Critical to

Table 1: In-situ Cloud Microphysical instrumentation operated by the University of North Dakota and the University of Oklahoma during the ORACLES field campaigns. For ORACLES 2017 and ORACLES 2018, a second Cloud Droplet Probe was included within this suite. The CAS and CIP instruments are a part of the Cloud and Aerosol Spectrometer (CAPS). The CAS, 2DS, and HVPS-3 fundamental measurement is two-dimensional particle images from which the size distribution is derived.

Instrument	Main Parameter	Sampling Frequency	Measurement Range
Cloud Droplet Probe (CDP)	Cloud Droplet Number Distribution $n(D)$	10 Hz	2 – 50 μm
Cloud and Aerosol Spectrometer (CAS)	Cloud Droplet Number Distribution $n(D)$	10 Hz $n(D)$;	0.5 – 50 μm
Cloud Imaging Probe (CIP)	Droplet Number Distribution $n(D)$	Asynchronous Images 1 Hz $n(D)$	25-1600 μm
Two-Dimensional Stereo Probe (2DS)	Droplet Number Distribution $n(D)$	Asynchronous images; 1 Hz $n(D)$	10 – 1280 μm
High Volume Precipitation Spectrometer (HVPS-3)	Droplet Number Distribution $n(D)$	Asynchronous images; 1 Hz $n(D)$	150 – 19200 μm
Passive Cavity Aerosol Spectrometer (PCASP-SPP200)	Aerosol Number Distribution $n(D)$	10 Hz	0.1 – 3 μm
CSIRO King Hotwire	Bulk Liquid Water Content	25 Hz	0.05 – 3 g m^{-3}

these observations are two classes of instruments: optical array probes and forward scattering probes. Optical array probes produce shadow images of particles passing through a high-intensity laser beam that illuminates a linear array of photodetectors. Since the object plane where particles are detected varies with the square of the particle diameter (i.e. depth of field), optical array probes allow for an increase in sample volume to compensate for the decrease in

concentration of larger particles (Knollenberg 1970). While this allows the ability to measure a large range of particles, optical array probes are known to produce large counting and sizing errors due to particles that pass outside of the optical depth of field. To determine particle size distributions, the number and size of each shadow image is calculated within a given time interval during post-processing. The particle size of each shadow image is typically determined by fitting a minimum bounding circle to each image, with the diameter of the circle determined to be the particle diameter, but various sizing methods exist (Wu and McFarquhar 2016).

As the name implies, forward scattering probes collect light scattered in a forward direction by a hydrometeor passing through the sample area. Through Mie scattering theory, the measured light intensity scattered by the hydrometeor within the depth of field is then used to determine particle size and is categorized into corresponding size bins defined by a refractive index of a standard (Gardiner and Hallett 1985). By knowing the aircraft speed, the volume sampled by forward scattering probes can be determined and particle size distributions derived from observed histogram of particle counts. Forward scattering probes have been known to suffer from measurement artifacts known as “coincidence”, where more than one hydrometeor is registered by the instrument at the same time resulting in undercounting and oversizing bias (Lance 2012).

For ORACLES, the Cloud Probes team operated a suite of optical array probes: the Stratton Park Engineering Company (SPEC) Two-Dimensional Stereo Probe (2DS), the SPEC High Volume Precipitation Spectrometer Version 3 (HVPS-3), and Droplet Measurement Technologies (DMT) Cloud Imaging Probe (CIP). The 2DS consists of two orthogonal lasers that illuminate two linear 128 photodiode arrays, producing an effective pixel size of roughly ten microns and an overlap region where particle images are orthogonal (Lawson et al. 2006;

Lawson 2011). This overlap region was designed to improve upon existing depth of field issues with optical array probes, by allowing for the determination of the distance to either object plane and the creation of stereo images (Lawson et al. 2006). However, for ORACLES, the 2DS was treated as two separate optical array probes, one aligned vertically and one horizontally with respect to the horizon. Mainly used for precipitation sized hydrometeors, the HVPS-3 consists of a single orthogonal laser that illuminates a single linear 128 photodiode array, with an effective pixel size of 150 microns. The CIP was a component of a combination instrument called the Cloud, Aerosol and Precipitation Spectrometer (CAPS), and contained a single 62 photodiode array with an effective pixel size of 25 microns.

The forward scattering probes deployed for ORACLES were the DMT Cloud Droplet Probe Version 2 (CDP) and Cloud Aerosol Spectrometer (CAS). The CDP measured single particle scattering (between 4° - 12°) in the particle size range of 2 – 50 microns within thirty size bins. An advantage of the CDP over other forward scattering probes is the inclusion of an optical mask (800 micron diameter pinhole for ORACLES CDPs) installed in front of droplet sizing photodetector (Lance 2012). With this optical mask eliminating the collection of scattered light from outside the viewing angle, the CDP was able to reduce coincidence errors that plague traditional forward scattering probes. The CAS, a component of the CAPS instrument, measured single particle scattering in the forward (4° - 12°) and backward (168° - 176°) directions for hydrometeors between 0.6 – 50 microns within thirty size bins.

The two remaining instruments operated by the Cloud Probes team are: the DMT Passive Cavity Aerosol Spectrometer (PCASP) and Commonwealth Scientific and Industrial Research Organization (CSIRO) King Hotwire Probe. The PCASP is a light scattering spectrometer (35° - 120° collection angles), utilizing a helium neon classical passive cavity of wavelength 0.63

microns. The PCASP is capable of measuring aerosols in the size range of 0.1 – 3.0 microns within thirty size bins. Channel boundaries for these size bins are defined by the refractive index of particles likely to be measured by the instrument. The CSIRO King Hotwire Probe consists of a hollow cylinder 2 millimeters long (0.1 mm diameter) wire that is heated to a constant operating temperature, high enough to prevent water accumulation (King et al. 1978). Through analysis of the power drop when in contact with hydrometeors, the CSIRO King Hotwire Probe provides liquid water content to the accuracy of 0.1 g/m³.

Critical to each of these in-situ cloud microphysical instruments is the need for accurate atmospheric environmental (e.g. temperature and dewpoint) and aircraft (e.g. airspeed and pressure altitude) observations to determine the volume of air sampled by the aircraft. Central to these environmental observations are pitot-static and total temperature probes, which are widely used in general aviation to accurately describe the airspeed of the aircraft. Pitot-static tubes are often located on the nose (or the wing) of the aircraft and exposed to the airflow to measure ram pressure, or the air pressure created by motion. The static pressure, or the pressure in a moving, homogeneous incompressible fluid, is determined through static ports integrated into the pitot-static probe. Typically situated next to pitot-static probes are total temperature probes, which are designed to measure the stagnation temperature, or the temperature of air at the stagnation point, where the local airflow velocity is zero. Due to airflow compression around the stagnation point, an adiabatic increase in temperature occurs and the static temperature, or the environmental air temperature unaffected by the aircraft, can be determined. Using the static air temperature and the dynamic pressure, or the difference between the ram and static pressures, the speed of the aircraft can be determined.

Accurate airspeed measurements are critical for safe flight, as any malfunction can lead to erroneous measurements and the potential for the aircraft to enter an aerodynamical stall. Numerous disappearances and crashes of flights have been attributed to malfunctioning, blocked or ice over pitot-static probes, including Air France Flight 447 over the Atlantic in 2009 (Goldman 2018). The Boeing 737 MAX was infamously grounded worldwide in 2019 after the failure of a single angle of attack probe, in-combination with the failure of the Maneuvering Characteristics Augmentation System (MCAS) flight stabilizing feature, which contributed to the crashes of Lion Air Flight 610 in 2018 and Ethiopian Airlines Flight 302 in 2019 (2021). Critical to the accurate measurement of airspeed is the placement of the pitot-static and total temperature probes on the aircraft surface, which need to be properly located within the stagnation zone around the leading edge of the aircraft in order to measure ram pressure and total temperature.

Similar to these critical aviation probes, in-situ cloud microphysical instrumentation needs to be properly located on the aircraft in order to have accurate measurements of marine stratocumulus. However, during the course of the ORACLES campaigns, the accuracy of the cloud probe measurements was uncertain due to the mounting location of instruments with respect to the aircraft wing. This probe measurement uncertainty introduced additional challenges when conducting analyses of the aerosol-cloud interaction processes.

CHAPTER II BACKGROUND

AIRFLOW INVESTIGATIONS

Since the advent of reliable cloud microphysical instrumentation, considerable research has been done to investigate the airflow and particle trajectories around research aircraft in an effort to improve measurement accuracy. The uncertainty regarding these studies is whether instruments are placed such that they sample free-stream conditions. Beard (1983) investigated the orientation of precipitation particle images within a Particle Measurement Systems (PMS) Inc optical array probe (OAP), noting the titling of the particle images from direction of flight (i.e. canting angle) was dependent on particle size and habit. From the canting angle and deformation of the particle images, Beard (1983) calculated the acceleration of airflow ahead of the PMS canisters (assuming incompressible flow ahead of a simple sphere), showing flow distortion up to 50 cm ahead of the instrument. King (1984) and King et al. (1984) were able to calculate the potential flow (i.e. incompressible, inviscid, and non-turbulent flow) and particle trajectories around Commonwealth Scientific and Industrial Research Organization (CSIRO) F-27 research aircraft to study instrument placement on the aircraft fuselage. King (1984) was able to show that the maximum width of the shadow zone (i.e. regions, often larger than the fuselage boundary layer, that do not contain particles of a certain size) occurs out to 0.2 fuselage radius (distanced normalized by the radius of the aircraft fuselage) and airflow departures from freestream velocities occur up to 3 fuselage radii ahead of the nose. Based on the equations of motion derived in King (1984), Drummond and MacPherson (1985) studied the air flow effects on droplets measured by four PMS OAPs on board the National Aeronautical Establishment of Canada's Twin Otter aircraft. Drummond and MacPherson

(1985) found that droplet concentrations are under-sampled by up to 25% for aircraft lift coefficients (i.e. dimensionless coefficient that relates lift to fluid flow around a body) of 0.79 (~4 degrees angle of attack). Aircraft lift coefficients can also be used to describe the relationship between a particular 2-D airfoil and the angle of attack, with the maximum lift coefficient for a given airfoil occurring at the stall angle. MacPherson and Baumgardner (1988) investigated airflow around wing-mounted PMS 2D-C instruments onboard the National Center for Atmospheric Research (NCAR) Beechcraft King Air. After noticing non-symmetrical icing on the outboard 2D-C, MacPherson and Baumgardner (1988) conducted extensive wind tunnel tests of the King Air pylon assembly with chalk and oil, calculating velocity ratios and side flow angles for multiple angles of attack at two sample locations (inboard and outboard). MacPherson and Baumgardner (1988) were able to show a deceleration and turning of streamlines within 0.75 meters of the 2D-C sampling plane, corresponding to droplet relaxation time of 60-micron diameter particles. MacPherson and Baumgardner (1988) suggest that droplets smaller than this size would follow streamline trajectories, but they do not calculate particle trajectories within their study.

Norment (1988) also studied the air flow effects on a PMS 2D-C and a PMS Forward Scattering Spectrometer Probe (FSSP) on board the NASA Lewis Research Center DHC6 Twin Otter aircraft. Similar to Drummond and MacPherson (1985), the PMS instruments used within the Norment (1988) study were mounted behind the leading edge of the aircraft wing. Norment (1988) modeled the potential flow around the Twin Otter wing, PMS canister and specific instruments for two aircraft true airspeeds (49 and 128 ms^{-1}) and two angles of attack (0 and 4 degrees). While the study found that for wing-mounted instruments results are insensitive to freestream air speed, Norment (1988) found that the PMS FSSP under-sampled

cloud droplets (5-50 microns diameter) by 10-13% at 0 degrees angle of attack, and 18-24% at 4 degrees angle of attack.

While these efforts have attempted to create guidelines for instrumentation placement or correction to data from instruments known to be poorly located, instruments are still integrated into research aircraft today on an ad hoc basis to suit structural integrity. Recently, there has been a renewed effort to re-evaluate the air flow and trajectory analysis for individual aircraft and pylon assemblies. O'Brien (2016) observed the preferred, vertical orientation of ice crystals within the sample volume of the Stratton Park Engineering Company (SPEC, Inc) Two-Dimensional Stereo Probe (2D-S) OAP on board the University of North Dakota Citation II Research Aircraft, suggesting an induced electric field on the aircraft (along with airflow deceleration) was responsible for the particle orientations.

Following discussions about their unique under-wing (and behind the leading edge) pylons on the Facility for Airborne Atmospheric Measurement's (FAAM) BAe-146-301 aircraft flown during ORACLES-2017, Bennett et al. (2019) performed a computational fluid dynamics investigation to understand the aerodynamics around their pylon assembly. Using ANSYS Fluent (version 16), Bennett et al. (2019) were able to produce solutions for compressible flows via an implicit, steady-state, density-based solver that was independently verified with observations from the Droplet Measurement Technologies (DMT) Aircraft-Integrated Meteorological Measurement System (AIMMS). While Bennett et al. (2019) only considered the effect of longitudinal and lateral velocity components on the sizing of hydrometeors within the DMT Cloud Imaging Probe (CIP-100), it nevertheless shows the ability of the current state of CFD to accurately produce the aerodynamics around aircraft instrumentation. Spanu et al. (2020) conducted numerical simulations for compressible flows

with Reynolds-Averaged Navier-Stokes equations (RANS), a Launder-ShamaK ϵ turbulence model, and Lagrangian particle tracking within OpenFOAM (version 4.0x) to investigate flow around wing-mounted instruments on board the DSR Dassault Falcon 20E. Through these simulations, Spanu et al. (2020) were able to determine the sampling efficiency (i.e. concentration of particles within the sample volume compared to free stream concentrations) for the DMT Cloud and Aerosol Spectrometer. At typical cloud sampling conditions (100 ms⁻¹ true airspeed, and static pressure 900 mb), cloud droplets less than 100 microns in diameter were shown to have a sampling efficiency of 77%, where droplets larger than 100 microns were shown to be minimally affected (Spanu et al. 2020).

COMPUTATIONAL FLUID DYNAMICS

Computational Fluid Dynamics (CFD) is a computer aided engineering tool designed around the Navier-Stokes equations, or the conservation equations of mass, momentum, and energy, to accurately model physical phenomena (Moukalled et al. 2016a). The Navier-Stokes equations can be expressed in a general conservation equation [Eq. 1], which describes the transport of any physical property ϕ

$$\frac{\partial}{\partial t} (\rho\phi) + \nabla * (\rho\mathbf{v}\phi) = \nabla * (\Gamma^{\phi}\nabla\phi) + Q^{\phi} \quad [1]$$

where:

$$\text{Unsteady Term: } \frac{\partial}{\partial t} (\rho\phi)$$

$$\text{Convection Term: } \nabla * (\rho\mathbf{v}\phi)$$

$$\text{Diffusion Term: } \nabla * (\Gamma^{\phi}\nabla\phi)$$

$$\text{Source Term: } Q^{\phi}$$

Within CFD frameworks, it is common practice to define the specific physical property ϕ in non-dimensional form by dividing by a quantity that has the same physical dimension to

generate solutions that are applicable to dynamically similar problems and to reduce the overall number of variables calculated (Moukalled et al. 2016a). An example of non-dimensional form is to express velocity, temperature and pressure via the Mach number (M) [Eq. 2], which is the ratio of speed of an object moving through a fluid and the local speed of sound (Moukalled et al. 2016a). Mach number is mathematically written as:

$$M = \frac{|\mathbf{v}|}{a} \quad [2]$$

where

$$a = \sqrt{\gamma \left(\frac{\partial p}{\partial \rho} \right)_T}$$

$$\gamma = \frac{c_p}{c_v}$$

Used in a variety of engineering applications and industries, the core numerical method used within CFD frameworks is the finite volume method. Similar to the finite difference or finite element method, the finite volume method is a technique to transform physical properties represented as partial differential equations over a domain into discrete algebraic equations over finite volumes (Moukalled et al. 2016a). The first step of the finite volume method is determination of the physical phenomenon and geometric quantities to model. For instance, within Fig. 3a, to determine horizontal wind speed throughout the domain, geometric information of the obstacle (i.e. building) is needed, as well as, the main physical properties of the domain. Next, the domain is subdivided into discrete non-overlapping elements that yield a grid or mesh system, which is defined by a set of vertices and bounded by faces. To obtain numerical solutions of the Navier-Stokes general conservation equation, values for the

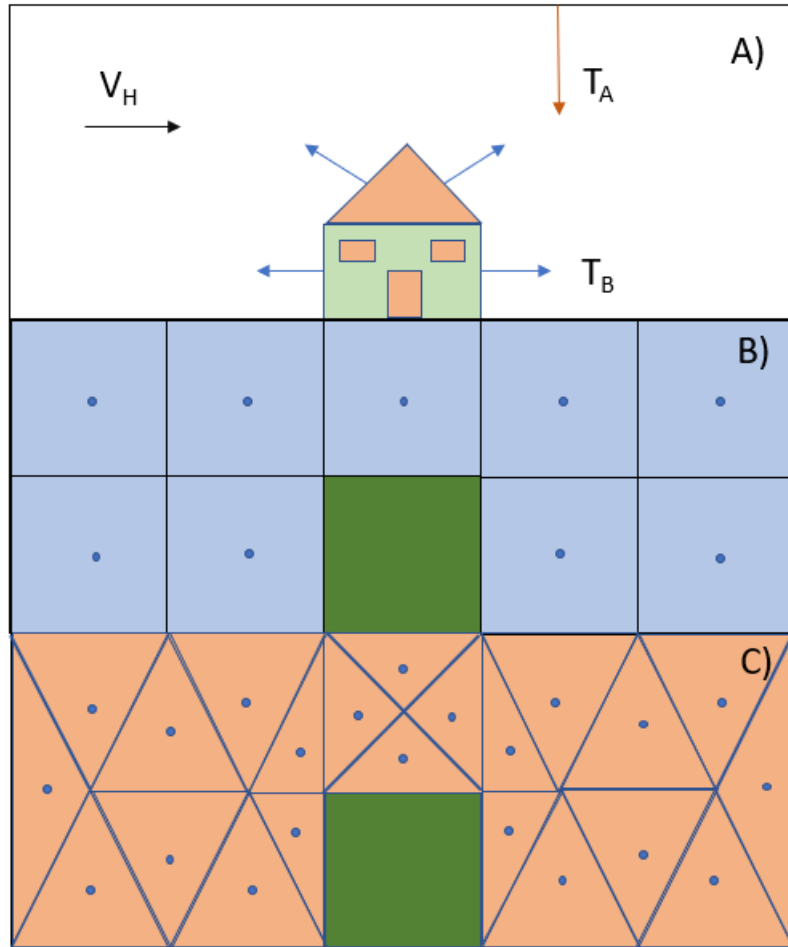


Figure 3: Domain discretization for the simplified example of horizontal wind flow across a building (shown in green), with structured (B) and unstructured mesh (C) and associated centroids.

non-dimensional form of the dependent variable ϕ are found at specific locations, known as grid elements or grid nodes, across the domain in a process called domain discretization (Moukalled et al. 2016b).

As shown in the simplified geometry in Fig. 3, the mesh can be constructed using either a structured or unstructured discretization process. For structured meshes, the domain is constructed of three-dimensional elements defined by local indices (e.g. i, j, k) that contain uniform spatial dimensions, with every interior cell in the domain connected to the same number of neighboring cells. The main advantage of the structured meshes is the

interchangeability of the local indices of each element with global indices of the domain, allowing for the mapping of the system of equations at each node to the full system of equations over the computation domain. While structured meshes allow for ease in computation of gradients and the flux between elements due to this mapping, there is limited geometric flexibility due to implicit communication between elements (Moukalled et al. 2016c). In contrast, unstructured meshes offer increased flexibility in the type of element used, such as polygons with triangular and quadrilateral faces for three-dimensional finite volume mesh. As shown in Fig. 3c, this unstructured discretization allows for the increased concentration of computational nodes around the simplified building geometry compared to the structured mesh. Unstructured mesh elements are not defined by local indices but are numbered sequentially (as are element faces, nodes, and other geometric features) starting with an arbitrary element (Moukalled et al. 2016c).

Explicit geometric information is needed in order to relate elements to each other. For an individual element, the index, the centroid, a list of bounding faces and a list of neighboring elements are required. For a face, the number of vertices comprising the face, the list of neighboring elements, the surface vector, the centroid and index must be known. Lastly, the faces that define the boundaries of the computational domain are required. With explicit defined relations between elements, unstructured discretization allows for heterogeneity within element creation.

Along with the discretization of the domain into a mesh, a critical component of the finite volume method is the discretization of the governing partial differential equations across the domain into sets of algebraic equations linking the value of the dependent variable at an element to its neighbors (Moukalled et al. 2016b). This is accomplished within two steps, the

first by applying a Gaussian quadrature to the volume integral of the source term and the surface integral at each element face to create a semi-discrete governing equation (Moukalled et al. 2016c). For any total flux \mathbf{J}^ϕ , using the Gaussian quadrature, the integral at the face f of the element is

$$\int_f (\mathbf{J}^\phi * n) dS = \sum_{ip \sim ip(f)} (J^\phi * n)_{ip} \omega_{ip} S_f \quad [3]$$

where $ip(f)$ is the number of integration points along surface f , ip refers to the integration point, ω_{ip} is the weighing function per integration point and S_f is the surface vector for the individual face (Moukalled et al. 2016c). Although accuracy increases with the number of integration points (and computational cost), typically, one value is chosen as the integration point, which is the centroid of the element or face. Assuming a steady state solution, Eq. 2 can be converted to a semi-discrete version for element C by

$$\sum_{f \sim nb(C)} (\rho \mathbf{v} \phi - \Gamma^\phi \nabla \phi)_f * S_f = Q_C^\phi V_C \quad [4]$$

Through integration of these equations over the mesh elements, and by replacing the volume integrals by surface integrals through the use of the divergence theorem, the governing equations can then be written as surface fluxes that are evaluated at the faces of the element. The second step of the discretization of the governing equations is to split these surface fluxes into linear (independent) and non-linear (dependent) parts, which describe how the physical quantity ϕ changes between faces. The final algebraic relation of the physical quantity ϕ , which is described by values (ϕ_C and ϕ_F) at the face between element C and element F as

$$a_c \phi_c + \sum_{F \sim NB(C)} (a_F \phi_F) = b_c \quad [5]$$

where

$$a_c = \sum_{f \sim nb(C)} Flux_{C_f} - Flux_C$$

$$a_F = FluxF_f$$

$$b_C = - \sum_{f \sim nb(C)} FluxV_f + FluxV$$

These algebraic equations are then assembled into a global matrix, whose rows and columns correspond to each element of the domain in the form of

$$\mathbf{A}[\mathbf{T}] = \mathbf{b} \quad [6]$$

where \mathbf{A} is a matrix of coefficients in Eq. 5, $[\mathbf{T}]$ is the solution vector, and \mathbf{b} is a vector of terms that cannot be included in \mathbf{A} .

While it is possible to obtain a solution to this global matrix utilizing matrix inversion, for an $N \times N$ matrix, it is computationally expensive as the operation count is on the order of N^3 (Moukalled et al. 2016d). Therefore, numerical solutions to the finite volume method employ an iterative method, which repeatedly solves the discrete system of equations across the domain by:

- i) Initial guess of discrete values of ϕ across the domain at each grid element
- ii) At each grid element ϕ_C , update discrete value utilizing [5]
- iii) Iterate across the domain, with updated values of ϕ_C influencing ϕ_F
- iv) Check if appropriate convergence criterion has been met. Otherwise, repeat.

The convergence criterion is dependent on the physical property ϕ that is modeled, with a typical requirement of a less than one percent maximum change in the grid point values for that iteration. The computational advantage of this approach is the minimum storage required as only the discrete values of the physical property are recorded at the grid point (Moukalled et al. 2016d). With the discrete values of the surrounding elements known, the individual value of any element can be updated through the iteration process.

INCOMPRESSIBLE FLUID FLOW COMPUTATION

As described above in Section 2a, previous studies have investigated airflow around the fuselage of an aircraft through the modeling of incompressible fluid flow, which assumes that density is constant within a fluid parcel. To represent incompressible flows within computational fluid dynamics, the general conservation Eq. 1 is expressed in equations similar to the continuity and momentum equations

$$\frac{\partial \rho}{\partial t} + \nabla * (\rho \mathbf{v}) = 0 \quad [7]$$

$$\frac{\partial}{\partial t} [\rho \mathbf{v}] + \nabla * \{\rho \mathbf{v} \mathbf{v}\} = -\nabla p + \nabla * \{\mu [\nabla \mathbf{v} + (\nabla \mathbf{v})^T]\} + \mathbf{f}_b \quad [8]$$

However, an issue arises due to the unavailability of an explicit equation for computing the pressure field within Eq. 8, requiring a reformatting of the Navier-Stokes equations to account for this issue (Moukalled et al. 2016e). The pressure equation is constructed through combination of the discretized Eq. 7 and Eq. 8 and solved with the Semi Implicit Method for Pressure Linked Equations (SIMPLE) technique, where the velocity and pressure fields are solved sequentially to satisfy mass and momentum conservation (Moukalled et al. 2016e).

Critical to the accuracy of any pressure-based fluid flow within CFD models is the treatment of momentum and pressure-correction equations at patch boundaries, or the domain edges (Moukalled et al. 2016e). Known as boundary conditions, these conditions describe the limits on the solution fields within the faces that surround these patches. For the momentum equation, a no-slip or slip boundary condition is generally applied for a moving or stationary wall, which can be an internal or external hard surface (Moukalled et al. 2016e). For a no-slip wall boundary, the velocity of the fluid at the wall is equal to the velocity of the wall, forcing a shear stress from the boundary element centroid to boundary face (Moukalled et al. 2016e). This shear stress ultimately creates a boundary force, normal towards the patch boundary and

a boundary pressure, which can be extrapolated from the boundary element centroid assuming the mass flux is zero to the boundary. For a slip wall boundary condition, the wall shear stress is zero, resulting in zero boundary force (Moukalled et al. 2016e) and a step function in velocity from the element centroid to boundary face.

To simulate fluid flow through the domain, an inlet and outlet boundary condition are set, detailing how the momentum field (and thus mass flow) enters and exits the domain in two-dimensions. For the momentum equation, the inlet boundary conditions are known as specified velocity and specified total pressure and velocity direction (Moukalled et al. 2016e). For specified velocity, using known values of velocity and mass flow rate, the convection and diffusion terms of Eq. 1 can be calculated, which results in solutions for the pressure at the boundary (Moukalled et al. 2016e). For the case of specific total pressure (p_o) and velocity direction, the boundary pressure is known directly through the relationship

$$p_o = p + \frac{1}{2}\rho\mathbf{v} * \mathbf{v} \quad [9]$$

With use of the continuity equation and velocity unit vector (specified as input), the mass flow rate at the boundary is computed, and thus the velocity at the boundary can be solved at every iteration (Moukalled et al. 2016e). For the momentum equation, two types of outlet boundary conditions are commonly used specified static pressure and fully developed flow. For the specified static pressure outlet boundary condition, the velocity at the outlet is equal to that of the boundary element, implying zero velocity gradient (Moukalled et al. 2016e). For the following developed flow condition, the velocity gradient normal to the outlet is assumed to be zero, and the pressure at the boundary is extrapolated from the interior pressure field, allowing velocity to be treated as known via the momentum equation (Moukalled et al. 2016e).

COMPRESSIBLE FLUID FLOW COMPUTATION

An advantage of a pressure based approach, such as the SIMPLE method, within computational fluid dynamics was the ability to resolve flows for various aerodynamic flow regimes (Moukalled and Darwish 2016). The most common approach to differentiate aerodynamic flow regimes is through the Mach number at an arbitrary point within the flow field (Anderson 2003). Subsonic flow fields contain Mach numbers less than one ($Ma < 1$) throughout the domain, are characterized by streamlines without discontinuities in slope (i.e. smooth) and disturbances within the flow propagate both upstream and downstream throughout the entire flow field (Anderson 2003). Transonic flows occur for freestream Mach numbers in the range of $0.8 < Ma < 1.2$ and occur in regions locally supersonic (such as airflow over the trailing edge of an airfoil) within ambient subsonic flows. Transonic flows typically contain weak shock waves generated in the trailing edge of the airfoil in a “fish-like” pattern (Anderson 2003). Supersonic fluid flows are defined for flows where the Mach number is greater than one ($Ma > 1$) for every point within the flow field and are frequently characterized by the presence of a shock wave (e.g. large discontinuity in flow properties and streamlines) (Anderson 2003). In contrast to subsonic flows, disturbances created within supersonic fluid flows cannot propagate upstream since the local flow velocity is greater than the speed of sound (Anderson 2003). Hypersonic fluid flows contain Mach numbers between five and twenty-five ($5 < Ma < 25$) and are dominated by viscous interactions in the region between the shock wave and moving body (Anderson 2003).

To properly resolve these key aerodynamic regime features, the thermodynamics of the fluid flow field need to be incorporated into the governing equations, which is the basis for a compressible fluid flow model framework. The key difference between incompressible and

compressible fluid flow is the density of the fluid becomes variable with increasing Mach number, requiring explicit calculation. To resolve fluid flow across all key aerodynamic regimes, the pressure-based SIMPLE approach allows for the calculation of the density field through the equation of state, while also calculating the velocity field via the momentum equation. In addition to [7] and [8], the conservation equations for compressible flow include the energy equation expressed in terms of temperature

$$\frac{\partial}{\partial t}(\rho c_p T) + \nabla \cdot [\rho c_p \mathbf{v} T] = \nabla \cdot [k \nabla T] + \rho T \frac{Dc_p}{Dt} + \frac{Dp}{Dt} - \frac{2}{3} \mu \Psi + \mu \Phi + \dot{q}_v \quad [10]$$

From Moukalled and Darwish (2016), the SIMPLE algorithm for compressible fluid flow follows as such:

1. The solution is started at time t for pressure, velocity, density, temperature and mass flow rate fields as the initial guesses (i.e. boundary conditions).
2. Solutions of the momentum equation to obtain a new velocity field v^* are found.
3. The equation of state is used to calculate a new density field ρ^* .
4. The mass flow rates at the control volume faces are updated to obtain a momentum satisfying mass flow rate, m^* .
5. With the new mass flow rates, the coefficients of the pressure corrections are found and applied to obtain a pressure correction field p' .
6. The pressure, density and velocity fields at the control volume centers and the mass flow rate at the control volume faces are updated to obtain continuity-satisfying fields.
7. The energy equation is solved to obtain a new temperature field T^* .
8. Set v^* , ρ^* , T^* , p^* , and m^* as the initial guess for velocity, density, temperature, pressure, and mass flow.

9. If a solution does not meet convergence criteria, the algorithm goes to step two and repeats.

MOTIVATION

To have accurate in-situ cloud microphysical measurements, the volume of air sampled at the instrument location must be known. Typically, to simplify these sample volume measurements, it is often assumed that the sampling locations are representative of freestream (i.e. undisturbed, unaltered, upstream) atmospheric flow. However, pressure perturbations ahead of the aircraft and the instruments themselves are known to alter particle trajectories at the sample volumes of the instruments. Additional deviations of relative airflow speed and direction occur at the instrument location as the aircraft undergoes maneuvers during flight. The overall concern is that uncertainty due to sampling location may be larger than the uncertainty due to determining the sample volume. To minimize uncertainty due to these perturbations, instruments are typically mounted on pylons that extend the sample volumes to a location some distance away from the aircraft. The P-3 aircraft used underwing pylons for mounting probes outboard of the aircraft engines. While the goal of this placement is to have instruments sample freestream conditions, there is no standardization of pylon configurations that would accomplish this goal for wing mounted instrumentation. Additionally, it is currently unknown if instruments should be mounted ahead or behind the leading edge of the aircraft wing to achieve freestream conditions. Historically, instruments have been mounted ahead of the leading edge of the aircraft wing, which is why the original pylon configuration (“Navy pylon”) on the NASA P-3 (Fig. 4a) was concerning. To address these concerns, a new pylon configuration (“Extended pylon”) was developed by the NASA Wallops Island Flight Facility engineers to allow the instrumentation to be located as far below and ahead of the leading edge

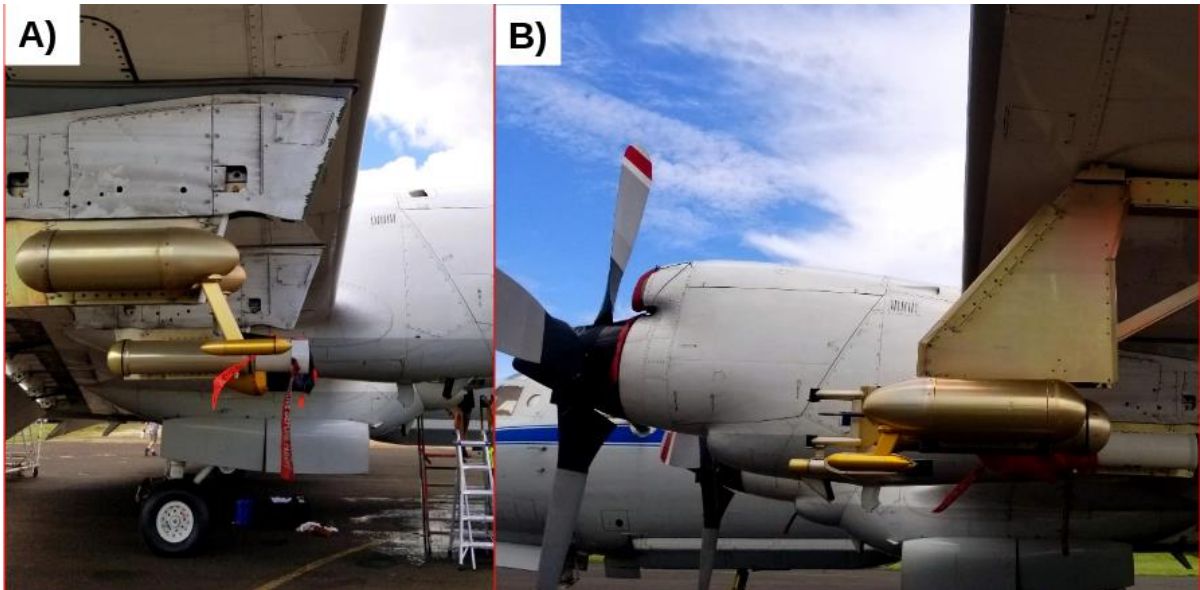


Figure 4: Cloud Droplet Probe (CDP) mounting locations with respect to the leading edge of the wings on-board the NASA P-3 Orion during the ORACLES 2018 field experiment in Sao Tome. Figure 1-A (Figure 1-B) contains the Navy (Extended) pylon design with the Langley Airborne Research Center (Uni. Of Hawaii) CDP.

of the aircraft wing as possible to sample within the freestream. The extended pylon shown in Fig. 4b, was manufactured for the ORACLES-2017 campaign and installed at the outboard pylon location of the left wing. To help determine which pylon configuration provided observations that were most representative of the marine stratocumulus cloud environment, analysis of simultaneous observations from two CDPS were used during ORACLES-2018. After eight research flights, pylon locations of the two CDPs were swapped in order to minimize the effect of each specific instrument on the analysis. While the relative difference in concentrations between pylons configurations is shown with this CDP comparison, there continues to be questions about which configuration would provide data that are more representative of the stratocumulus cloud environment.

OBJECTIVE

A computational fluid dynamical (CFD) study of the NASA P-3 pylon configurations would offer the opportunity to determine which configuration allows for the better

representation of the cloud environment. Additionally, a CFD analysis would allow for increased confidence in the suitability of the NASA P-3 aircraft for future cloud microphysical missions. The objective of this proposed study is to determine the effects of airflow on the measurements made by cloud microphysical instrumentation installed behind the leading edge of the aircraft wing, where the majority of the ORACLES in-situ cloud microphysical data were obtained. Through a CFD analysis of the NASA P-3 pylon configurations used during ORACLES, we will address the following scientific questions:

- 1. What is the sampling efficiency of cloud droplets at the instrument mounting location for the Navy and Extended NASA P-3 pylon configurations?**
- 2. For future cloud microphysical missions, should wing-mounted instruments sample ahead or behind of the leading edge of the aircraft wing?**

CHAPTER III METHODOLOGY

Computational Fluid Dynamics – OpenFOAM

Previous analysis into airflow around the DMT Cloud-Aerosol-Precipitation Spectrometer (CAPS) by Spanu et al. (2020) has demonstrated the usefulness of the Open Source Field Operation and Manipulation (OpenFOAM) package for atmospheric research. OpenFOAM is open source CFD software owned by the OpenFOAM foundation, distributed under a General Public license and was created in the C++ programming language with an object-oriented coding approach (Jasak et al. 2007). OpenFOAM uses the finite volume method and the C++ operator overloading feature to represent and evaluate partial differential equations through a series of scalar-vector operations (Chen et al. 2014). A particular benefit of OpenFOAM's approach is that users can understand the syntactical language of the code due to its mimicking of mathematical formula. The open-source nature of OpenFOAM allows for the development of community code and tutorials for researchers starting out with CFD analysis and removes the high purchase cost of commercial CFD software, while allowing simulation processing on high performance computing resources.

The OpenFOAM distribution core has two categories: solvers and utilities (Greenshields 2017). Solvers are an organized structure of iterative linear algebraic equations, determined through the discretization process described in Chapter 2. The role of solvers within the OpenFOAM distribution is the collection of critical information related to gradient schemes and multigrid algorithms (Moukalled et al. 2016f). Solvers are subdivided into preconditioners and smoothers. Preconditioners are approximate solutions to the direct numerical solution of the global matrix and are used to promote the convergence rate for the chosen numerical solver.

(Moukalled et al. 2016f). Smoothers are techniques to reduce low frequency error components within iterative solvers through the use of multigrid methods, which is the process of including fine and coarse mesh elements within the domain. Smoothers promote convergence of the solver solutions by transforming low frequency errors within fine mesh elements to high frequency errors at a coarser mesh element (Moukalled et al. 2016f).

Utilities contain scripts and modules for pre-processing and post-processing each simulation. Pre-processing involves the generation and manipulation of simple or complex volumetric meshes, supporting structured and unstructured grids in two-dimensional or three-dimensional space for each solver. Post-processing of solutions allows for sub setting the numerical solutions for regions or points of interest, calculating additional gradients or physical quantities of interest, and visualization of the solutions.

The OpenFOAM distribution can be downloaded from the OpenFOAM foundation website (<https://openfoam.org/>) via Docker, which allows the user to download the code base into a compartmentalized container that has specific software and configuration files needed for a given operating system. For this research, OpenFOAM version 8 (released 22nd July 2020; <http://dl.openfoam.org/docker/openfoam8-linux>) was selected for use on RedHat operating systems at the University of North Dakota.

OPENFOAM – NASA P-3 CASES

To investigate the airflow around the NASA P-3 for the Extended and Navy pylon configurations, simulations of both pylon configurations will be conducted for the in cloud profiles flown during ORACLES (e.g. sawtooths and level cloud legs). To conduct this analysis with OpenFOAM, multiple levels of processing are needed to accurately transform conceptual diagrams into successful airflow solutions. First, utilizing OpenFOAM pre-

processing utilities, accurate representation of the NASA P-3 with both pylon configurations are created within the OpenFOAM domain. Second, determination of the OpenFOAM solvers (including conditioners and smoothers) and governing equations to simulate airflow around the NASA P-3 models are needed. Upon selection of the appropriate solver, boundary conditions definitions are required for the domain patches, as well as, nondimensional variables calculated by the solver. Additionally, multiple solutions to the OpenFOAM solver are required for sensitivity testing of the input boundary conditions chosen for the simulations. The added benefit of these multiple solutions is it allows for testing of multiple environmental conditions observed during ORACLES. With the ensemble of airflow solutions for the NASA P-3 pylons, the OpenFOAM postprocessing utilities will be utilized for simulating hydrometeors within these solutions

It is important to note that any change to the orientation of the aircraft within the domain would require reprocessing of the snappyHexMesh algorithm, the angle of attack was implemented within each simulation by altering the three dimensional velocity components of the input patch within the U initialization file.

OPENFOAM – PRE-PROCESSING

To achieve quality results within OpenFOAM, realistic models of the desired pylon configurations are needed for numerical calculations. Three-dimensional computer-aided design (CAD) models of the NASA P-3 pylon configurations, with associated instrument canisters and instruments, were provided by the NASA Wallops Island Flight Facility and shown in Figure 5. With the FreeCAD software package, additional CAD models of both pylon configurations attached to the P-3 wing hard-points at Station 9 (furthest outboard, port-side location) were created from the NASA Wallops Island Flight Facility CAD models. FreeCAD

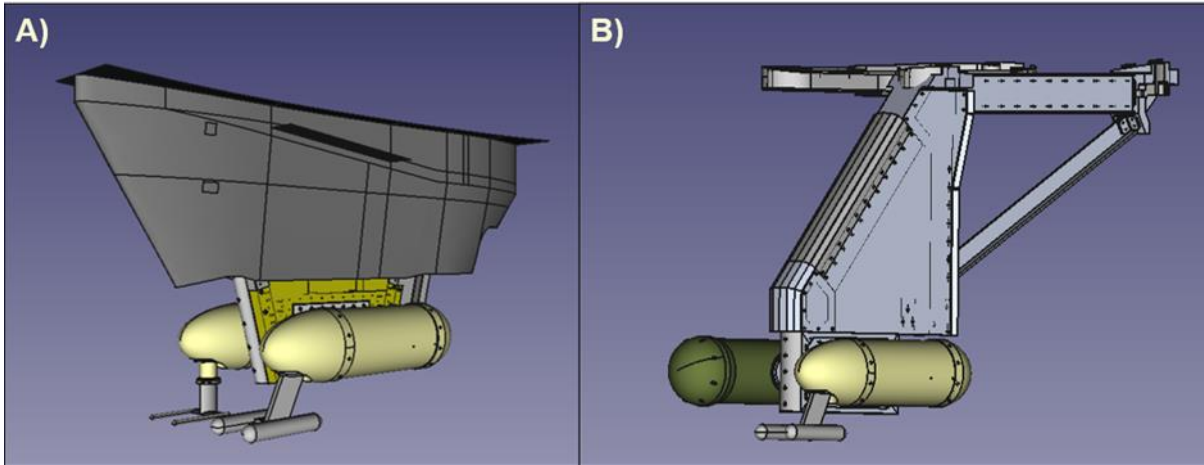


Figure 5: Three-dimensional computer-aided design (CAD) models of the NASA P-3 Navy pylon configuration (Figure 2-A) and Extended pylon configuration (Figure 2-B). Each configuration contains designs for the Cloud Droplet Probe and “bullet” canister used during ORACLES 2018.

is an open-source, three-dimensional parametric CAD modeling application that allows users to produce models of objects for a variety of sizes and purposes (Riegel et al. 2020). The primary use of FreeCAD is to generate meshes from solid geometries for three-dimensional printing. The mesh generation features of FreeCAD allow for the length between each node to be specified to dictate how the surface mesh conforms to the geometry surface. Once the NASA P-3 pylon configurations were assembled, surface meshes of the assembly were created within FreeCAD. Due to limited computational allowances, the length between surface nodes for the P-3 fuselage were set to ten millimeters (10 mm). The length between surface nodes for the P-3 pylon and OAP canisters were set to the maximum resolution of a hundred microns (0.1 mm). The NASA P-3 pylon configuration surface meshes were saved in the Wavefront OBJ file format, a human readable format that represents three-dimensional geometry by storing the position of each vertex. Due to the differences in the native units between FreeCAD and OpenFOAM, the entire P-3 pylon configuration surface mesh was scaled by one thousandth (1/1000) to convert saved vertex positions from millimeters to meters.

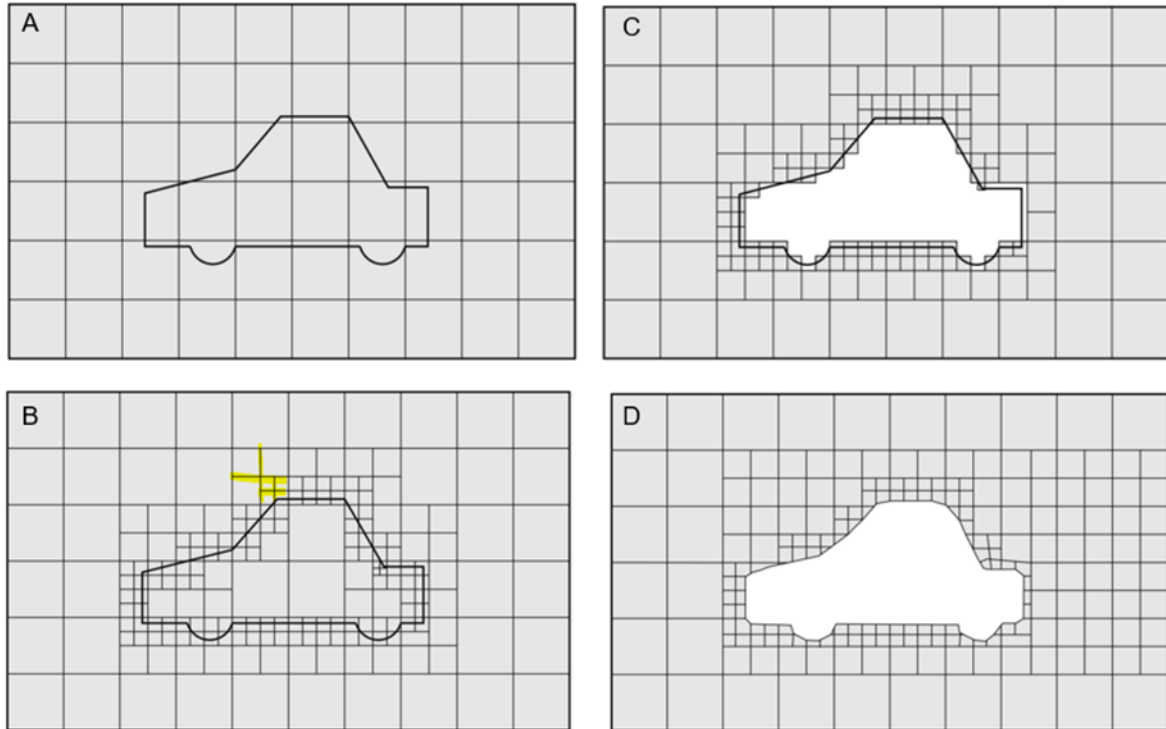


Figure 6: Example of the mesh generation from the *snappyHexMesh* meshing utility, detailing the structure outline (a), splitting of the domain around this structure (b), removal of interior cells (c), and incorporation into the domain (d). Figure is a modification of Figure 5.8, Figure 5.10, Figure 5.11, and Figure.13 within Greenshields 2016).

To generate the volume mesh within OpenFOAM, a simplistic three-dimensional cubic domain is first created with the *blockMesh* utility. Similar to previous studies (King 1984; Norment 1988; Spanu et al. 2020), the domain is configured to be 10 times the length of the pylon assembly in order to minimize the effects of domain boundaries, resulting in a volume mesh three hundred meters in length in each dimension. To incorporate the complex surface mesh of the P-3 pylon configurations generated by FreeCAD into the volume mesh, the OpenFOAM utility *snappyHexMesh* is used to conform the volume mesh to the CAD model surface. As shown in Fig. 6, *snappyHexMesh* chisels the volume mesh to the geometry surface by splitting each volume mesh cell overlapping the position of the geometry surface mesh and iteratively refining each cell to snap to the object surface. To do this, the edges of the surface mesh are first defined with the *surfaceFeatureExtract* utility (Fig. 6a). Cell splitting is

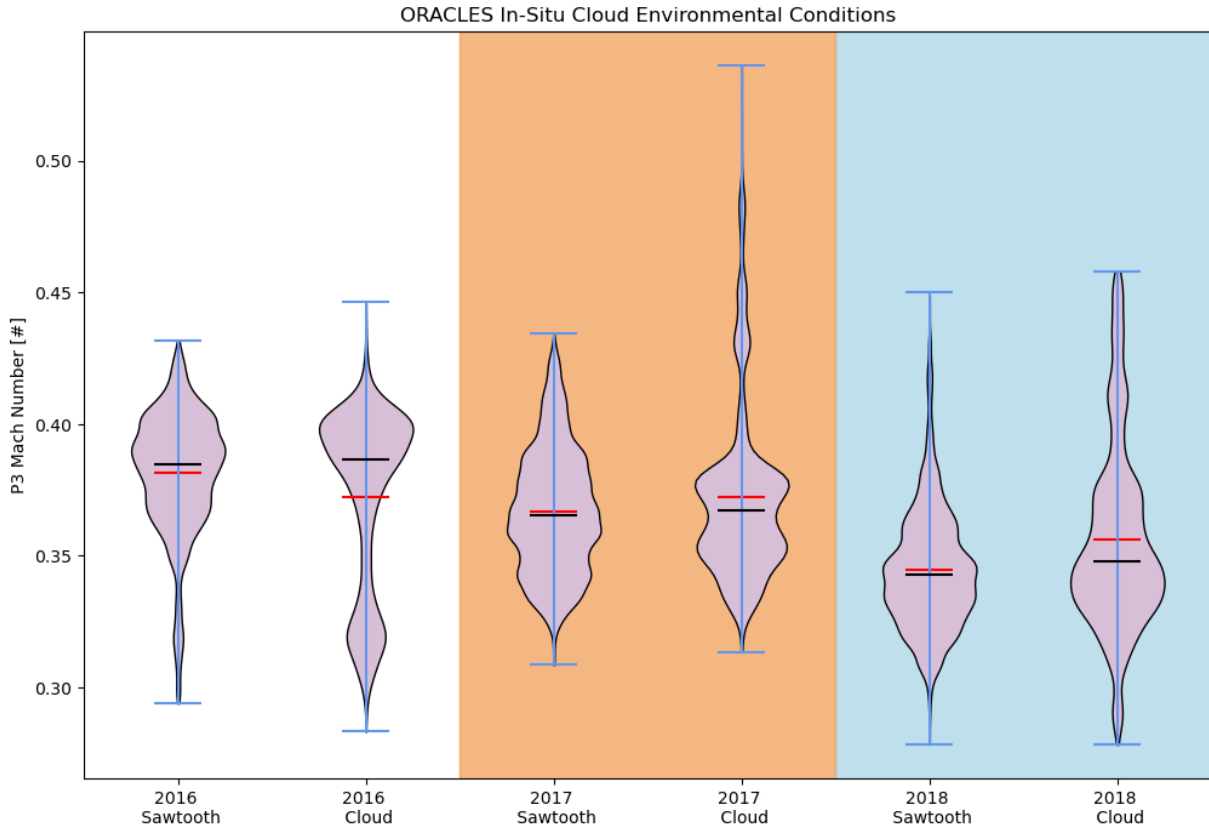


Figure 7: Mach Number for the NASA P-3 Orion during in-situ cloud sampling throughout ORACLES. Shading for each violin plot represents data distribution. Red (black) lines indicate mean (median) of the distribution.

performed on the edges specified by this utility and then across the surface of the geometry (Fig 6b). After every cell on the parameter of the geometry has been split, if desired, boundary layer cells are added on the perimeter of the geometry (Fig. 6c). Finally, cells and edges within the geometry parameter are removed to “snap in” the surface mesh (Fig. 6d). All of these features are controlled by the *snappyHexMeshDict* configuration file within the openFOAM case. The *snappyHexMesh* configuration for the NASA P-3 pylon analysis is contained in Appendix A.

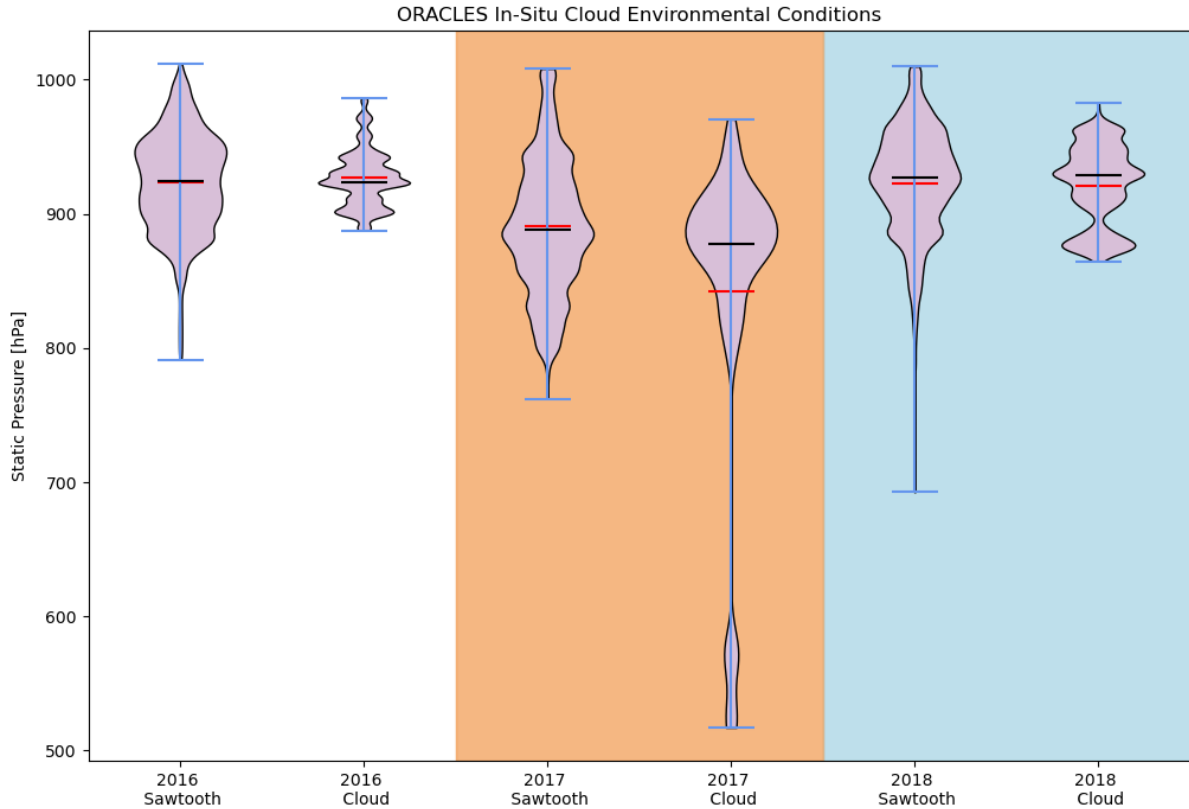


Figure 8: Static Pressure for the NASA P-3 Orion during in-situ cloud sampling throughout ORACLES. Shading for each violin plot represents data distribution. Red (black) lines indicate mean (median) of the distribution.

OPENFOAM - SOLVER

In each of their studies, Bennett et al. (2019) and Spanu et al. (2020) raise concerns on the validity of airspeed calculations within King (1984) due to the assumption of an incompressible fluid. As aircraft speed approaches 0.3 Mach, air density can no longer be considered independent of velocity, and using Benouli’s equation for incompressible flow leads to a 10% overestimation of air speed (Spanu et al. 2020). As shown in Fig. 7, the average Mach number of the ORACLES cloud sampling profiles exceeds 0.3 Mach, specifically 0.33 average Mach for sawtooth profiles and 0.36 average Mach for level cloud profiles. Therefore, to accurately describe the flow around the P-3 pylon assembly, an OpenFOAM steady-state solver,

rhoSimpleFoam, will be used to calculate compressible, turbulent flow, using a Semi-Implicit Method for Pressure Linked Equations (SIMPLE) algorithm.

Similar to Spanu et al. (2020), *rhoSimpleFOAM* solver will use Reynolds-Averaged Navier-Stokes equations (RANS) with a shear stress transport (SST) $k-\omega$ turbulence model and a fixed composition thermophysical model, *hePsiTherm*. The SST $k-\omega$ turbulence model was developed to better predict flows with adverse pressure gradients and allows for easier integration throughout a complex mesh, where k is the turbulent kinetic energy and ω is the specific turbulence dissipation rate (Wilcox 1993; Moukalled and Darwish 2016). Within this framework, the specific turbulence dissipation ω is defined as:

$$\omega = \frac{\varepsilon}{C_\mu k} \quad [11]$$

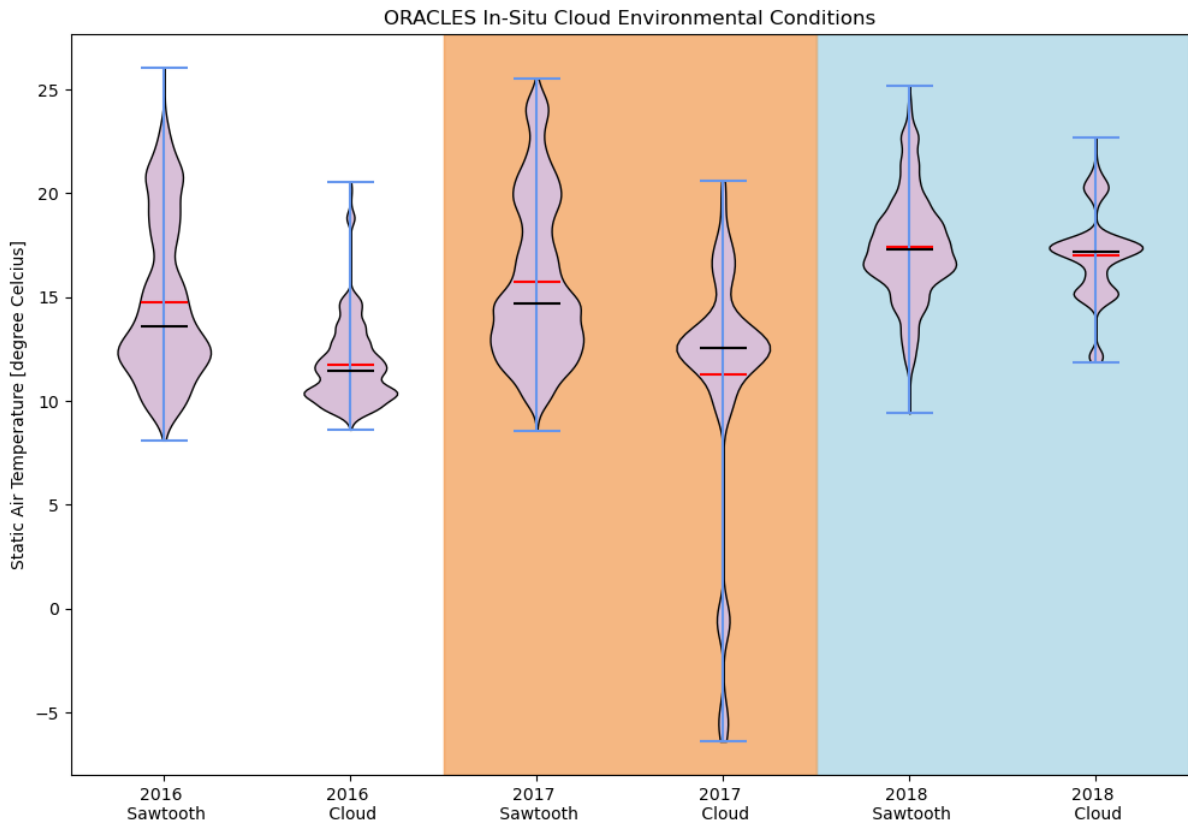


Figure 9: Static Air Temperature for the NASA P-3 Orion during in-situ cloud sampling throughout ORACLES. Shading for each violin plot represents data distribution. Red (black) lines indicate mean (median) of the distribution.

where ϵ is the rate of dissipation of turbulent kinetic energy. From (Moukalled and Darwish 2016), the two conservation equations to define the k- ω model are:

$$\frac{\partial}{\partial t}(\rho k) + \nabla \cdot (\rho \mathbf{v} k) = \nabla \cdot (\mu_{eff,k} \nabla k) + P_k - \beta^* \rho k \omega \quad [12]$$

$$\frac{\partial}{\partial t}(\rho \omega) + \nabla \cdot (\rho \mathbf{v} \omega) = \nabla \cdot (\mu_{eff,\omega} \nabla \omega) + C_{\alpha 1} \frac{\omega}{k} P_k - C_{\beta 1} \rho \omega^2 \quad [13]$$

with the assigned values to the model constraints:

$$C_{\alpha 1} = \frac{5}{9}, \quad C_{\beta 1} = 0.075, \quad \beta^* = 0.09, \quad \sigma_{k_1} = 2, \quad \sigma_{\omega_1} = 2, \quad P_{r_t} = 0.9$$

where

$$\mu_t = \rho \frac{k}{\omega} \quad [14]$$

$$k_t = \frac{\mu_t}{P_{r_t}} \quad [15]$$

$$\mu_{eff,k} = \mu + \frac{\mu_t}{\sigma_{k_1}} \quad [16]$$

$$\mu_{eff,\omega} = \mu + \frac{\mu_t}{\sigma_{\omega_1}} \quad (17)$$

The thermophysical model, *hePsiThermo*, is pressure-temperature system, based on compressibility, that is constructed to describe the energy, heat, and physical properties of a fixed composition, or non-reacting, fluid. Within *hePsiThermo*, a transport model used for

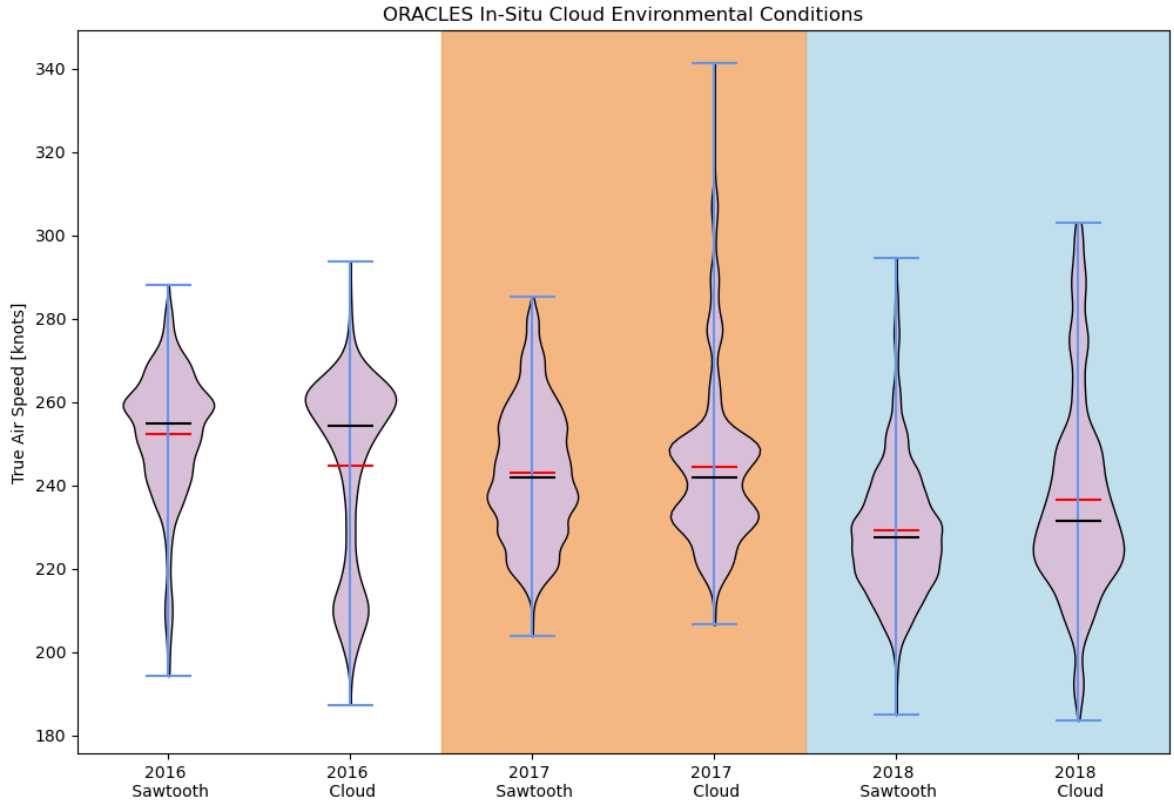


Figure 10: True Air Speed for the NASA P-3 Orion during in-situ cloud sampling throughout ORACLES. Shading for each violin plot represents data distribution. Red (black) lines indicate mean (median) of the distribution.

internal energy and enthalpy calculations is configured to assume constant dynamic viscosity

μ , and the thermal conductivity K is determined by the Prandtl number

$$Pr = \frac{C_p \mu}{\kappa} \quad [18]$$

The model is configured to assume a constant specific heat and heat of fusion, as well as, the equation of state for a perfect gas. The species of the fluid to be modeled is set by the molecular weight, which is configured to air at standard pressure. Each parameter set is included within the *thermophysicalProperties* files within the case directory and can be found in Appendix B.

OPENFOAM – POST-PROCESSING

Along with analysis into the streamlines around the P-3 pylon assembly calculated from the *rhoSimpleFoam* solutions, the sampling efficiency at the instrument sampling location is needed. As in Norment (1988) and Spanu et al. (2020), the sampling efficiency is calculated to be the concentration of droplets at the sampling location compared to the droplet concentration at the domain border. In order to accurately calculate sampling efficiency for the pylon assembly, solutions to describe particle motion within the compressible flow solutions are needed. As in Spanu et al. (2020), an Eulerian-Lagrangian approach is undertaken to solve for one-way coupling of multi-phase flow. As described above, *rhoSimpleFoam* will be used to calculate a solution of the fluid phase (i.e. freestream air). *uncoupledKinematicParcelFoam*, a Lagrangian particle solver, will be used to calculate the Newtonian forces upon a particulate phase (i.e. water hydrometers) using a posteriori methodology. Using the scalar fields calculated within *rhoSimpleFoam*, *uncoupledKinematicParcelFoam* calculates the affect of these scalars on the injection of particles within the simulation.

This analysis assumes a manual injection of particles, such that the three-dimensional position of a simulated ‘cloud’ is defined on the inlet boundary condition with a minute velocity in the direction of flight to initiate motion in the direction of flight. These manual particle injection requires a *particlePosition* file within the *system* directory that requires the three-dimensional location of particles to initiate. From DeCaria (2021), assuming a homogeneous spaced cloud, the probability density function for the nearest neighbor to a specific cloud droplet is:

$$p_{nn}(r) = 4\pi nr^2 e^{\left(-\frac{4}{3}\pi nr^3\right)} dr \quad [19]$$

where r is the radius of the cloud droplet and n is the mean number density. From Eq. 19, the mean distance between cloud droplets is then found as:

$$\bar{r} = \int_0^{\infty} r p_{nn}(r) dr = 4\pi n \int_0^{\infty} r^3 e^{\left(-\frac{4}{3}\pi n r^3\right)} dr \quad [20]$$

With utilization of variable transformation and the gamma function, the mean distance between cloud droplets is:

$$\bar{r} = 0.554n^{-\frac{1}{3}} \quad [21]$$

With Eq. 21, particle positions are created for a fixed mean number density over a finite two-dimensional space, as particles are initiated on the two-dimensional inlet boundary condition. This finite two-dimensional space is centered on the area that the Cloud Droplet Probe sample volume comprises within y-z space of (x-space is the direction of flight) of the domain.

Along with the defined particle positions and manual injection into the simulation, the size distribution of the simulated particles and the particle interaction with the *rhoSimpleFoam* defined patches are required. Particles that interact with the domain edges are removed from the simulation and any particle that interacts with the aircraft, pylons or instrumentation are rebounded downstream within the simulation. Droplet breakup due to the interaction with aircraft are not considered.

We assume a one-way coupling of the multi-phase flows, such that only flow-induced drag forces and gravity are acting on the particles. The influence of particle to particle interactions on the fluid will not be considered. As with Spanu et al (2020), to determine the sampling efficiency of these simulated LaGrangian particles, a kernel density estimation is used to determine the probability density function for a finite space directly ahead of the instrumentation. Comparison of this kernel density estimation for the space ahead of the

instrumentation with a similar space where the particles are initiated will determine sampling efficiency.

OPENFOAM – CASE DIRECTORY

The twelve NASA P-3 OpenFOAM simulations are configured into specific directory structures, which define the governing equations for each simulation, variables of interest, mesh generation, numerical schemes, boundary conditions for each variable, among others. The structure of the case directory for the compressible flow simulations of the NASA P-3 aircraft is described in Fig. 11, with the various boundary conditions to simulate environments observed during ORACLES listed in Table 2. To differentiate between cases, each case is

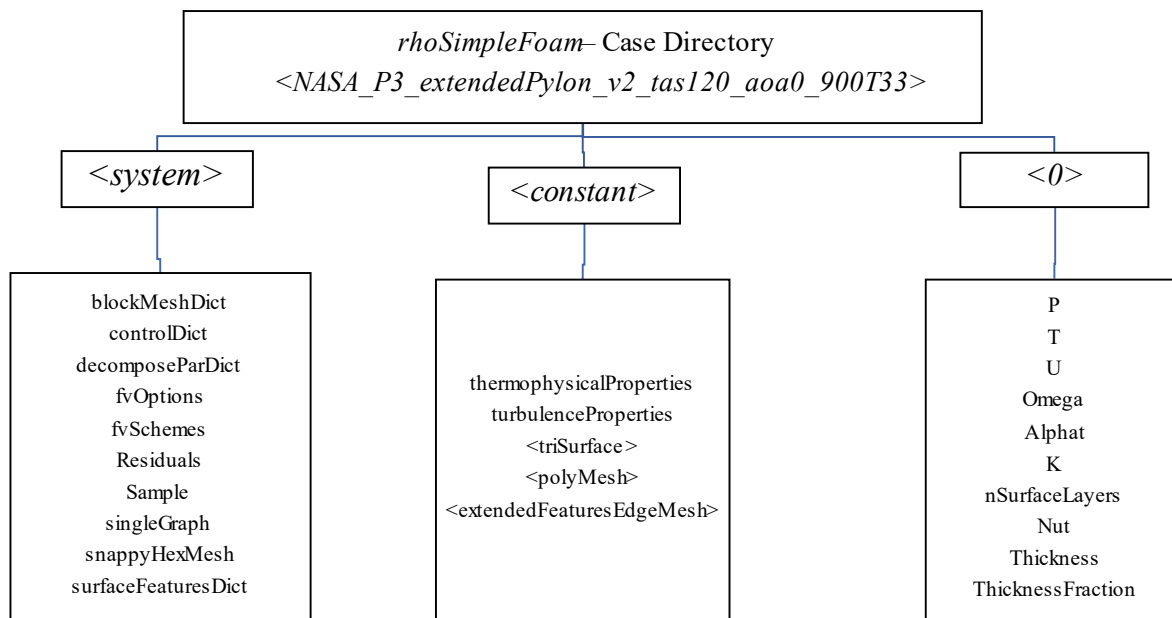


Figure 11: Directory structure for the OpenFOAM solver, *rhoSimpleFoam*, for the *NASA_P3_extendedPylon_v2_tas120_aoa0_900T33* case. Listed are all required files for processing. Names listed within brackets indicate a directory.

structured to contain the airframe, specific pylon, version number, and selected airspeed, angle of attack, pressure and temperature within the name of the directory. The environmental parameters (e.g. pressure, temperature, velocity, turbulent kinetic energy k and specific

turbulence dissipation ω) are each defined in their respective files underneath the initial time directory, 0 . For the velocity file U , the three dimensional velocity components of the inlet patch are set in meters per second, along with the boundary conditions for the volume and surface meshes. For the volume mesh, described by the variable $freestream$, the $freestreamVelocity$ boundary condition

Table 2: Selected OpenFOAM boundary conditions default values for compressible flow simulations. For each default velocity, flow angle is adjusted to simulate three separate angle of attacks.

Pylon Configuration	Freestream Velocity [m/s]	Freestream Temperature [K]	Output Pressure [Pa]	Angle of Attack [°]
Extended	120	303	900	-4, 0, +4
	140	293	800	-4, 0, +4
Navy	120	303	900	-4, 0, +4
	140	293	800	-4, 0, +4

is set to provide freestream velocity throughout the domain. For the surface mesh, described by the variable $wall$, a $noSlip$ boundary condition fixes the velocity to zero on the cells in direct contact with the geometry. For the temperature file T , the temperature of the inlet patch is set in Kelvin and applied uniformly throughout the domain. The volume mesh is given boundary condition $inletOutlet$, which requires the input and output patches of the domain to have the same temperature. The surface mesh is given the boundary condition $zeroGradient$, which extrapolates the temperature of the geometry from the nearest cell value. For the pressure file P , the pressure of the outlet patch is set in pascals, with a $freestreamPressure$ boundary

condition applied to the volume mesh that provides freestream pressure to the domain. Additionally, the surface mesh boundary condition is set to *zeroGradient*, previously described. For the turbulent kinetic energy file *k*, the inlet patch value is set in squared meters per seconds squared, with the volume mesh boundary condition set to *inletOutlet*. For the surface mesh, the *kqRwallFunction* is applied, which provides a wrapper around the *zeroGradient* condition to add specific parameter weights for the sublayer assumptions of the turbulence model. The specific dissipation rate ω is setup similar to the *k* file, with the surface mesh boundary condition set to *omegaWallFunction*. This boundary conditions provides a constraint on the dissipation rate and production of turbulent kinetic energy as determined by the turbulence model. The rest of the files within the *0* directory are related to output from the *snappyHexMesh* algorithm, which defines the layers and thickness of the surface mesh. Each of these files can be found in Appendix C.

Within the *constant* directory, the vertices of every cell within the domain are defined within the *triSurface* directory in a human-readable format. Every cell face and surface are contained within the *polyMesh* directory, with the edges of the surface mesh defined within the *extendedFeaturesEdgeMesh* directory. The parameters for the thermophysical and turbulence models are also included within this directory.

Within the *system* directory, control of the processing (i.e. number of integrations, write control, write style, etc) of the simulation are contained within the *controlDict* file. The *fvOptions* and *fvSolution* files contain the options and interpolation schemes for the simulation. The *residual*, *sample* and *singleGraph* files are used to output specific information from each simulation in human-readable formats for a given set of coordinates within the domain. All of these files are contained within Appendix D.

CHAPTER IV

RESULTS

Twelve simulations of airflow around the NASA P-3 Orion are performed in this study with the computing resources of the University of North Dakota's Department of Atmospheric Sciences. As this is the first study to explore the incorporation of computational fluid dynamics into analysis of atmospheric instrumentation for this department and research group, the fifteen simulations comprised here are the result of a litany of modifications to the configuration files of each solution. These modifications tuned the configuration files to promote convergence of each solution, to create a successful mesh that modeled the NASA P-3 Orion with associated pylons and to allow for parallel processing of each solution. The configuration files stored within the Appendices of this study are the results of these modifications and allow any willing user to re-create these results. The associated standard triangle language (STL) files containing the NASA P-3 Orion Computer Aided Design (CAD) geometry used within this study are available upon request and will be openly available within the author's GitHub repository (<https://github.com/jrobrien91>) after the publication of these results.

Of the many challenges throughout this study, visualization of these solutions proved to have the most complications. As designed, OpenFOAM intends for the user to use ParaView for three dimensional visualization of solutions. ParaView was created by Los Alamos National Laboratory and various government institutions as an application built upon the Visualization Toolkit (VTK), an open source software for manipulating and displaying three dimensional software (Ahrens et al. 2005). ParaView is designed to render OpenFOAM solutions and provide additional layers of processing for multi levels of architecture at the user's disposal, from laptops to high performance computing clusters. However, while an

open-source software, the documentation, user interface and workflow within ParaView was found to be convoluted and incorporation of the software into more atmospheric science applications can be the subject of another dissertation in and of itself.

The main issue with the utilization of ParaView within this analysis was the inability to render the full flow field within a simulation on the University of North Dakota computing infrastructure due to insufficient memory, a known issue with ParaView rendering. To compensate, extensive testing of OpenFOAM post-processing command line interface techniques were performed and applied to the fifteen solutions, resulting in two-dimensional portions of the mesh to be extracted and saved within a VTK extensible markup language (XML) format. As these slices were just a small portion of the overall solution, ParaView was able to input these slices and render the solutions within the University of North Dakota computing infrastructure. However, the process of creating two dimensional slices of the three-dimensional solutions uses post-processing techniques that extracts the centroids of each element along a line resulting in a haphazard view of the mesh within this partition as the mesh resolution increases around the pylons. Additionally, even with these two dimensional slices, ParaView does not allow the user to easily access the data within each element, inhibiting analysis that can be programmed by the user. Finally, the process for determination of the three-dimensional positions of Lagrangian particles and their associated scalar fields within ParaView was painstaking at best, leaving the user a limited ability to add additional calculations of their own. While there have been improvements to the ParaView user experience and documentation with the creation of online message boards via Discourse within the last few years, due to the rampant memory consumption to render solutions, ParaView was abandoned within this study.

An alternative to the standard visualization of OpenFOAM solutions was found after an introduction to the PyVista python library at the 2022 Scientific Python Conference in Austin, Texas. PyVista is a high-level application programming interface for the VTK software package, or a `Pythonic VTK`, which allows for the rendering of mesh data structures and filtering of spatial datasets similar to ParaView (Sullivan and Kaszynski 2019). The significant difference of PyVista is direct array access through NumPy, allowing the user to easily manipulate, display, and perform additional analysis on the dataset. PyVista has had a marked performance improvement on this analysis was its ability to produce full rendered solutions of the flow field around the NASA P-3 Orion, create two-dimensional slices of the mesh interactively, and be fully scriptable to allow for iterative creation of figures. Most importantly, it allows for the user to interact with solution scalar fields within arrays easily. Through a combination of OpenFOAM and PyVista, the resulting solutions successfully demonstrate airflow around the NASA P-3 Orion for a variety of boundary conditions, which are used to simulate environmental conditions explored during ORACLES.

MESH QUALITY

Within each simulation, the CAD files of the NASA P-3 with appropriate pylon configuration is incorporated into the computational domain via *snappyHexMesh* as described in Chapter 3. To evaluate the validity of the mesh generated through this process, the OpenFOAM utility *checkMesh* is applied to each simulation. With the *checkMesh* utility, checks to the mesh statistics, topology, and geometry are performed and summarized with text files included in each simulation. The result of this utility is a conclusion if the mesh used within the simulation is valid. Table 3 contains the number of centroids and faces used to represent each patch within the simulations, with the majority of these features confined to the aircraft geometry with roughly 2.1 million centroids used to represent these aircraft within the

Table 3: Results of the OpenFOAM *checkMesh* utility topology tests for the Navy and Extend Pylon configurations. Shown are the number of points and faces used to represent the domain and geometry for each simulation. The total number of cells, points and faces are consistent between pylon configurations and thus, summarized for each configuration below.

Configuration	Patch	# Points	# Faces
Navy Pylon	Inlet	40000	40401
Navy Pylon	Outlet	40000	40401
Navy Pylon	frontAndBack	80000	80802
Navy Pylon	topAndBottom	80000	80802
Navy Pylon	aircraft	2088931	2316488
Extended Pylon	Inlet	40000	40401
Extended Pylon	Outlet	40000	40401
Extended Pylon	frontAndBack	80000	80802
Extended Pylon	topAndBottom	80000	80802
Extended Pylon	aircraft	2089456	2316621

mesh. Ultimately, roughly 17 million cells were used to represent the NASA P-3 with pylon configurations within the overall 200 cubic meter domain. Table 4 contains the checks to the mesh geometry. The geometry tests within the *checkMesh* utility check to verify the input geometry is located within the overall domain, for the aspect ratio of each face and cell (i.e. ratio between the longest and shortest length), for the difference between the minimum and maximum cell volume, the non-orthogonality between cells (i.e. angle between two cell centroids), and the skewness between cells (i.e. distance between the line intersection between two cell centroids and their common face). Each simulation described within this study successfully passed the *checkMesh* utility and has been confirmed to have a valid mesh.

Table 4: Results of the OpenFOAM checkMesh utility geometry tests for the Navy and Extend Pylon configurations.

Solutions	Max Aspect Ratio	Max Cell Openness	Mesh Non-orthogonality Average	Min Volume	Max Volume
Navy Pylon	16.5085	4.60E-16	7.99	2.18E-07	1.00206
Extended Pylon	16.5085	4.60E-16	7.99	2.59E-07	1.00206

SOLUTION RESIDUALS

For each solution, the OpenFOAM utility *residuals* is configured to track the convergence, or performance, of each simulation. For each equation within the *rhoSimpleFoam* solver, absolute and relative tolerances are defined within the *0* iteration directory for each dependent variable. As the name implies, the *residuals* utility calculates the residual of each calculation for a given equation throughout the mesh. For a matrix system, the residual is defined as

$$r = \frac{1}{n} \sum |\mathbf{b} - \mathbf{Ax}| \quad [22]$$

If the initial residual for each equation satisfies either the absolute or relative tolerance of its dependent variable, the system of equations are assumed to be solved and the solution will not

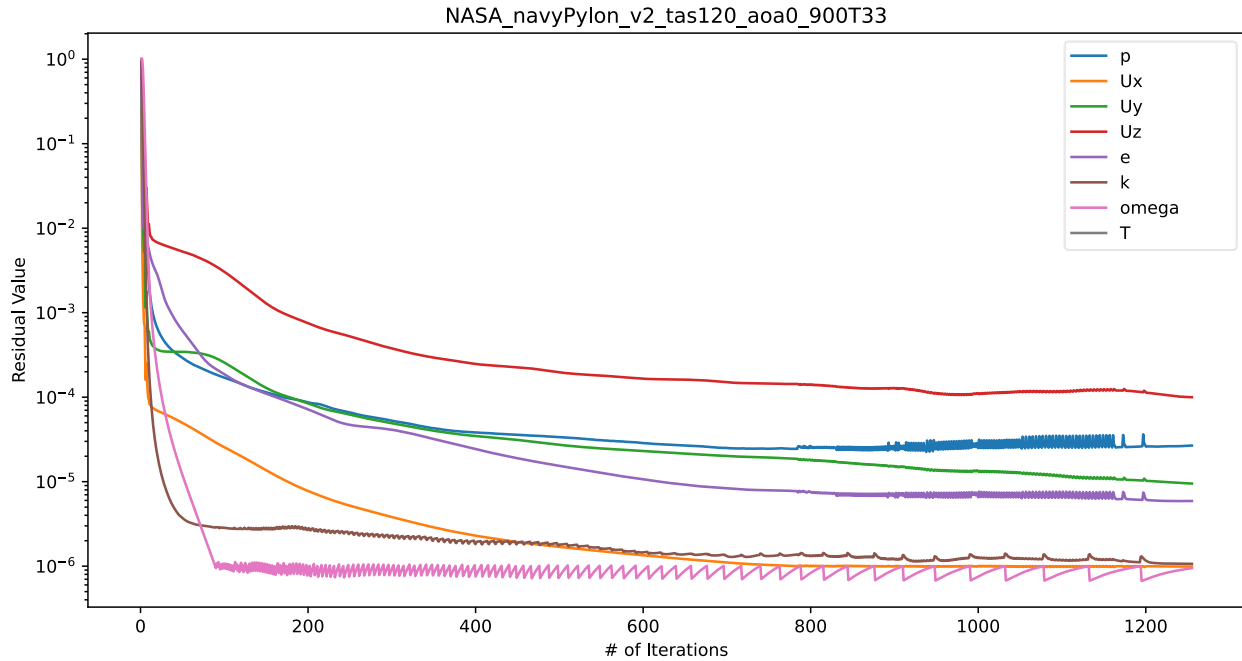


Figure 12: Residual plot of the dependent variables within the rhoSimpleFoam solver for the Navy Pylon solution (True Air Speed – 120 m/s; Angle of Attack = 0° ; Pressure = 900 mb, Temperature = 33C boundary conditions).

evolve further. For unstable simulations, it is therefore possible that the residuals of the governing equations never satisfy the defined tolerances due to rapidly oscillating solutions and will iterate indefinitely. As shown in Figure 12, all variables begin each solution uniform throughout the mesh, resulting in the highest residuals throughout the processing. While some oscillations within the residuals exist within the turbulence variable, this simulation is determined to converge on a solution after 1200 iterations, when all the tolerance thresholds (10^{-4}) are met. An unsatisfactory solution to this simulation would have residuals oscillating to high values with each iteration or a long wave oscillation spanning hundreds of iterations throughout the solution.

Table 5: Final residuals of the dependent variables within the rhoSimpleFoam solver for the final iteration for each NASA P-3 solution.

Solutions	Final Iteration	Pressure	Ux	Uy	Uz	e	k	omega
navyPylon_v2_tas120 aoa0_900T33	1255	2.68E-05	9.88E-07	9.50E-06	9.997E-05	5.90E-06	1.07E-06	9.47E-07
navyPylon_v3_tas120 aoaPos4_900T33	1967	4.06E-05	1.11E-06	3.88E-06	9.97E-05	8.76E-06	1.28E-06	7.11E-07
navyPylon_v3_tas120 aoaNeg4_900T33	3326	3.84E-05	9.14E-07	5.02E-06	9.99E-05	4.19E-06	1.18E-06	7.11E-07
navyPylon_v3_tas140 aoa0_800T20	1265	3.75E-05	1.00E-06	1.01E-05	9.997E-05	7.54E-06	1.16E-06	9.43E-07
navyPylon_v3_tas140 aoaPos4_800T20	3158	4.98E-05	1.21E-06	4.34E-06	9.996E-05	9.74E-06	1.49E-06	9.43E-07
navyPylon_v3_tas140 aoaNeg4_800T20	3212	3.84E-05	9.03E-07	4.48E-06	9.997E-05	3.98E-06	1.02E-06	9.70E-07
extendedPylon_v2_tas120 aoa0_900T33	1238	3.66E-05	1.00E-06	1.06E-05	9.93E-05	7.34E-06	1.22E-06	7.07E-07
extendedPylon_v3_tas120 aoaPos4_900T33	1976	4.44E-05	1.19E-06	3.97E-06	9.99E-05	8.92E-06	1.29E-06	8.92E-07
extendedPylon_v3_tas120 aoaNeg4_900T33	2190	4.09E-05	9.89E-07	5.13E-06	9.98E-05	4.49E-06	9.98E-07	8.50E-07
extendedPylon_v3_tas140 aoa0_800T20	1243	3.86E-05	1.01E-06	1.04E-05	9.93E-05	7.48E-06	1.15E-06	7.23E-07
extendedPylon_v3_tas140 aoaPos4_800T20	2705	5.20E-05	1.27E-06	4.72E-06	9.99E-05	1.07E-05	1.47E-06	8.87E-07
extendedPylon_v3_tas140 aoaNeg4_800T20	6536	4.31E-05	9.14E-07	4.90E-06	9.97E-05	4.24E-06	1.02E-06	9.78E-07

The reasons for a simulation to diverge can be due to improperly set boundary conditions, unphysical values set for the individual patches, or even the architecture of the computing infrastructure. While all NASA P-3 solutions successfully converged with consistent residuals, the negative four degree angle of attack solutions for both pylon configurations required the most iterations. With the creation of the mesh with *blockMesh* and *snappyHexMesh*, processing of the solution with rhoSimpleFoam, and various post-processing utilities, the NASA P-3 navy pylon configuration solution (1255 iterations) shown in Figure 12 required a day to process with six processors on the University of North Dakota computing resources.

NAVY PYLON SOLUTIONS

Six iterations of the NASA P-3 Orion with the Navy Pylon configuration were performed in this analysis with the different initial boundary conditions outlined in Table 2. The first version of this configuration utilized a single processor and the boundary conditions defined

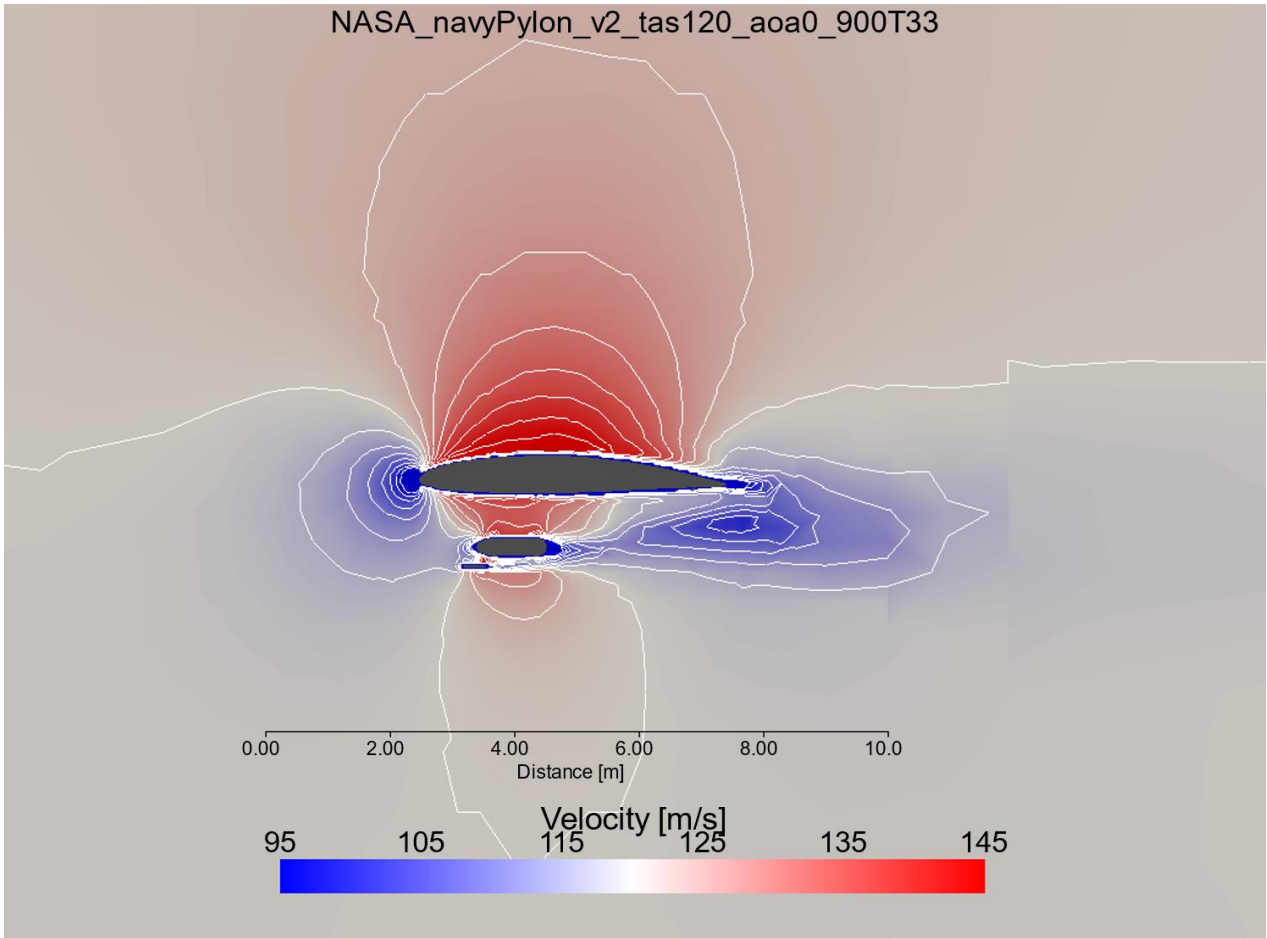


Figure 13: NASA P-3 Orion Navy Pylon configuration showcasing velocity magnitudes with a two-dimensional slice through the solution with a view point along the wing (into the page is towards the fuselage). For this simulation, boundary conditions are: freestream airspeed 120 meters per second, angle of attack zero degrees, freestream pressure 900 millibars and temperature 33 degrees Celsius. Contours represent every 3.33 meters per second difference in velocity.

in Fig. 12. As this first solution for the Navy Pylon configuration took over 168 hours for mesh creation and to converge to a solution, efforts were made to expand the configuration files to incorporate multi-core processing. With the OpenFOAM *decomposePar* function, the domain is equally subset into partitions equal to the number of processors defined within the configuration files, allowing the meshing routine *snappyHexMesh* and solver *rhoSimpleFoam* to process in parallel. The OpenFOAM *reconstructParMesh* and *reconstructPar* functions then allow for the reconstruction of the partitioned mesh and scalar fields to a single coherent solution.

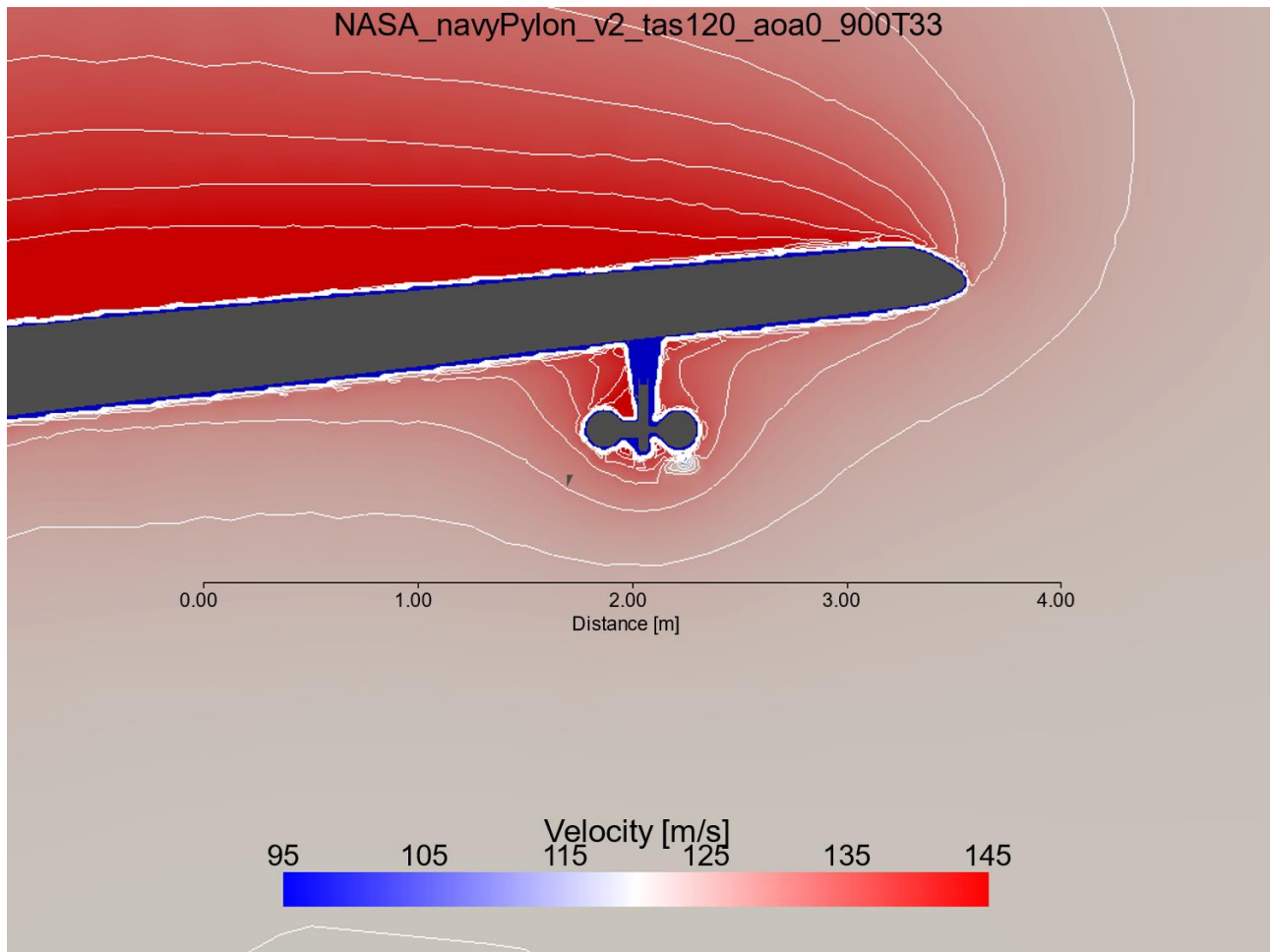


Figure 14: NASA P-3 Orion Navy Pylon configuration showcasing velocity magnitudes with a two-dimensional slice through the solution with a view point along the wing (into the page is towards the fuselage). For this simulation, boundary conditions are: freestream airspeed 120 meters per second, angle of attack zero degrees, freestream pressure 900 millibars and temperature 33 degrees Celsius. Contours represent every 3.33 meters per second difference in velocity.

The initial procedure sought to increase the efficiency of this OpenFOAM processing workflow through the bypass of the *snappyHexMesh* meshing routine for all six iterations, reusing the mesh created within the initial solution and changing the boundary conditions for each iteration. Ultimately, this procedure failed to produce the desired outcome allowing for the analysis of solutions initiated with various boundary conditions. Within the *snappyHexMesh* routine, for each patch meshed within the domain, the boundary conditions information is stored within the mesh. Therefore, the method of reusing the initial solution

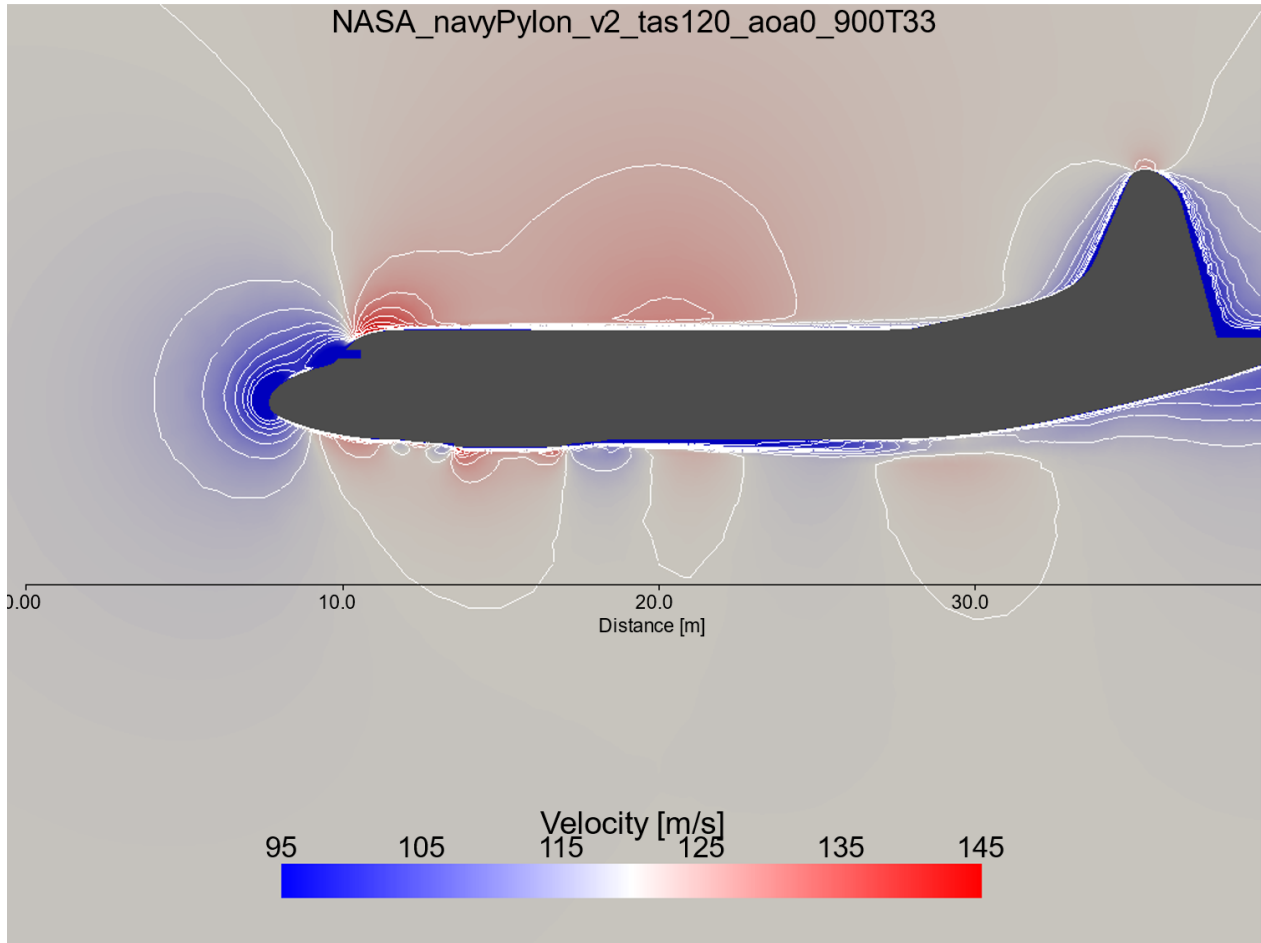


Figure 15: NASA P-3 Orion Navy Pylon configuration showcasing velocity magnitudes with a two-dimensional slice through the center line of the fuselage. For this simulation, boundary conditions are: freestream airspeed 120 meters per second, angle of attack zero degrees, freestream pressure 900 millibars and temperature 33 degrees Celsius. Contours represent every 3.33 meters per second difference in velocity.

resolved mesh for each iteration of the Navy Pylon configuration simulations ultimately reproduced the results of the initial iteration. A third version of these simulations was produced that recreated the mesh for each simulation and allows for changing of boundary conditions outlined in Table 2.

With PyVista, Navy Pylon configuration solutions were rendered for the full NASA P-3 with associated scalar fields for all six iterations. Two-dimensional slices highlighting the Navy Pylon, with associated Cloud Droplet Probe and `Bullet` Canister, are shown in two

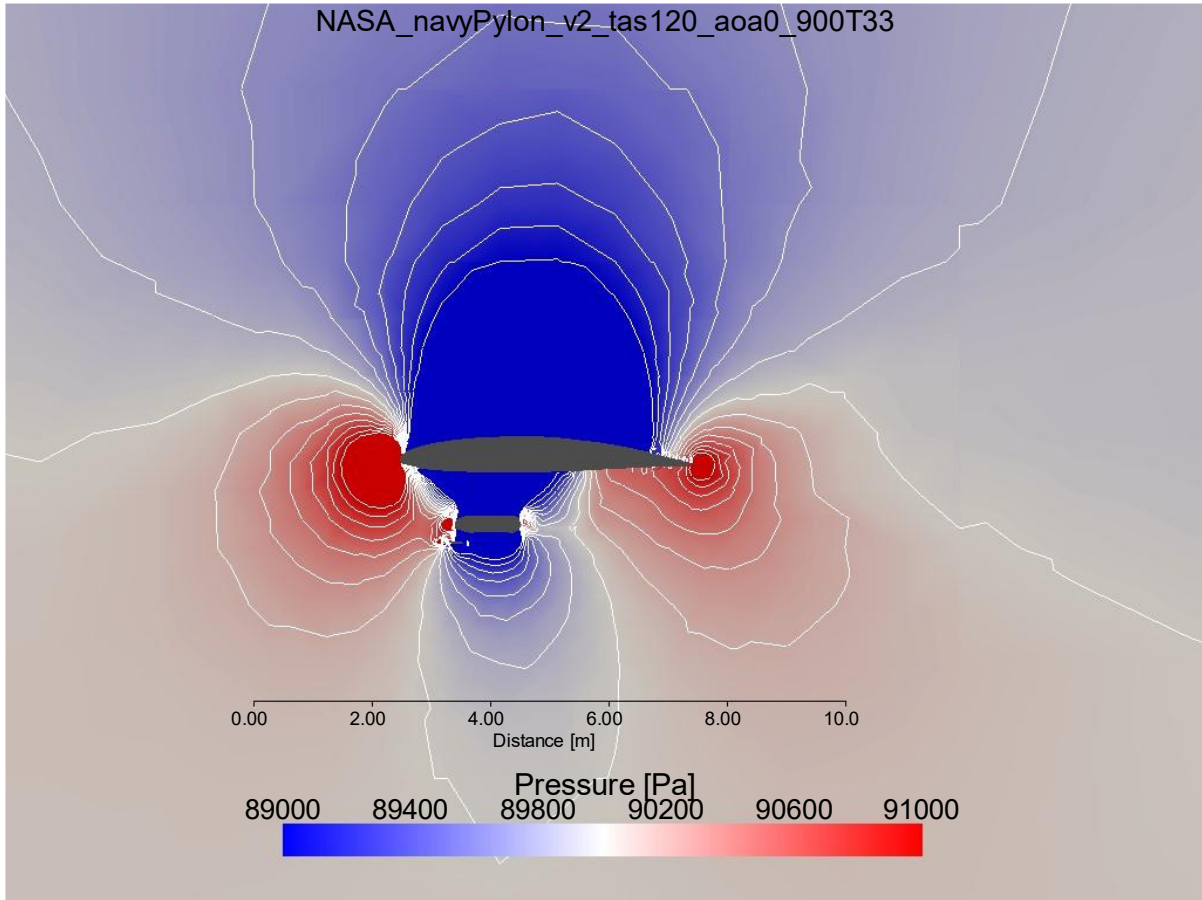


Figure 16: NASA P-3 Orion Navy Pylon configuration showcasing atmospheric pressure with a two-dimensional slice through the center line of the Cloud Droplet Probe. For this simulation, boundary conditions are: freestream airspeed 120 meters per second, angle of attack zero degrees, freestream pressure 900 millibars and temperature 33 degrees Celsius. Contours represent every 133.3 Pa difference in pressures.

different viewing orientations within Figs. 13 and 14 of the Cloud Droplet Probe sample volume and highlighting a side profile of the assembly, with the fuselage in the direction into the page. The magnitude of the velocity scalar is shown and contoured in Fig. 13, with decrease in velocities from the freestream value (120 ms^{-1}) two meters ahead of the leading edge of the aircraft wing and four meters behind the pylon assembly. Associated with the decrease in velocities ahead of the leading edge of the aircraft is the increase in velocities around the wing, resulting in velocities greater than freestream conditions ($\sim 6 \text{ ms}^{-1}$) 6 meters above and below the pylon assembly. As shown in Fig. 14, with a viewing orientation across the pylon assembly

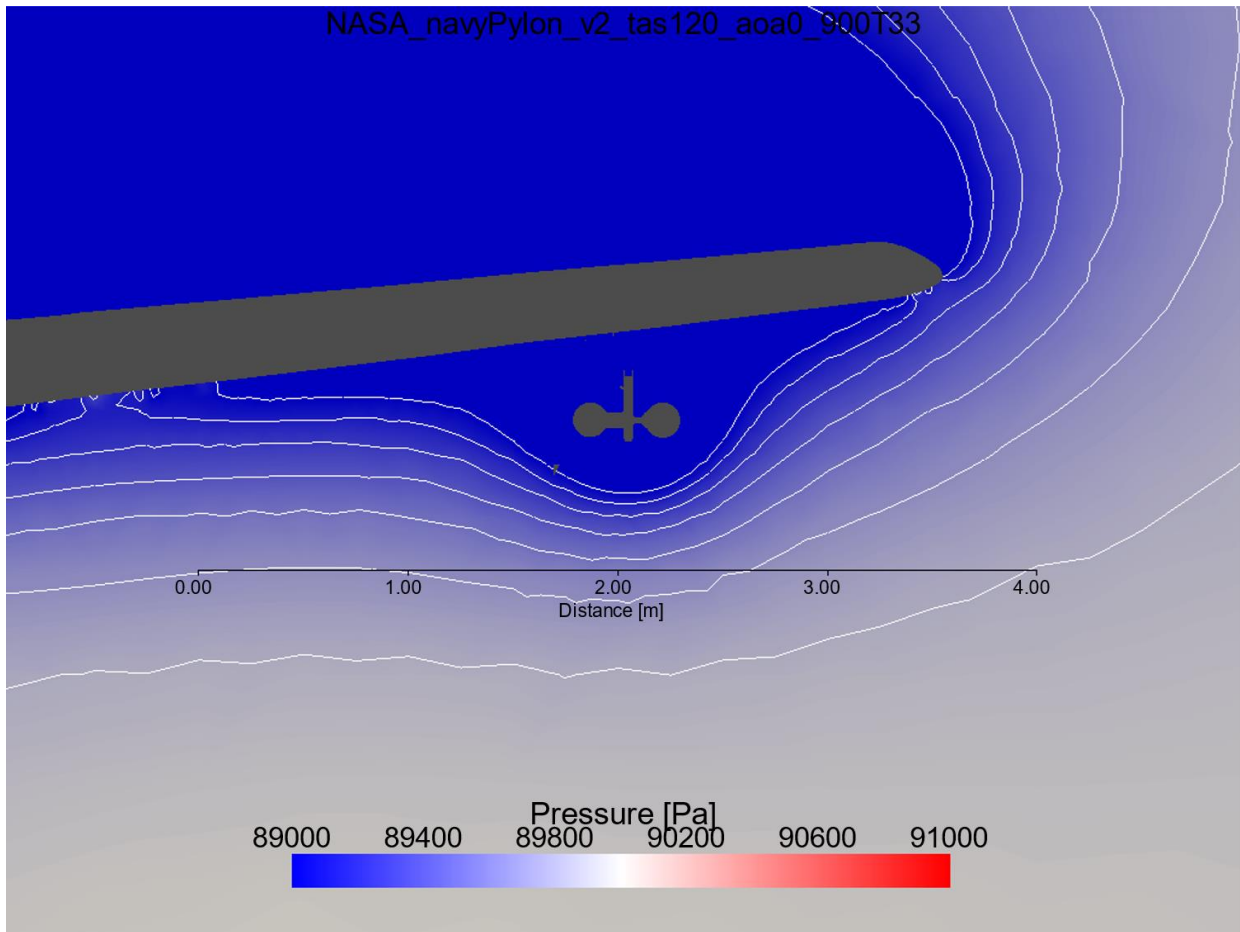


Figure 17: NASA P-3 Orion Navy Pylon configuration showcasing atmospheric pressure with a two-dimensional slice across the leading edge of the aircraft wing. For this simulation, boundary conditions are: freestream airspeed 120 meters per second, angle of attack zero degrees, freestream pressure 900 millibars and temperature 33 degrees Celsius. Contours represent every 133.3 Pa difference in pressures.

and the two-dimensional slice centered on the leading edge of the aircraft, the decrease in velocities ahead of the pylon configuration are constrained to the leading edge of the aircraft. Velocity contours indicate near freestream velocities close to the pylon assembly, with an increase in velocities outboard as shown by contours two meters from the assembly. Fig.13 also highlights this with undisturbed airflow directly underneath the Cloud Droplet Probe. Fig. 15 includes a viewing angle along the centerline of the NASA P-3 Orion, away from either pylon configuration to allow for comparison along a similar mesh for the various simulations.

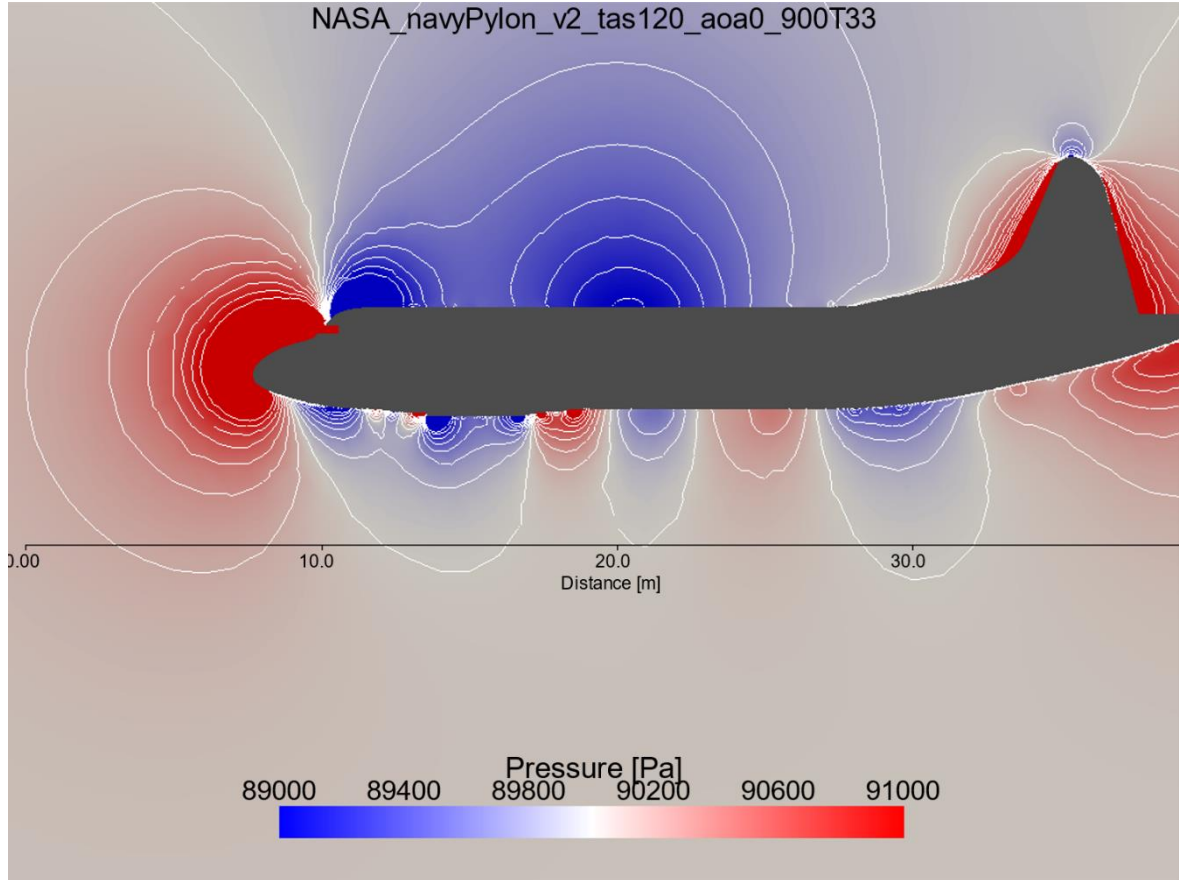


Figure 18: NASA P-3 Orion Navy Pylon configuration showcasing atmospheric pressure with a two-dimensional slice through the centerline of the fuselage. For this simulation, boundary conditions are: freestream airspeed 120 meters per second, angle of attack zero degrees, freestream pressure 900 millibars and temperature 33 degrees Celsius. Contours represent every 133.3 Pa difference in pressures.

Associated with the decrease in velocities from freestream values ahead of the leading edge of the aircraft wing is the increased atmospheric pressure (Fig. 16). This pressure, known as Ram pressure, is the result of the bulk motion of the fluid against the pylon assembly. As expected for subsonic aerodynamic flow, deviations from freestream values are found ahead and being the aircraft body, with the ram pressure increasing from the 90000 Pascal boundary conditions applied to the simulation. This increase in ram pressure is also observed ahead of

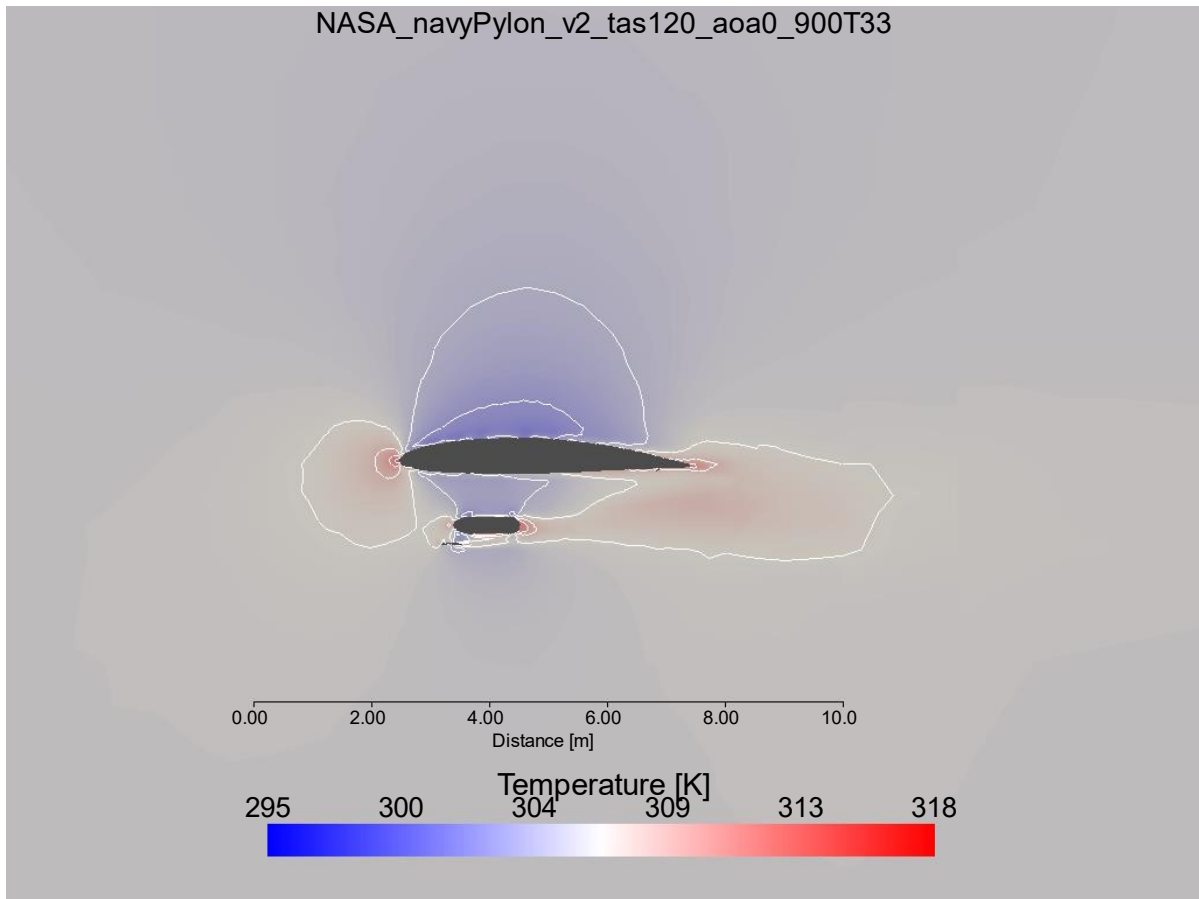


Figure 19: NASA P-3 Orion Navy Pylon configuration showcasing total temperature with a two-dimensional slice through the center of the Cloud Droplet Probe. For this simulation, boundary conditions are: freestream airspeed 120 meters per second, angle of attack zero degrees, freestream pressure 900 millibars and temperature 33 degrees Celsius. Contours represent every 1.5 Kelvin difference in temperature.

the Cloud Droplet Probe Bullet canister, though limited to directly ahead of the instrument. As expected with airflow over an airfoil, pressure above the wing is markedly lower than

freestream values. In contrast to the velocities within Fig. 13, the pressure contours, representing 133.3 pascal differences within the flow, indicate lower pressure propagates well above and ahead of the leading edge of the aircraft. From the viewing angle across the pylon assembly, Fig. 17 indicates lower pressure inboard (or toward the center of the aircraft) and outboard associated with the increased velocities shown in Fig. 14. These areas of lower pressure extend outboard beyond the wing tip and two meters below the pylon assembly. Fig.

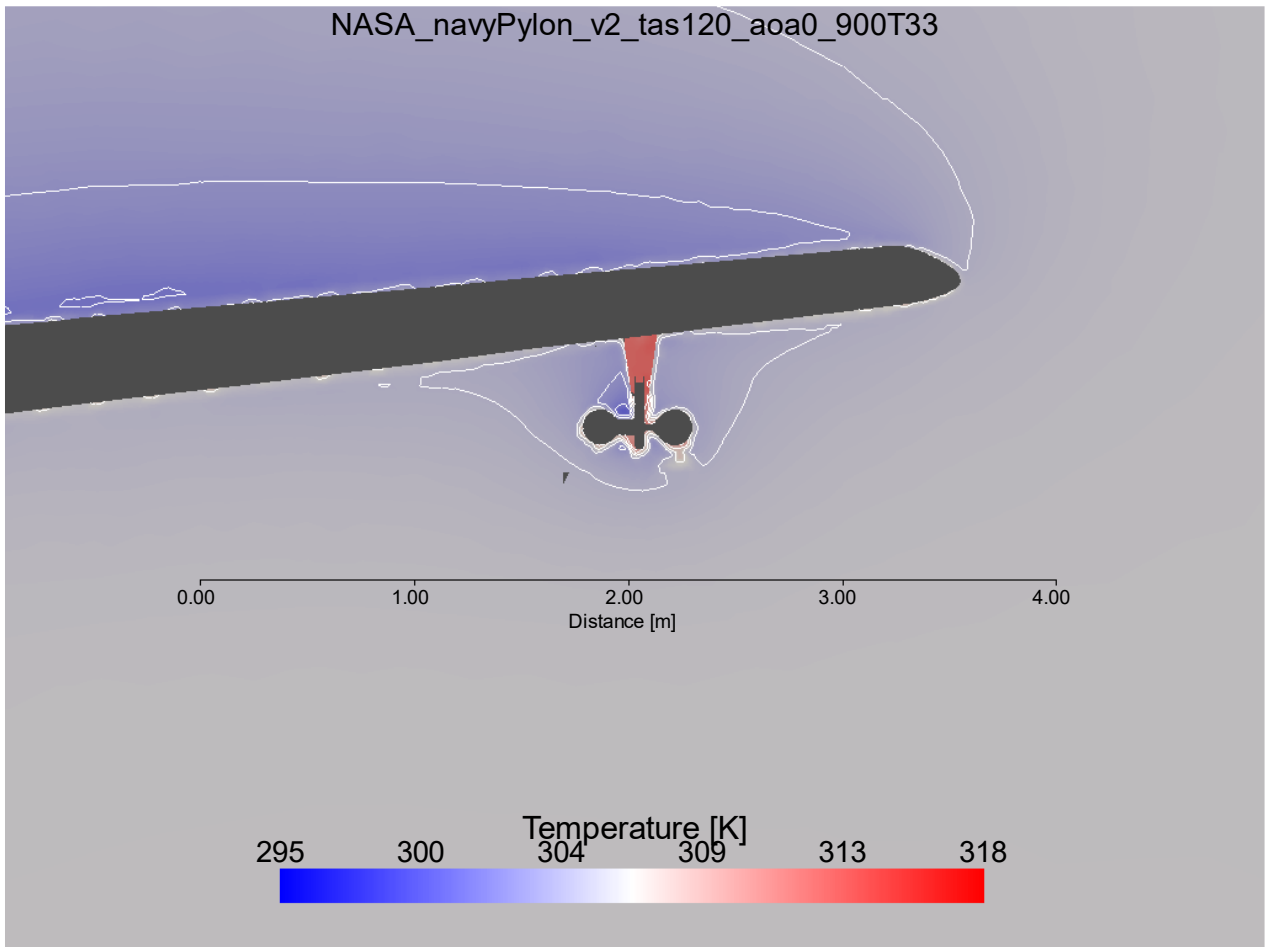


Figure 20: NASA P-3 Orion Navy Pylon configuration showcasing total temperature with a two-dimensional slice along the leading edge of the aircraft wing. For this simulation, boundary conditions are: freestream airspeed 120 meters per second, angle of attack zero degrees, freestream pressure 900 millibars and temperature 33 degrees Celsius. Contours represent every 1.5 Kelvin difference in temperature.

18 contains the pressure field along the NASA P-3 fuselage, with a marked area of increased ram pressure within ten meters of the aircraft nose. Beneath the aircraft fuselage, areas of increased ram pressure ahead of the NASA P-3 bomb bay, which housed the Jet Propulsion Laboratory's Airborne Precipitation Radar Version 3, result in oscillating areas of high and low pressure down the aircraft fuselage.

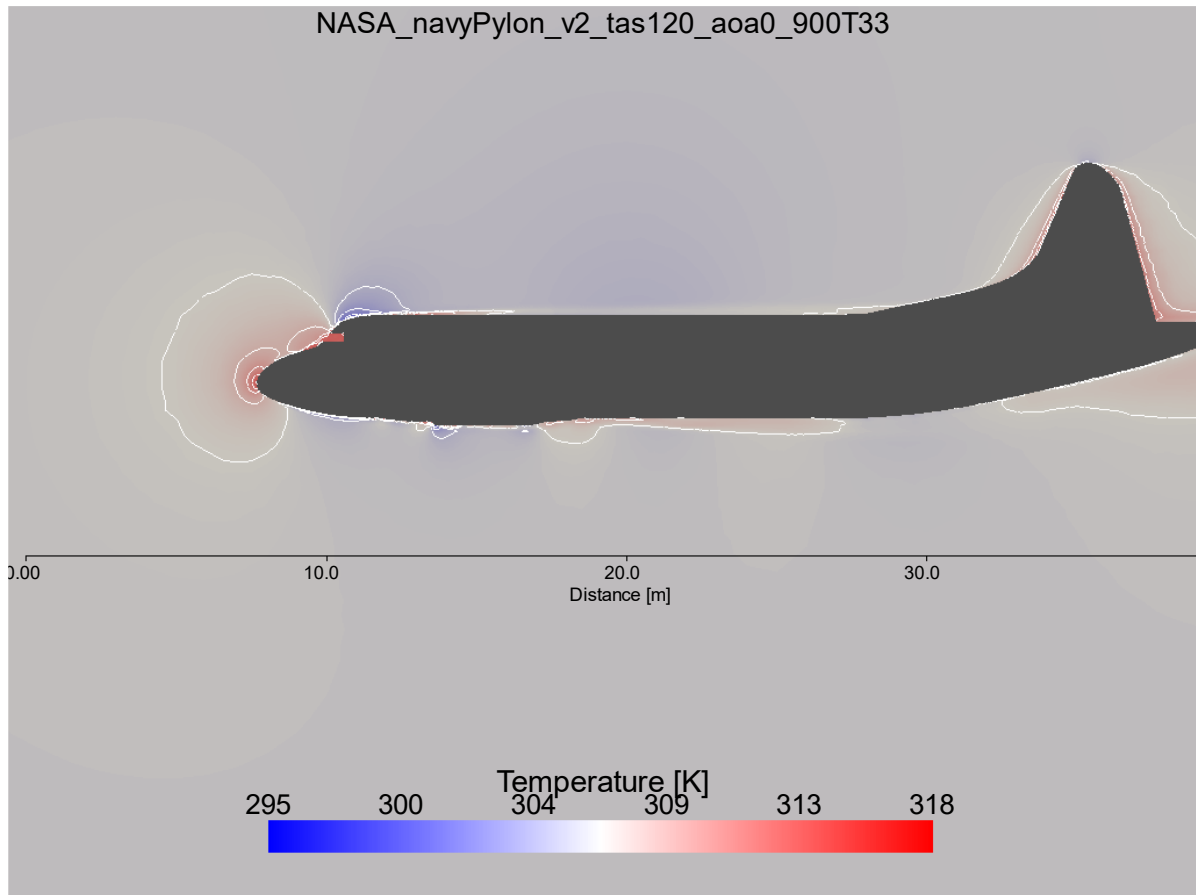


Figure 21: NASA P-3 Orion Navy Pylon configuration showcasing total temperature with a two-dimensional slice along centerline of the aircraft fuselage. For this simulation, boundary conditions are: freestream airspeed 120 meters per second, angle of attack zero degrees, freestream pressure 900 millibars and temperature 33 degrees Celsius. Contours represent every 1.5 Kelvin difference in temperature.

Along with the pressure and airflow velocity, the temperature at the pylon assembly is also critical for the in-situ microphysical instrumentation, particularly instrumentation utilizing heated wires (Hotwire). The temperature of the fluid field from the viewing angle along the pylon assembly is provided in Fig. 19. As expected, as the fluid flow is slowed ahead of the leading edge due to the increase in ram pressure, the fluid is compressed and experiences an increase in temperature due to the conversion of kinetic energy into internal energy. This fluid flow temperature ahead of the aircraft body is the stagnation temperature, or total air temperature. Figure 19 indicates the total air temperature is contained directly ahead of the

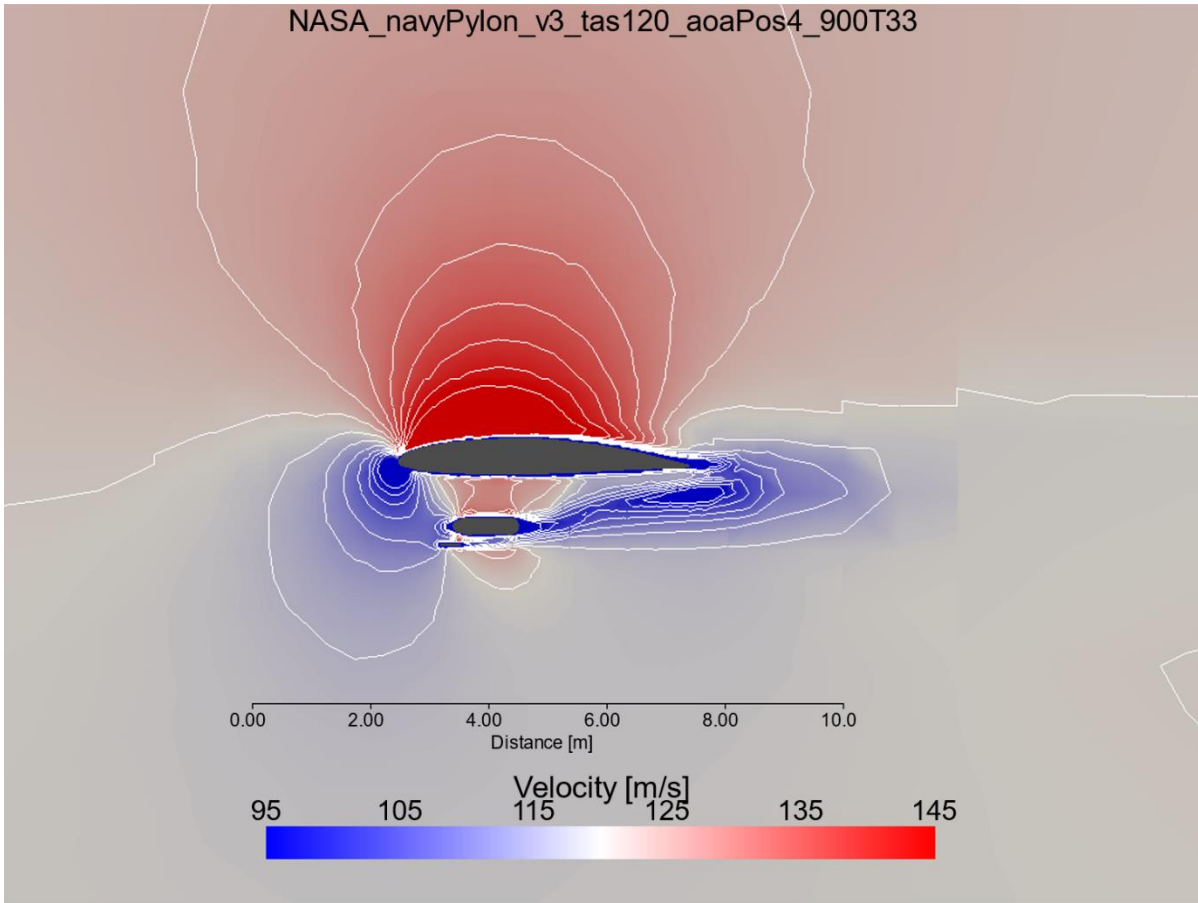


Figure 22: NASA P-3 Orion Navy Pylon configuration showcasing velocity magnitudes with a two-dimensional slice through the solution with a view point along the wing (into the page is towards the fuselage). For this simulation, boundary conditions are: freestream airspeed 120 meters per second, angle of attack positive four degrees , freestream pressure 900 millibars and temperature 33 degrees Celsius. Contours represent every 3.33 meters per second difference in velocity.

leading edge of the wing and CDP canister, with much of the temperature increase confined to behind the assembly as the fluid flow converges to maintain continuity. Unlike the velocities shown in Fig. 13 or ram pressure shown in Fig. 16, temperature contours indicate disjointed effects, with little to no influence of the aircraft wing on the total temperature increase at the canister location. From the viewing angle across the pylon, the temperature increase is confined

to the near the surface skin of the pylon assembly, with the CDP far enough below the Bullet canister to be near ambient conditions (Fig. 20).

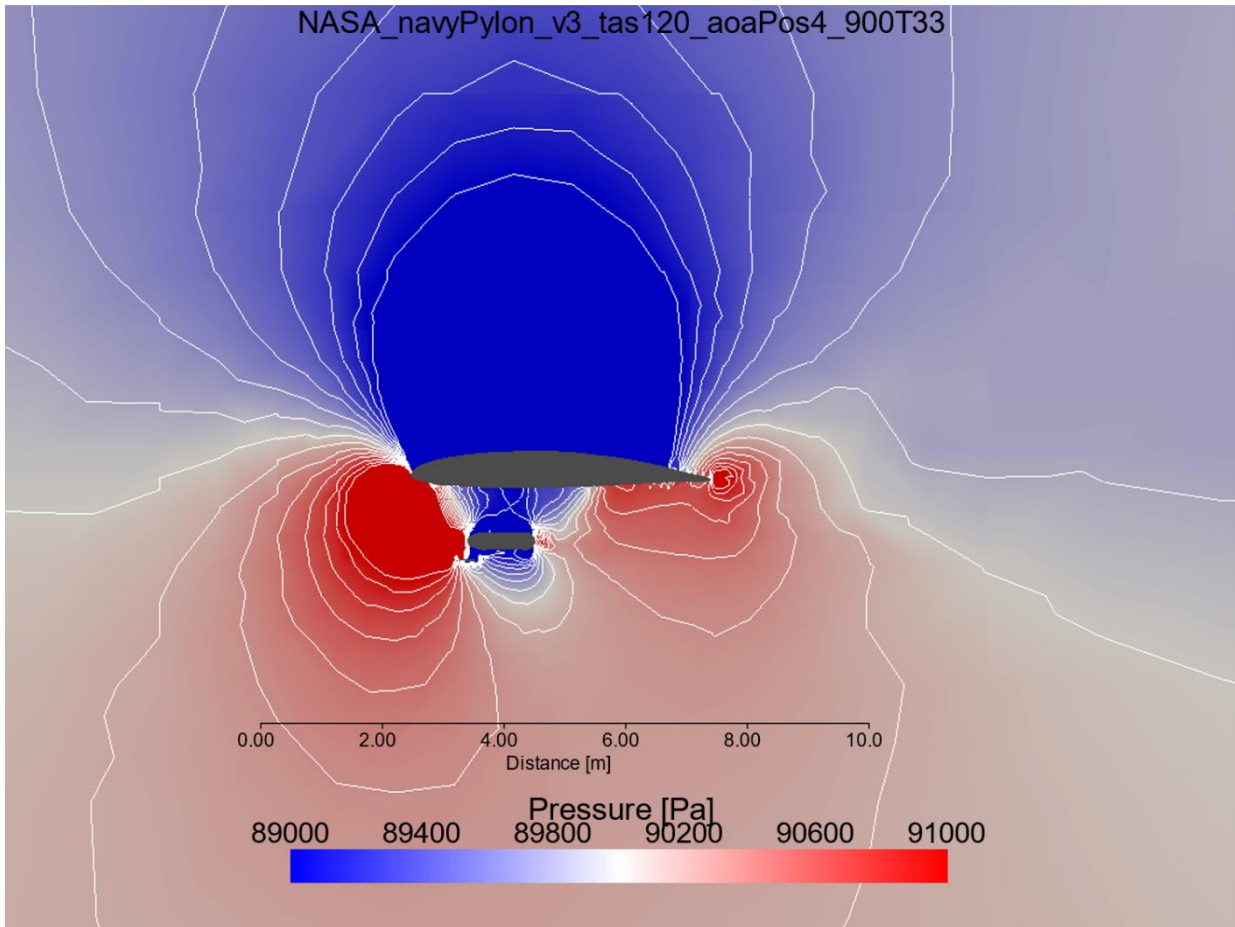


Figure 23: NASA P-3 Orion Navy Pylon configuration showcasing atmospheric pressure with a two-dimensional slice through the center line of the Cloud Droplet Probe. For this simulation, boundary conditions are: freestream airspeed 120 meters per second, angle of attack positive four degrees, freestream pressure 900 millibars and temperature 33 degrees Celsius. Contours represent every 133.3 Pa difference in pressures.

As described in previous chapters (see Chapter 1b), the NASA P-3 maneuvered using vertical profiles to sample the depth of the Southern Atlantic Ocean marine stratocumulus layers. For an aircraft in a climb, the direction of ambient air flow is unchanged, while the angle (i.e. angle of attack) between the centerline through the airfoil (i.e. chord line) and the flow direction increases. Within the OpenFOAM framework, to simulate these maneuvers on the airflow around the pylon assemblies, a vertical velocity component is added to the domain's

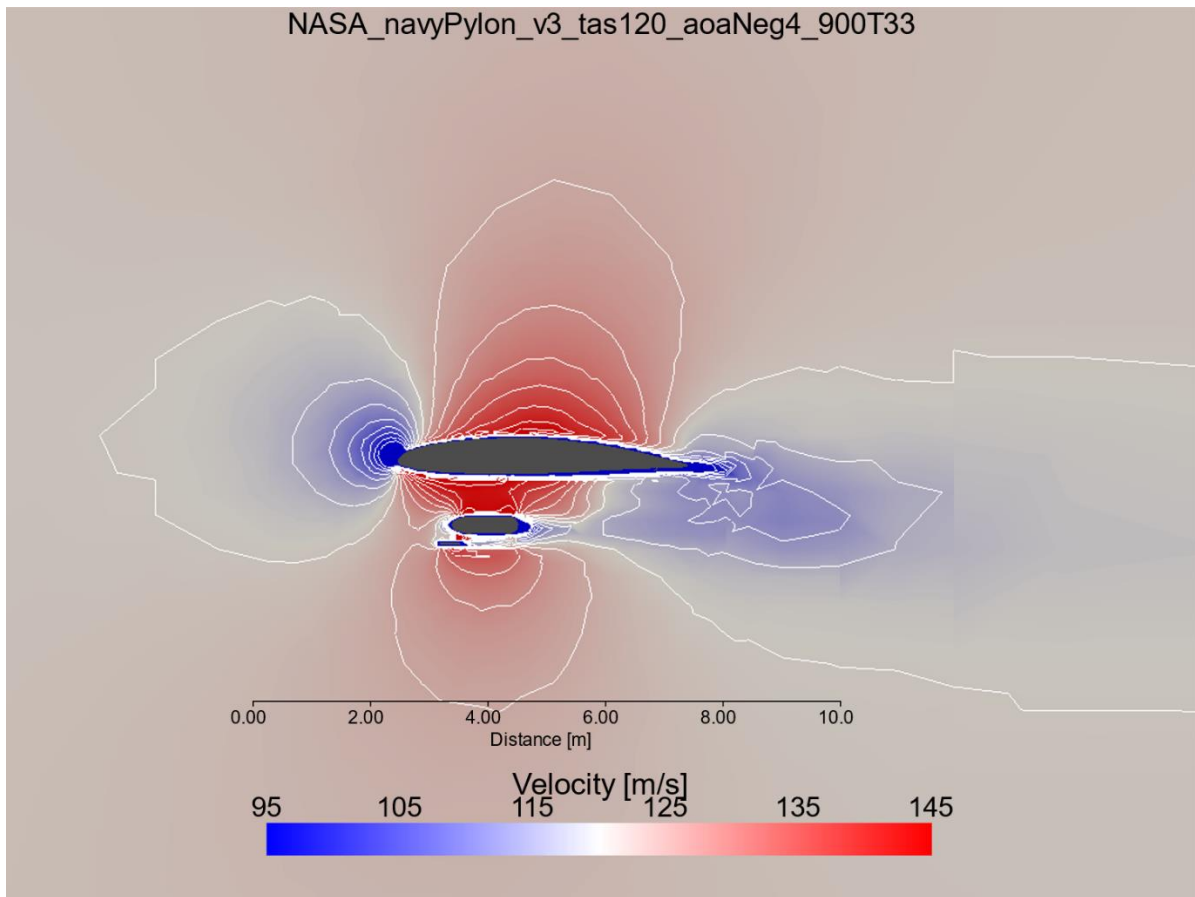


Figure 24: NASA P-3 Orion Navy Pylon configuration showcasing velocity magnitudes with a two-dimensional slice through the solution with a view point along the wing (into the page is towards the fuselage). For this simulation, boundary conditions are: freestream airspeed 120 meters per second, angle of attack negative four degrees, freestream pressure 900 millibars and temperature 33 degrees Celsius. Contours represent every 3.33 meters per second difference in velocity.

inlet boundary condition. Therefore, within the OpenFOAM simulations, rather than manipulating the chord line, the angle of the ambient fluid flow is altered. This methodology was chosen for computational efficiency rather than the translation of each centroid, face, and vertices of the NASA P-3 Orion STL file to account for an angle of attack. In order to constrain the full effect of these maneuvers on the airflow, the maximum and minimum angle of attacks ($\pm 4^\circ$) flow components were added to the inlet boundary conditions. For the cases with an inlet boundary condition of 120 ms^{-1} (140 ms^{-1}), this resulted in a vertical velocity of component of 8.39 ms^{-1} (9.77 ms^{-1}).

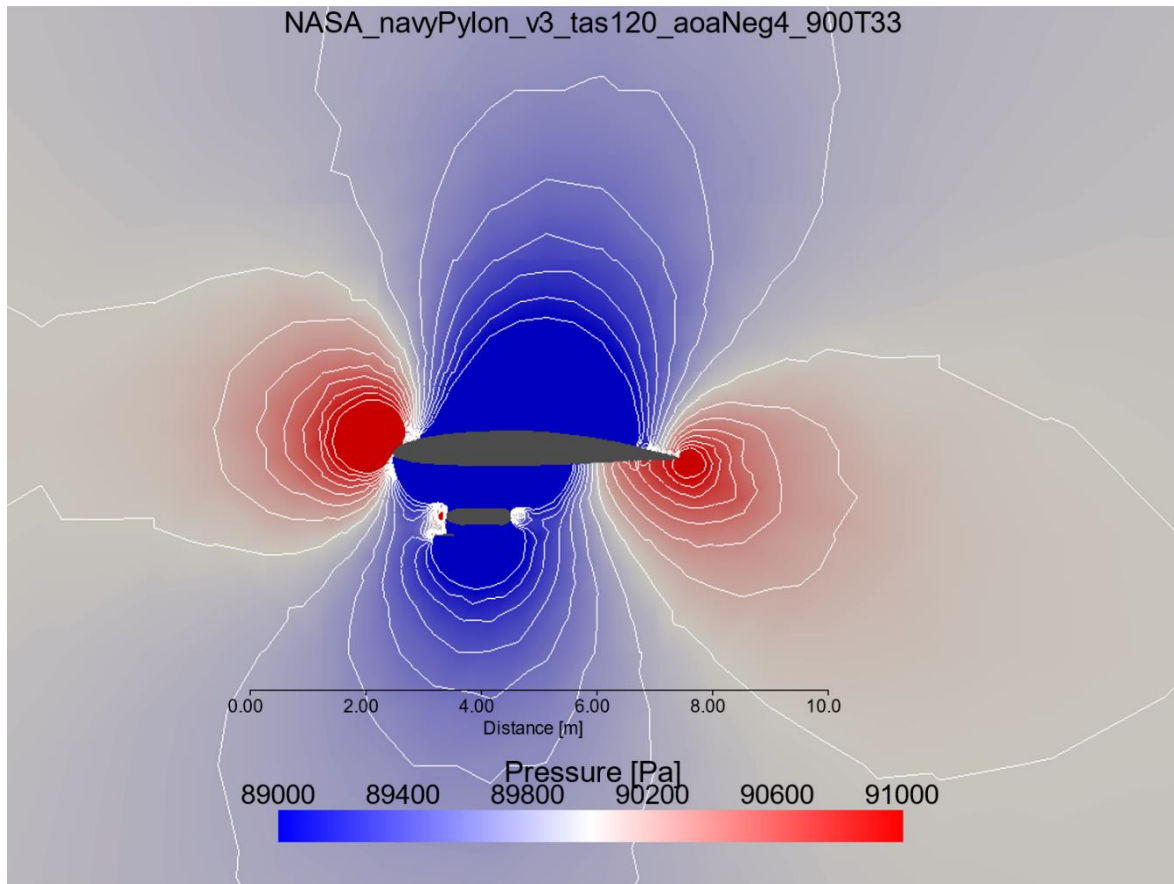


Figure 25: NASA P-3 Orion Navy Pylon configuration showcasing atmospheric pressure with a two-dimensional slice through the center line of the Cloud Droplet Probe. For this simulation, boundary conditions are: freestream airspeed 120 meters per second, angle of attack negative four degrees, freestream pressure 900 millibars and temperature 33 degrees Celsius. Contours represent every 133.3 Pa difference in pressures.

For the $+4^\circ$ angle of attack simulation, as shown in Fig. 22, the fluid flow is no longer centered around the middle of the aircraft wing leading edge, but is shifted vertically compared to the level flight simulation ($\alpha = 0^\circ$) shown in Fig. 13. This shift down along the leading edge of the aircraft wing is the expected result for an aircraft in a climb and highlights the ability of this methodology to represent vertical maneuvers of the aircraft. In addition, the $+4^\circ$ angle of attack case shows a decrease of airflow ahead of the CDP compared to the level in-cloud flight simulation in Fig. 13. The pressure field with a viewing angle along the pylon assembly for the $+4^\circ$ angle of attack case is provided in Fig. 23. In contrast to level in-cloud flight simulation shown in Fig. 15, the increased ram pressure from the aircraft wing now extends well below

the pylon assembly and combines with the ram pressure of the CDP Bullet canister. The area of low pressure observed directly beneath the canister within Fig. 15 has decreased to within a meter of the canister assembly. Overall, for the $+4^\circ$ angle of attack case, there is no longer an area of undisturbed airflow near the CDP.

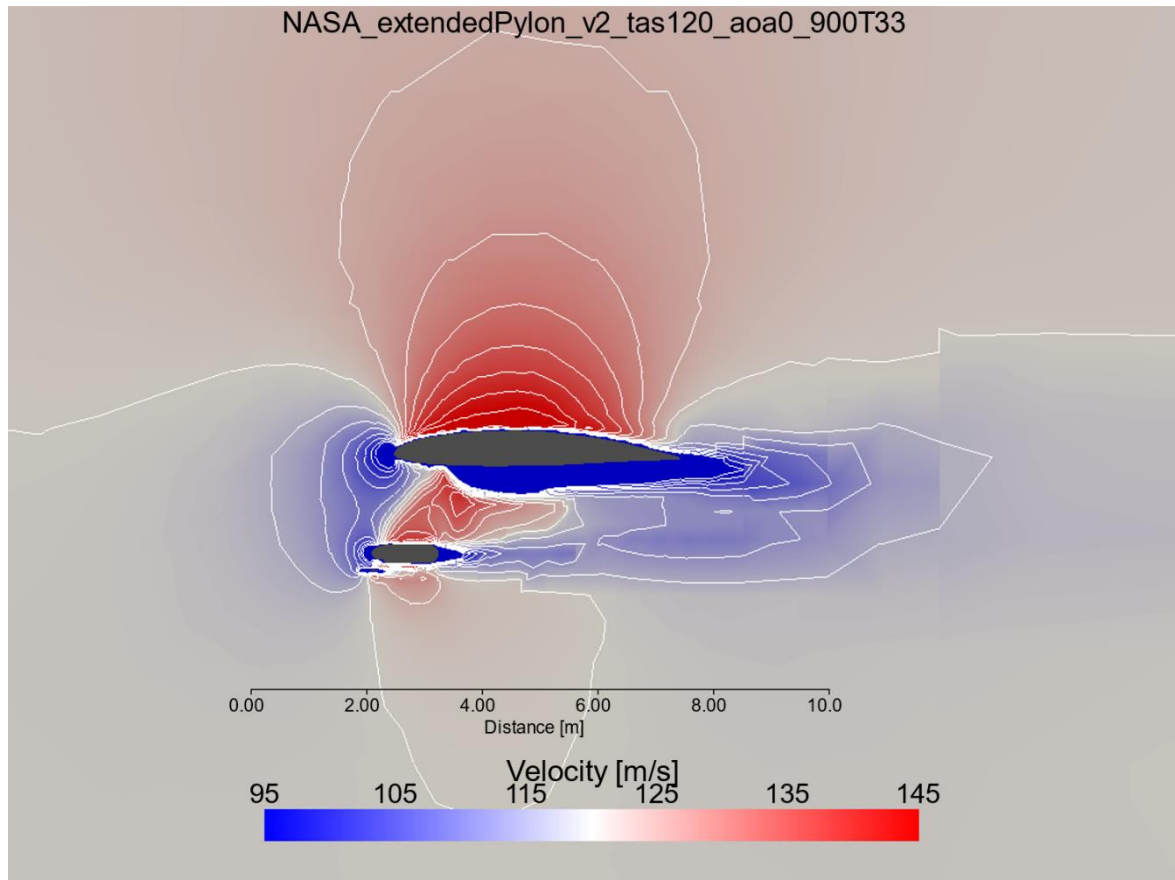


Figure 26: NASA P-3 Orion Extended Pylon configuration showcasing velocity magnitudes with a two-dimensional slice through the solution with a view point along the wing (into the page is towards the fuselage). For this simulation, boundary conditions are: freestream airspeed 120 meters per second, angle of attack zero degrees, freestream pressure 900 millibars and temperature 33 degrees Celsius. Contours represent every 3.33 meters per second difference in velocity.

To simulate the descent portion of the sawtooth profiles, a -4° angle of attack was applied to the OpenFOAM cases and the velocity field is shown in Fig. 24. As expected for a decent, the -4° angle of attack case replicates the expected shift of the flow angle up on the leading edge of the aircraft. This shift in the relative flow angle results in a stark contrast from the level

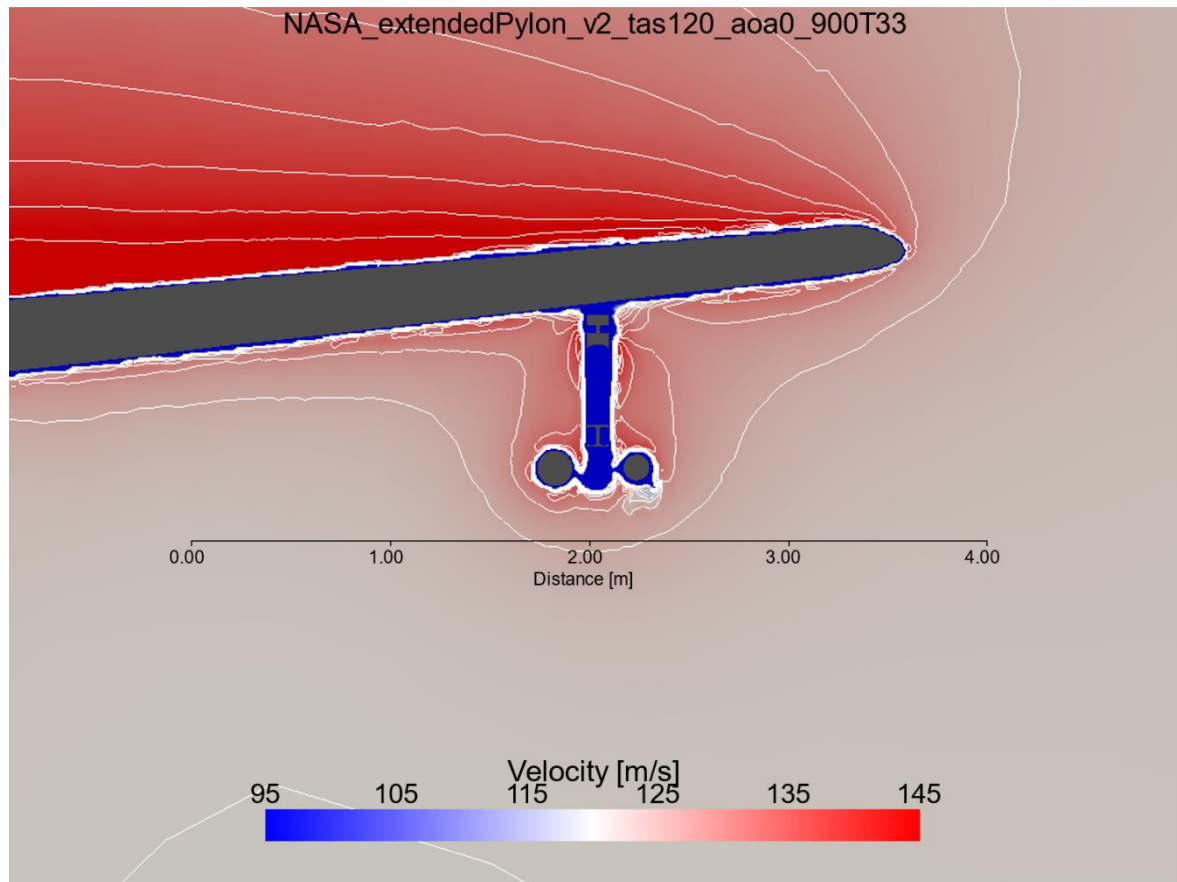


Figure 27: NASA P-3 Orion Extended Pylon configuration showcasing total temperature with a two-dimensional slice along the leading edge of the aircraft wing. For this simulation, boundary conditions are: freestream airspeed 120 meters per second, angle of attack zero degrees, freestream pressure 900 millibars and temperature 33 degrees Celsius. Contours represent every 3.33 meters per second difference in velocity.

in cloud flight simulation (Fig. 13) and ascent portion of the sawtooth profile (Fig. 22), where the deceleration of the fluid flow is now confined to the region ahead of the aircraft wing. At the CDP location, as shown by the velocity contours, airflow is within 3.3 ms^{-1} of freestream velocities, with increased velocities from freestream now extending from the pylon mount ahead of the Cloud Droplet Probe location. This increase in velocity is associated with a decrease in ram pressure compared to freestream values across much of the pylon assembly as shown in Fig. 25, where the leading edge of the aircraft wing experiences the most significant increase in ram pressure. This increase in velocity results in a shielding effect of the pylon

assembly, with only the instrument canister and CDP instrument head experiencing increased ram pressure.

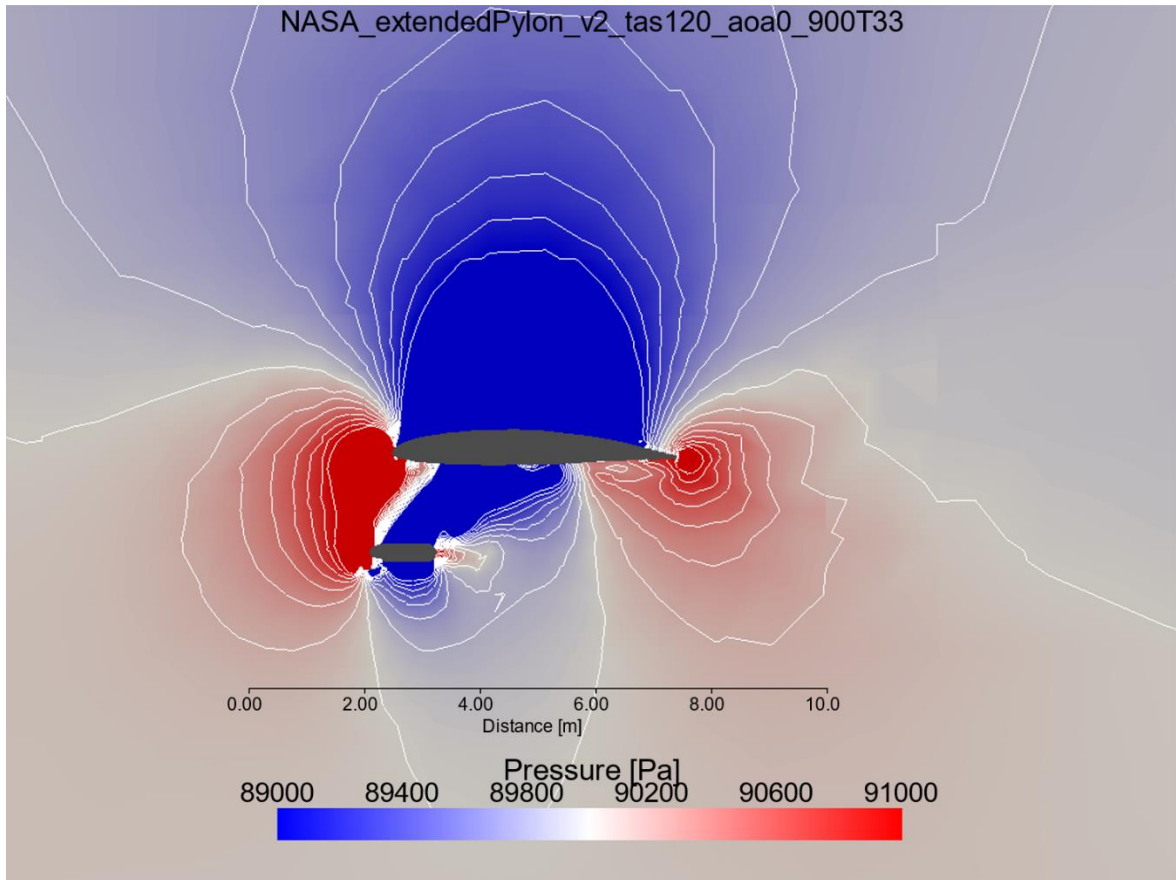


Figure 28: NASA P-3 Orion Extended Pylon configuration showcasing atmospheric pressure with a two-dimensional slice through the center line of the Cloud Droplet Probe. For this simulation, boundary conditions are: freestream airspeed 120 meters per second, angle of attack zero degrees, freestream pressure 900 millibars and temperature 33 degrees Celsius. Contours represent every 133.3 Pa difference in pressures.

EXTENDED PYLON SOLUTIONS

Six iterations of the NASA P-3 Orion with the Extended Pylon configuration are simulated in this study. Similar to the Navy pylon configuration, a third version of these simulations were created to reproduce the complex mesh for each individual simulation with the appropriate boundary conditions and are shown here. Figure 26 shows the airflow velocity around the NASA P-3 with Extended Pylon configuration with exact boundary conditions as Fig. 13.

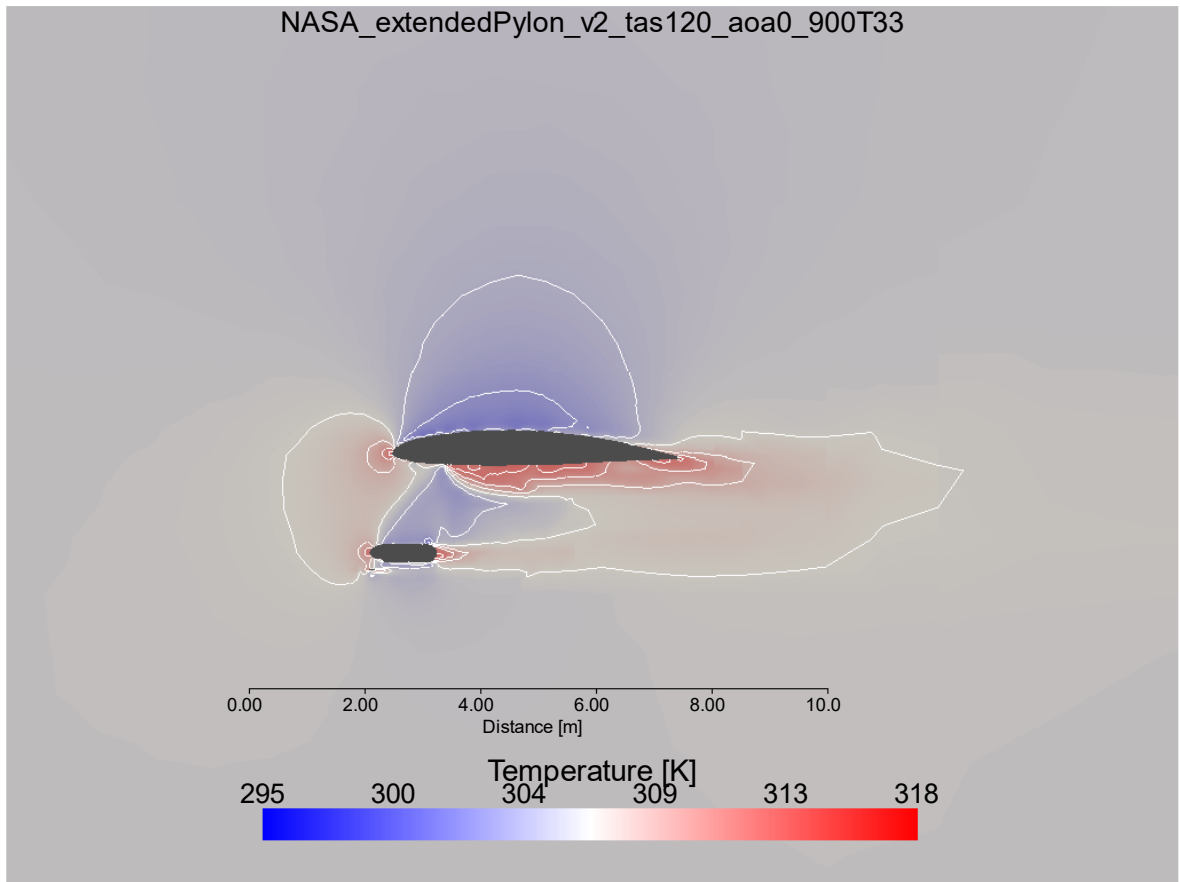


Figure 29: NASA P-3 Orion Extended Pylon configuration showcasing total temperature with a two-dimensional slice along centerline of the aircraft fuselage. For this simulation, boundary conditions are: freestream airspeed 120 meters per second, angle of attack zero degrees, freestream pressure 900 millibars and temperature 33 degrees Celsius. Contours represent every 1.5 Kelvin difference in temperature.

Similar to the actual NASA P-3 Orion configuration during ORACLES, the Extended Pylon configuration within these simulations is 0.3 meters lower and 0.57 meters ahead of the Navy Pylon configuration. The relocation of the instruments ahead of the leading edge of the aircraft wing results in the flow deceleration ahead of the stagnation zones of the instrument canisters and aircraft wing. In contrast to Fig. 13, these stagnation zones provide a compounding effect on the velocity field, resulting in a broader area of decreased velocities around and behind the pylon assemblies.

Velocity contours also highlight that the airflow ahead of the CDP experiences a larger decrease from freestream values (120 ms^{-1}) as compared to the Navy Pylon in Fig. 13. Also notable is the tight velocity gradient associated with the pylon itself within Fig. 26, highlighted by the packed contours from the mounting location on the wing to the instrument canister. Fig. 27 contains a two-dimensional vertical slice along the aircraft wing centered on the Cloud Droplet Probe sample volume for the Extended Pylon configuration. Comparison with Figure 15 highlights the larger width of the Extended Pylon compared to the Navy Pylon design, which provides greater surface area for flow distortion ahead of the assembly. This increased pylon width results in a broad area of increased pressure ahead of the Extended Pylon as shown

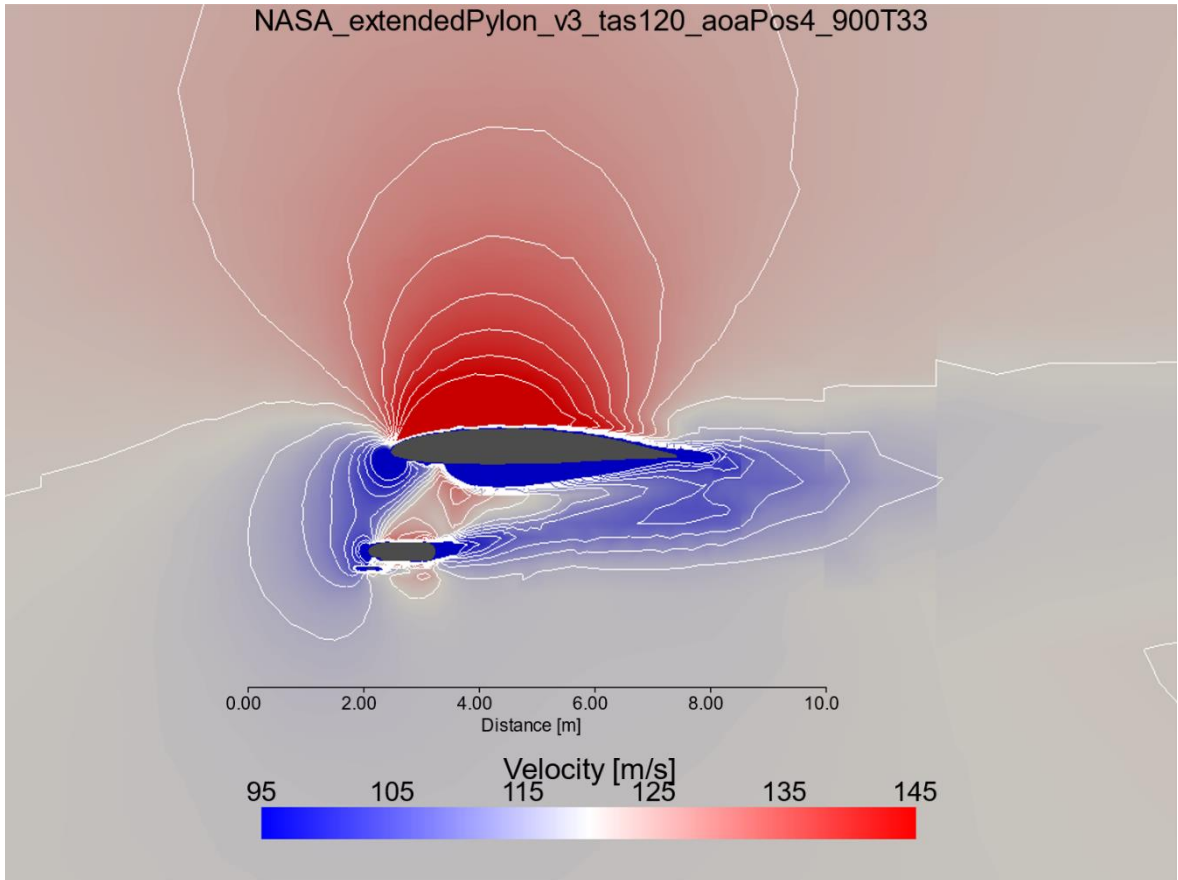


Figure 30: NASA P-3 Orion Extended Pylon configuration showcasing velocity magnitudes with a two-dimensional slice through the solution with a view point along the wing (into the page is towards the fuselage). For this simulation, boundary conditions are: freestream airspeed 120 meters per second, angle of attack positive four degrees, freestream pressure 900 millibars and temperature 33 degrees Celsius. Contours represent every 3.33 meters per second difference in velocity.

in Fig. 28, which extends from the wing leading edge to the Cloud Droplet Probe location. Interestingly, in comparison with Fig. 16, the overall lateral extent of the increased pressure ahead and behind of the pylon assemblies does not significantly change between simulations. However, the airflow directly ahead of the Cloud Droplet Probe on the Extended Pylon assembly contains a larger increase in ram pressure compared to the Navy Pylon. Figure 29 shows the two-dimensional slice along the Extended Pylon assembly of the temperature field. Similar to the velocity and pressure fields, the total temperature field does not experience a lateral increase in the distance ahead or behind of the Extended Pylon assembly affected but

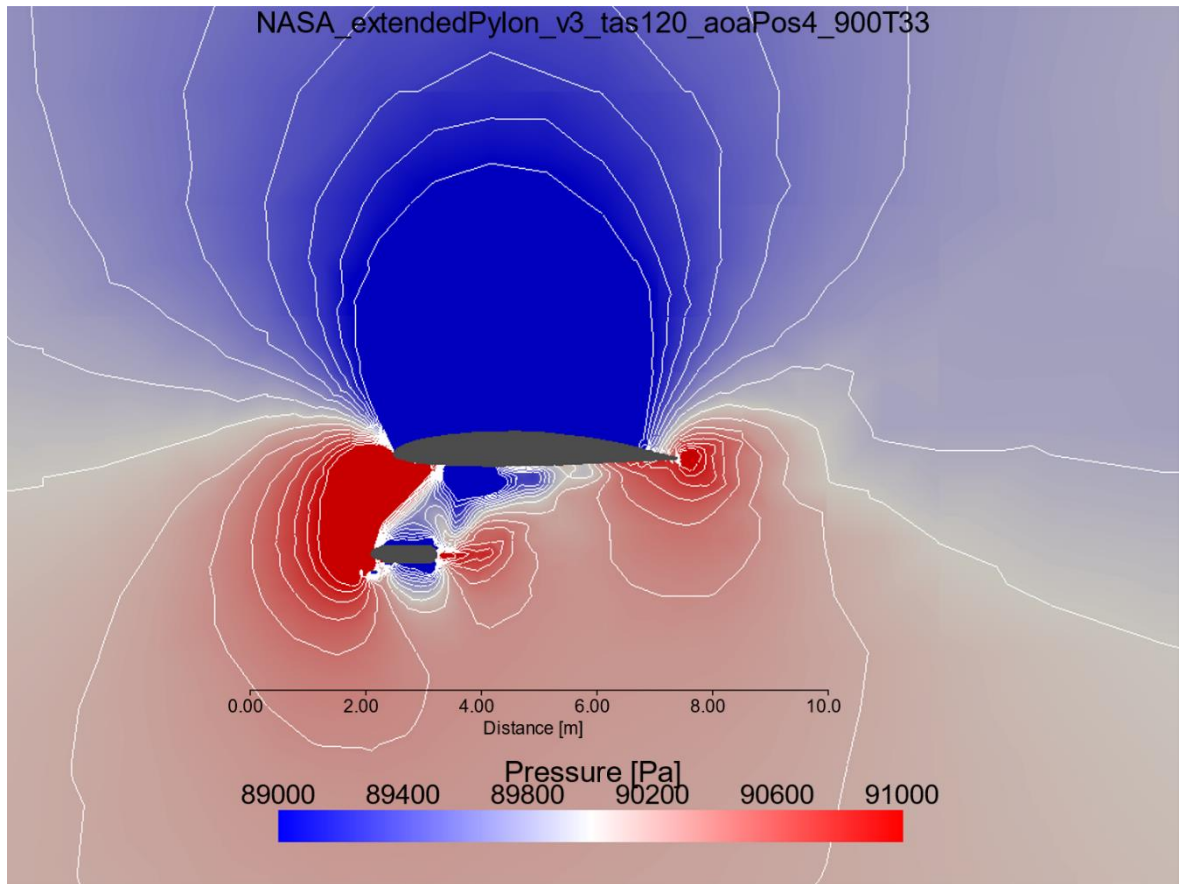


Figure 32: NASA P-3 Orion Extended Pylon configuration showcasing velocity magnitudes with a two-dimensional slice through the solution with a view point along the wing (into the page is towards the fuselage). For this simulation, boundary conditions are: freestream airspeed 120 meters per second, angle of attack negative four degrees, freestream pressure 900 millibars and temperature 33 degrees Celsius. Contours represent every 3.33 meters per second difference in velocity.

does contain an increase in magnitude at the Cloud Droplet Probe location compared to the Navy Pylon (Fig. 19). Additionally, while the total temperature increases are disjointed for the wing and Bullet canister within the Navy Pylon assembly (Fig. 19), the total temperature field is increased across the length of the Extended Pylon leading edge, resulting in a unified area of increased total temperature from the leading edge of the wing to CDP.

Similar to the NASA P-3 Navy pylon simulations, the ORACLES sawtooth profiles were simulated for the Extended Pylon configuration through modification of the velocity inlet boundary condition. Fig. 30 contains a two-dimensional slice along the pylon assembly of the

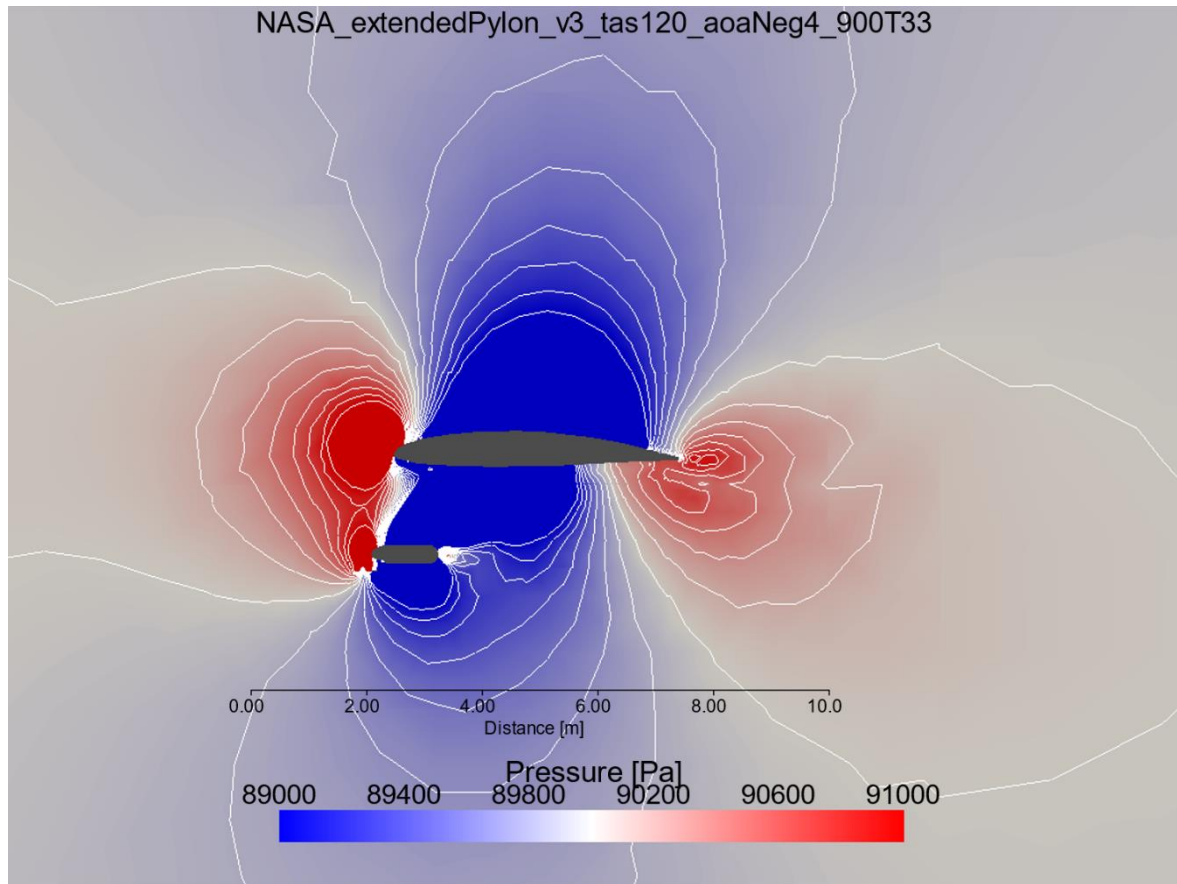


Figure 33: NASA P-3 Orion Extended Pylon configuration showcasing atmospheric pressure with a two-dimensional slice through the center line of the Cloud Droplet Probe. For this simulation, boundary conditions are: freestream airspeed 120 meters per second, angle of attack negative four degrees, freestream pressure 900 millibars and temperature 33 degrees Celsius. Contours represent every 133.3 Pa difference in pressures.

velocity field for the Extended Pylon ‘sawtooth climb’ (i.e. positive four degrees angle of attack) simulation. While the stagnation zone is shifted down along the leading edge of the wing and contains an increase in lateral extent, the overall velocity field is remarkably similar to the level legs shown in Fig. 26. Fig. 31 contains a similar viewing angle for the pressure field, which highlights increased ram pressure due to the pylon itself. This is shown with a component of increased ram pressure extending some distance behind the leading edge beneath the wing (and up the pylon) compared to the constant altitude flight legs (zero angle of attack simulation) of Fig. 28. However, as with the velocity field, the overall pressure field including the extent and magnitude of the increase in ram pressure ahead of the CDP is remarkably

similar to the constant altitude flight legs shown in Fig. 28. Figure 32 shows a two-dimensional slice along the pylon assembly of the velocity field for the Extended Pylon “sawtooth descent” (i.e. -4° angle of attack) and also contains a similar velocity field to the “sawtooth ascent” simulation of Fig. 30 and constant altitude legs of Fig. 26. Indicated by the velocity contours, Fig. 32 does contain a longer lateral extent of decreased airflow velocities ahead and behind of the pylon assembly compared to Fig. 26 and Fig. 30. Additionally, Fig. 32 contains an increased airflow velocities beneath and behind CDP instrumentation compared to Fig. 26. Figure 33 contains a similar slice of the pressure field for the “sawtooth descent” simulation.

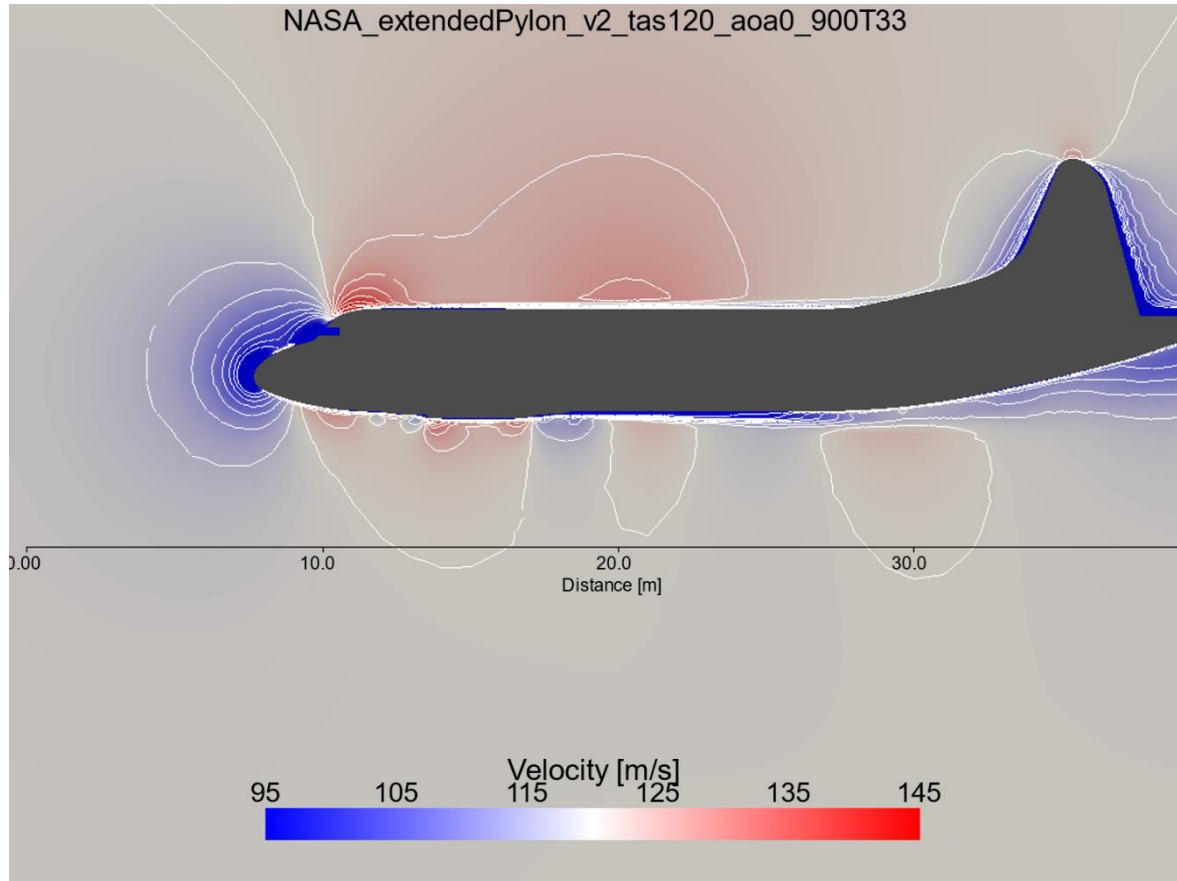


Figure 34: NASA P-3 Orion Extended Pylon configuration showcasing airflow velocity with a two-dimensional slice along centerline of the aircraft fuselage. For this simulation, boundary conditions are: freestream airspeed 120 meters per second, angle of attack zero degrees, freestream pressure 900 millibars and temperature 33 degrees Celsius. Contours represent every 3.33 meters per second.

With the change in the angle the airflow relative to the pylon assembly, the increase in ram pressure is shifted vertically from the CDP. In contrast to Fig. 28, the decrease in pressure (magnitude and extent) beneath and behind the pylon assembly is enhanced, coinciding with the increase in pressure above and in front.

While the differences between Navy Pylon and Extended Pylon simulations have been highlighted so far, to demonstrate both model iterations are comparable, comparison of simulations along the NASA P-3 fuselage highlight the repeatability of the simulations when resolving similar sections of the aircraft. Figure 34 contains a two-dimensional slice of the

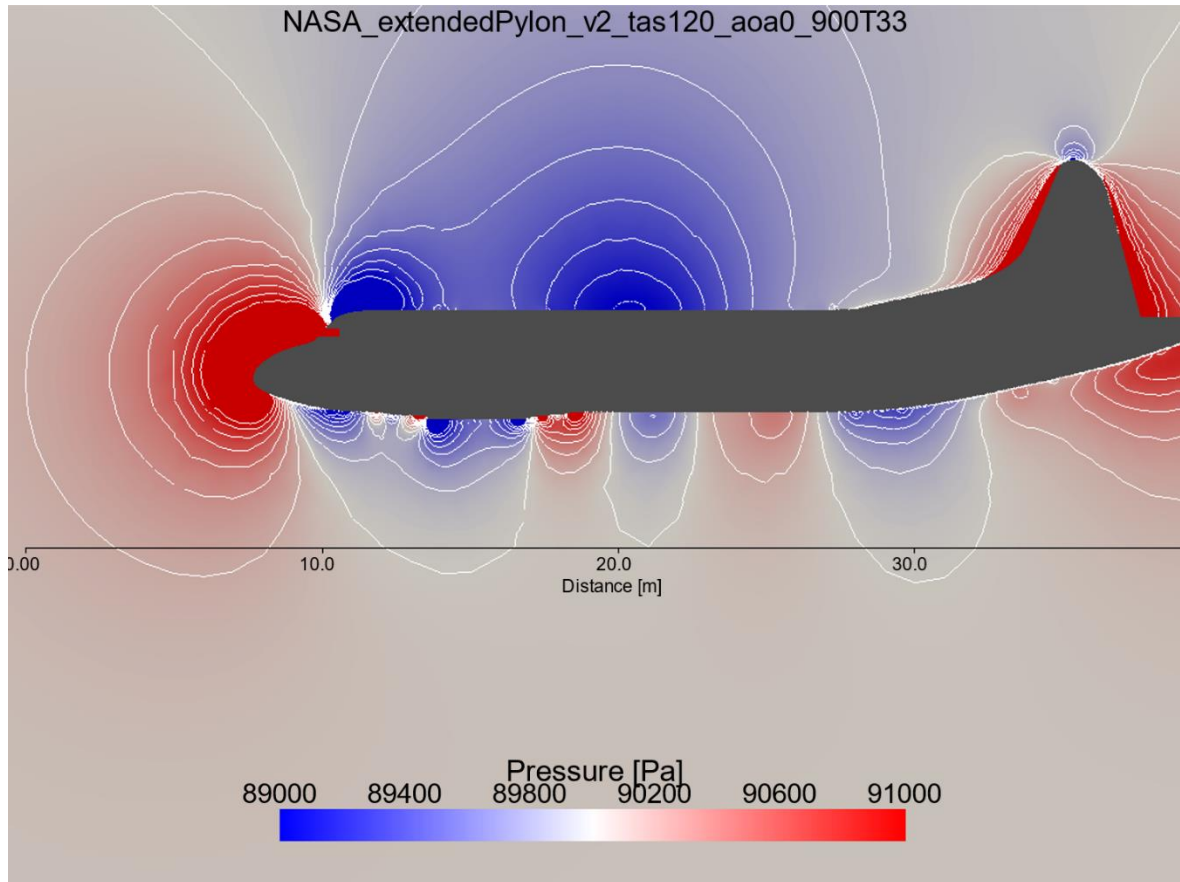


Figure 35: NASA P-3 Orion Extended Pylon configuration showcasing pressure field with a two-dimensional slice along centerline of the aircraft fuselage. For this simulation, boundary conditions are: freestream airspeed 120 meters per second, angle of attack zero degrees, freestream pressure 900 millibars and temperature 33 degrees Celsius. Contours represent every 133.3 Pa.

velocity field along the NASA P-3 aircraft from the Extended Pylon simulation (boundary conditions freestream airspeed 120 ms^{-1} and 0° angle of attack), while Fig. 35 contains a similar slice of the pressure field. Comparison of Fig. 15 to Fig. 34, and Fig. 18 to Fig. 35, highlight the robustness of these simulations, with comparable velocity fields for much of the aircraft. Small deviations do exist between the simulations along the fuselage boundary layer near the tail of the aircraft, which are likely due to small fluctuations within the *snappyHexMesh* routine and the increased resolution around the aircraft body.

CLOUD DROPLET PROBE SAMPLE VOLUME

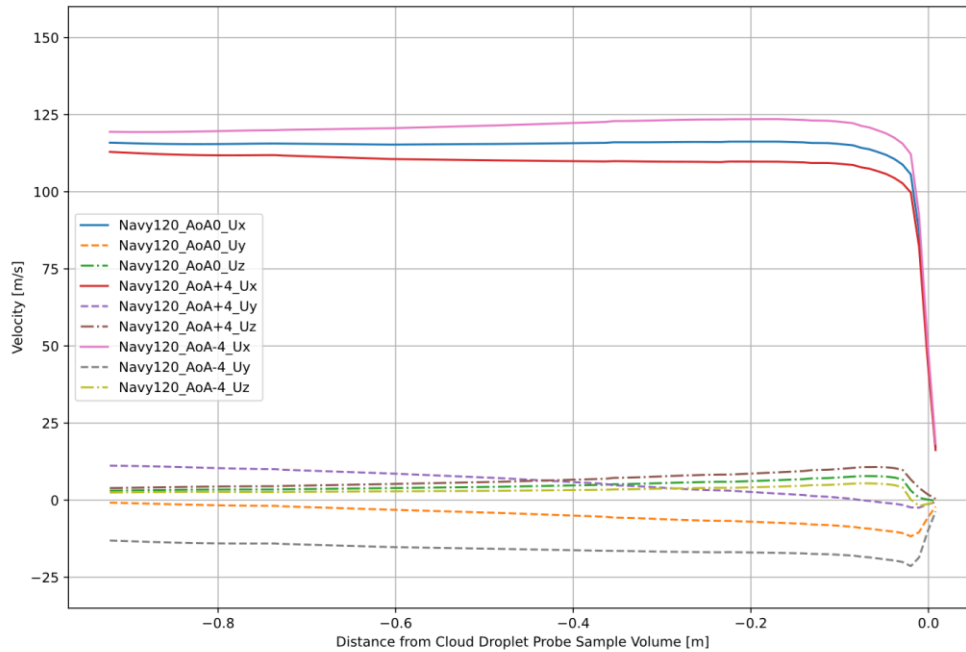


Figure 36: Subset of the velocity field through the mesh leading up to the Cloud Droplet Probe sample volume for the Navy Pylon solutions with the boundary conditions of 120 meters per second freestream and all simulated angle of attacks.

As defined in Table 2, additional simulations for each pylon configuration were performed in order to test the airflow response to changes in initial boundary conditions. For the sake of brevity, results for all simulations have been compiled through the subset of the scalar fields through the mesh leading up to the Cloud Droplet Probe sample volume per pylon configuration. For the Navy Pylon configuration, the Cloud Droplet Probe is located within the mesh at the location [14.49, 3.05, 13.75] and the subset of the scalar fields have been created for the area up to one meter ahead of this location along the direction of flight (i.e. x-axis). For the Extended Pylon configuration, the Cloud Droplet Probe is located within the mesh at the location [13.92, 2.725, 13.7] and the subset of the scalar fields have also been created for the area up to one meter ahead of this location.

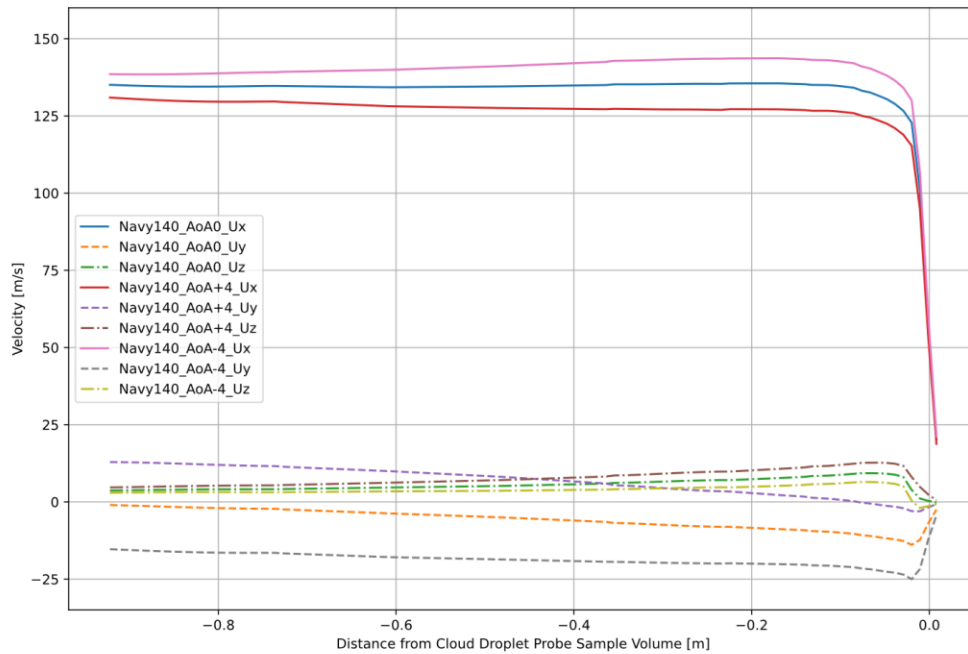


Figure 37: Subset of the velocity field through the mesh leading up to the Cloud Droplet Probe sample volume for the Navy Pylon solutions with the boundary conditions of 140 meters per second freestream and all simulated angle of attacks.

Figure 36 contains the three-dimensional velocity field subset for the Navy pylon simulations described within Fig. 13, 22, and 24 (freestream velocities of 120 ms^{-1} with all angle of attack boundary conditions). As shown in Fig. 36, the main component of the velocity field is contained within the direction of flight (x-axis), which starts to deviate from freestream values up to a meter ahead of the aircraft. As this direction of flight velocity starts to deviate from freestream values, the airflow deviates beneath the CDP sample volume (negative y-component) and in the outboard direction (positive z-component). A similar relationship within the velocity field is shown when the boundary conditions are updated for 140 ms^{-1} freestream airflow, 80000 Pa ambient pressure and 293K temperature within Fig. 37. The overall velocity field is steady and exhibits the same relationships between Fig. 36 and Fig. 37, suggesting the influence of Navy pylon configuration on the relative airflow is independent of initial

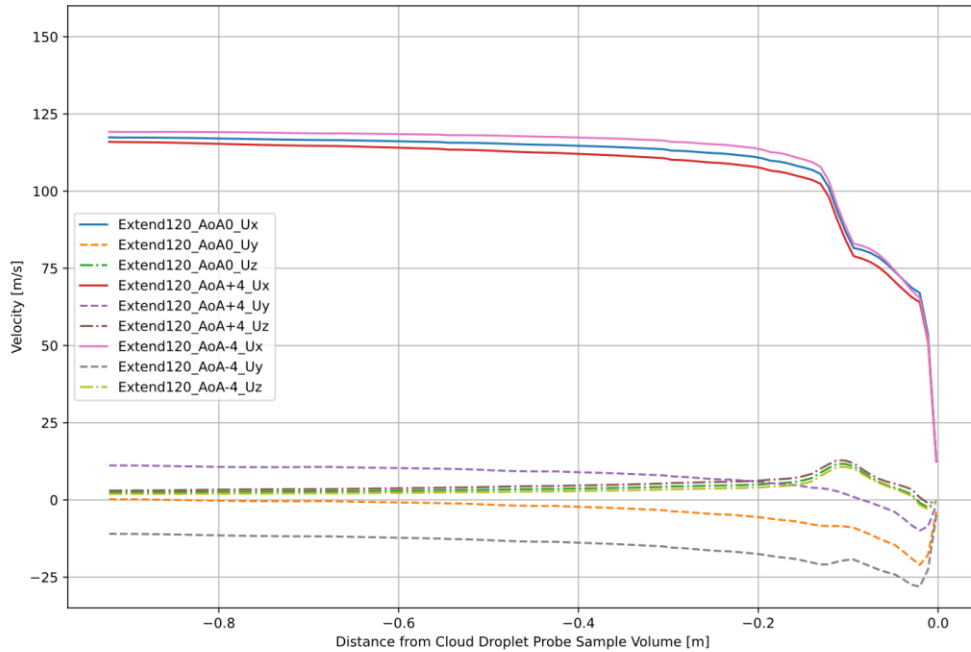


Figure 38: Subset of the velocity field through the mesh leading up to the Cloud Droplet Probe sample volume for the Extended Pylon solutions with the boundary conditions of 120 meters per second freestream and all simulated angle of attacks.

conditions (i.e. airspeed and altitude). However, as shown in both sets of initial conditions and Fig. 13, 22, and 24, the influence of the Navy pylon configuration on the relative airflow is dependent on flight maneuver. Particularly concerning is the sign of this relationship changes for the ‘sawtooth decent’ profile (i.e negative four angle of attack), where there are increased velocities compare to freestream within the meter ahead of the CDP.

Figure 38 contains the three-dimensional velocity field subset for the Extended Pylon configuration simulations shown in Figs. 26, 30, and 32. Similar to the Navy Pylon configuration, the principal component of the velocity field is contained within the flight direction (x-component), with flow compensating beneath and outboard of the Cloud Droplet

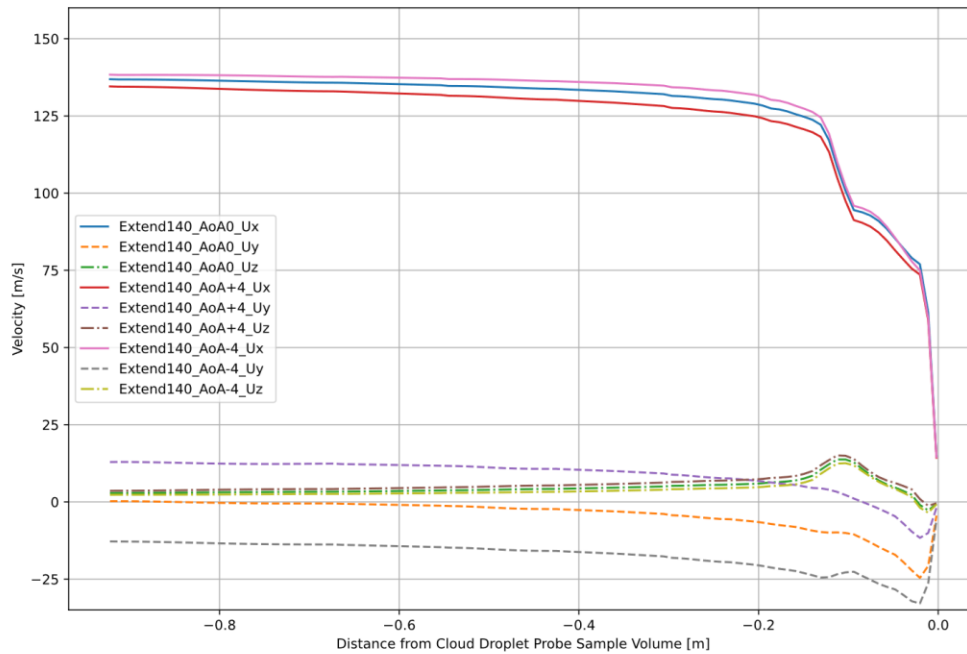


Figure 39: Subset of the velocity field through the mesh leading up to the Cloud Droplet Probe sample volume for the Extended Pylon solutions with the boundary conditions of 140 meters per second freestream and all simulated angle of attacks.

Probe for the deceleration in the direction of flight. However, in contrast to Fig. 36 and Fig. 37, the velocity field within the Extended Pylon simulations begins to decelerate further ahead of the Cloud Droplet Probe and has ‘two moment’ characteristics within the along flight and outboard velocity components. A similar relationship within the velocity field is found within the Extended Pylon simulations initiated with boundary conditions of 140 ms^{-1} airflow, 80000 Pa ambient pressure and 293K temperature within Fig. 36, suggesting the relationship between pylon assembly and relative airflow are independent of initial conditions. In contrast to Figs. 36 and 37, the Extended Pylon configurations shown in Fig. 38 and Fig. 39 does not contain divergence within the along flight component of the velocity field for the various angle of attack boundary conditions. This implies while the Extended Pylon observes a larger area of

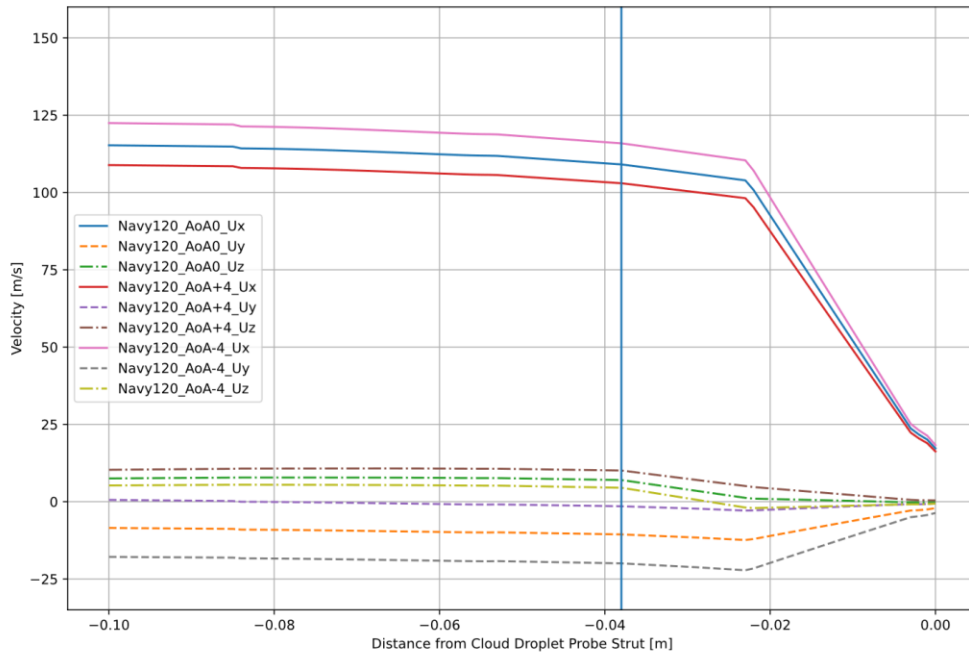


Figure 40: Subset of the velocity field through Cloud Droplet Probe sample volume (marked by vertical blue line) for the Navy Pylon solutions with the boundary conditions of 120 meters per second freestream and all simulated angle of attacks.

deceleration ahead of the Cloud Droplet Probe, unlike the Navy Pylon, it is independent of flight maneuver.

As much of the deceleration within the flow is contained to the portion of the mesh directly ahead of the instrument, Fig. 40 and Fig. 41 narrow the three-dimensional velocity field subsets for the Navy and Extended Pylon configurations to focus on the location of the Cloud Droplet Probe sample volume within the simulations, indicated by the blue vertical line. The location of the Cloud Droplet Probe sample volume was determined by manually measuring the distance between the sample volume and horizontal strut on the instrument within the cloud physics laboratory at the University of North Dakota, which is 1.5 inches (0.038 meters). While Fig. 40 showcases the same tendencies for the Navy Pylon configuration as Fig. 36 and Fig. 37 with the influence of angle of attack on simulations, it does provide some optimism that

overall, Navy Pylon is within 17% of freestream velocities at the sample location of the Cloud Droplet Probe.

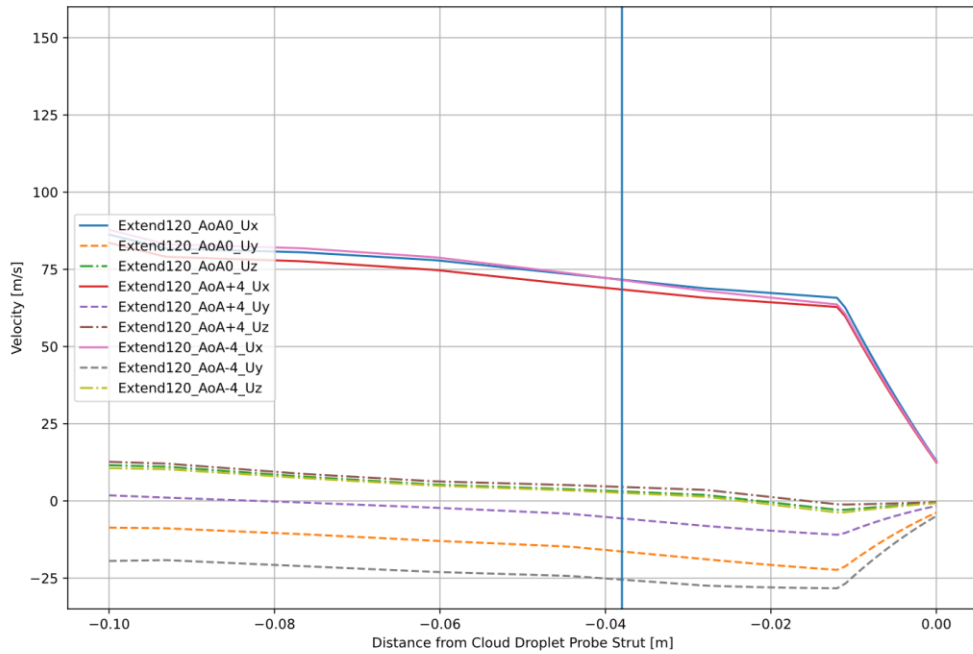


Figure 41: Subset of the velocity field through Cloud Droplet Probe sample volume (marked by vertical blue line) for the Extended Pylon solutions with the boundary conditions of 120 meters per second freestream and all simulated angle of attacks.

While the same cannot be said for the Extended Pylon within Fig. 41, with a stark 62% departure from freestream velocities within the CDP sample volume, there is yet still optimism. With comparison of Fig. 41 to Fig. 42, the Extended Pylon simulations indicate that this departure from freestream velocities appears independent of aircraft maneuvers (shown by the difference in angle of attack) and independent of ambient conditions (shown with the differences in initial boundary conditions). This suggests data collected with the Extended Pylon during ORACLES can be easily corrected for this departure from freestream with a universal offset to the sample volume calculations. While the Navy Pylon simulations are closer to freestream conditions, the same cannot be said for the ORACLES observations

collected with this configuration, as corrections to the data will have to be dependent on angle of attack.

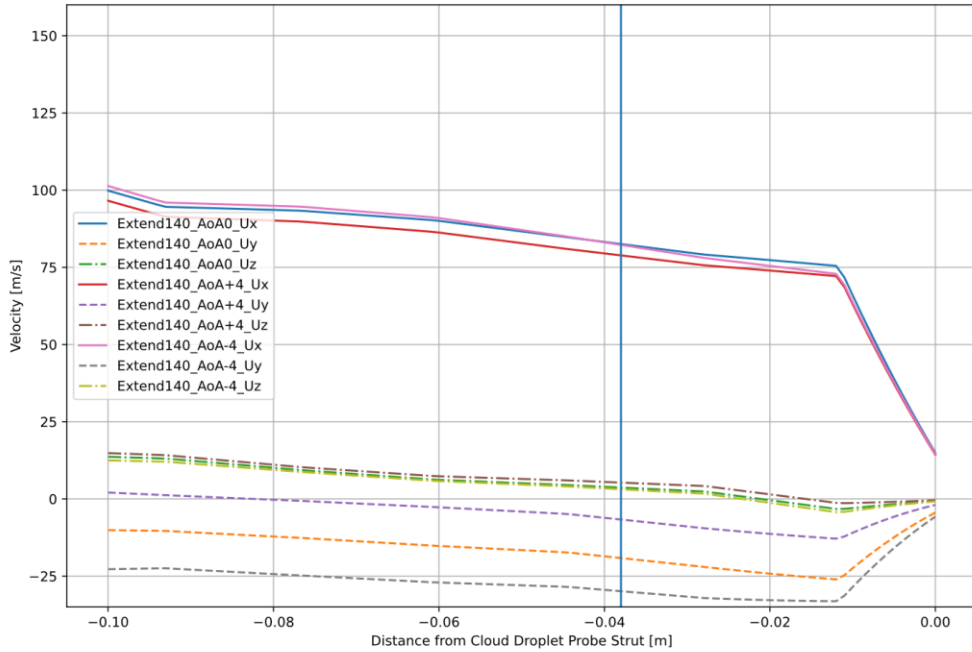


Figure 42: Subset of the velocity field through Cloud Droplet Probe sample volume (marked by vertical blue line) for the Extended Pylon solutions with the boundary conditions of 140 meters per second freestream and all simulated angle of attacks.

To further summarize these results, Table 6 contains the velocity field extracted from the centroid nearest to the location of the CDP sample volume for the Extended Pylon configuration. As shown in previous figures, the velocity at the CDP sample volume is independent of initial boundary conditions. However, as Fig. 41 indicates, all solutions show a marked departure (57%-63%) from freestream. In contrast, the velocity field extracted from the CDP sample volume within the Navy pylon configuration, shown in Table 7, are remarkably close to freestream values (2%-14% departures from freestream). Table 7 does indicate the Navy Pylon contains double the spread (12% relative difference in angle of attack

solutions) in departure from freestream compared to the Extended Pylon (6% relative difference in angle of attack solutions).

Table 6: Extracted velocity values for the nearest centroid to the Cloud Droplet Probe sample volume within the Extended Pylon Simulations and calculated percent of freestream for the magnitude of velocity.

SOLUTIONS	FREESTREAM [m/s]	Ux [m/s]	Uy [m/s]	Uz. [m/s]	Umag % of Freestream
NASA_extendedPylon_v2_tas120 aoa0_900T33	120	71.64	-16.37	3.07	61%
NASA_extendedPylon_v3_tas120 aoaPos4_900T33	120	68.46	-5.67	4.525	57%
NASA_extendedPylon_v3_tas120 aoaNeg4_900T33	120	71.5	-25.49	2.67	63%
NASA_extendedPylon_v3_tas140 aoa0_800T20	140	82.543	-19.15	3.68	61%
NASA_extendedPylon_v3_tas140 aoaPos4_800T20	140	78.87	-6.67	5.28	57%
NASA_extendedPylon_v3_tas140 aoaNeg4_800T20	140	82.25	-29.88	3.12	63%

To extract the effect of the wing itself from this analysis, simulation of the NASA P-3 Orion without pylons or in-situ instrumentation was conducted for the 120 ms⁻¹ and 0° angle of attack boundary condition case. Similar to the process defined above, the velocity field of this No-Pylon solution was extracted for the locations where the Cloud Droplet Probe sample volumes are located within the Navy and Extended pylon solutions. These results are also shown in Table 7 and indicate 1% departure from freestream for either location. This result indicates the departure from freestream ahead of the pylon configurations is due to the pylon and instrument assembly, and not due to the influence of the aircraft wing. However, these results also indicate an inherent 2% difference between Cloud Droplet Probe sample volumes is the result of the wing.

Finally, intercomparison between instruments on the NASA P-3 during ORACLES was original method to understand airflow around these two separate pylon assemblies. Comparison between Table 6 and Table 7 indicates the relative difference within the velocity

Table 7: Extracted velocity values for the nearest centroid to the Cloud Droplet Probe sample volume within the Navy Pylon Simulations and calculated percent of freestream for the magnitude of velocity. Additionally, extracted velocity values for simulation of the NASA P-3 without pylons for the Cloud Droplet Probe sample volume locations within the Navy and Extended Pylon simulations.

SOLUTIONS	FREESTREAM [m/s]	Ux [m/s]	Uy [m/s]	Uz. [m/s]	Umag % of Freestream
NASA_navyPylon_v2_tas120 aoa0_900T33	120	109.07	-10.58	6.99	92%
NASA_navyPylon_v3_tas120 aoaPos4_900T33	120	102.98	-1.48	10.82	86%
NASA_navyPylon_v3_tas120 aoaNeg4_900T33	120	115.89	-19.95	4.49	98%
NASA_navyPylon_v3_tas140 aoa0_800T20	140	126.96	-12.55	8.40	91%
NASA_navyPylon_v3_tas140 aoaPos4_800T20	140	119.18	-1.95	11.98	86%
NASA_navyPylon_v3_tas140 aoaNeg4_800T20	140	134.44	-23.40	5.41	98%
NASA_noPylons_v2_tas120 aoa0_900T33. Navy CDP Location	120	121.41	-3.58	3.88	101%
NASA_noPylons_v2_tas120 aoa0_900T33. Extended CDP Location	120	118.49	-1.55	3.00	99%

fields between the Navy and Extended pylons within the Cloud Droplet Probe sample volumes. For the constant altitude cloud legs, the Extended Pylon experienced a 30% larger departure from freestream velocities than the Navy Pylon. Within the sawtooth profiles, simulated via changing angle of attacks within this framework, the Extended Pylon experienced 29% larger departure from freestream for the ‘sawtooth climb’ profiles and a 35% larger departure from freestream for the ‘sawtooth descent’ profiles.

LAGRANGIAN PARTICLES

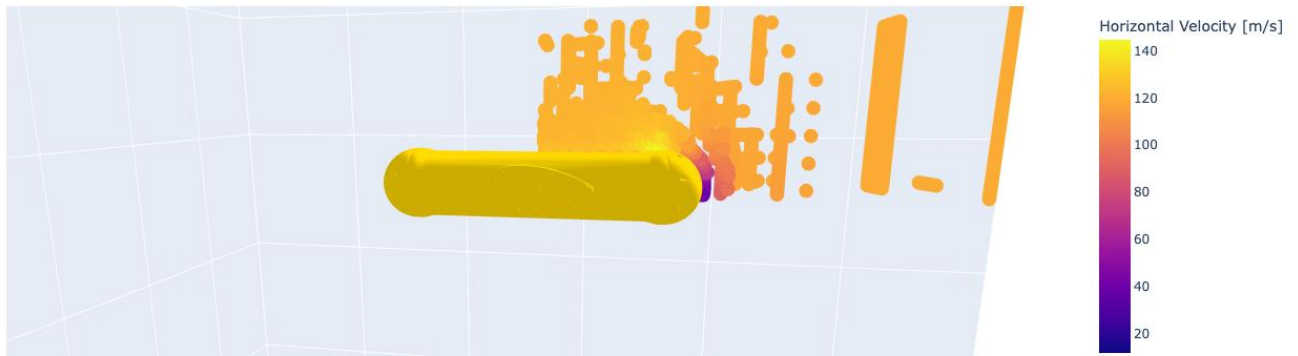


Figure 43: Simulated Lagrangian particles (10 micron in diameter, 100 #/cc concentration) for the compressible flow simulation of airflow around a Particle Measurement System canister used during ORACLES. Particles are shaded with calculated horizontal velocities, with a departure from freestream centered in front of the canister.

To study the effect of these twelve flow simulations on the full range of in-situ observations observed during ORACLES, simulation of Lagrangian Particles at three specific diameters (e.g. 10, 50, 100 microns) and four cloud droplet number concentrations (e.g. 50, 100, 200, 300 per cubic centimeter) was proposed. As Lagrangian Particle processing within OpenFOAM is conducted a posteriori for each flow simulation, a total of 144 simulations were planned to cover the full range of ORACLES observations. At the time of this proposed methodology, it was assumed that the *uncoupledKinematicParcelFoam* was capable of multicore processing. For the compressible flow simulations, the mesh creation and associated solver *rhoSimpleFoam* equally split the mesh creation and analysis mesh across six processors. This is a significant advantage of the underlying file format and mesh geometry of OpenFOAM. As each point, face, cell and element of the mesh have explicit information detailing communication between each, the *decomposePar* utility allows for the mesh and calculations to be split across computational resources. However, as Lagrangian Particles do not have the explicit information to relate to each of these points, faces and cells within the mesh, separation of the processing across multiple cores was determined too not be possible.

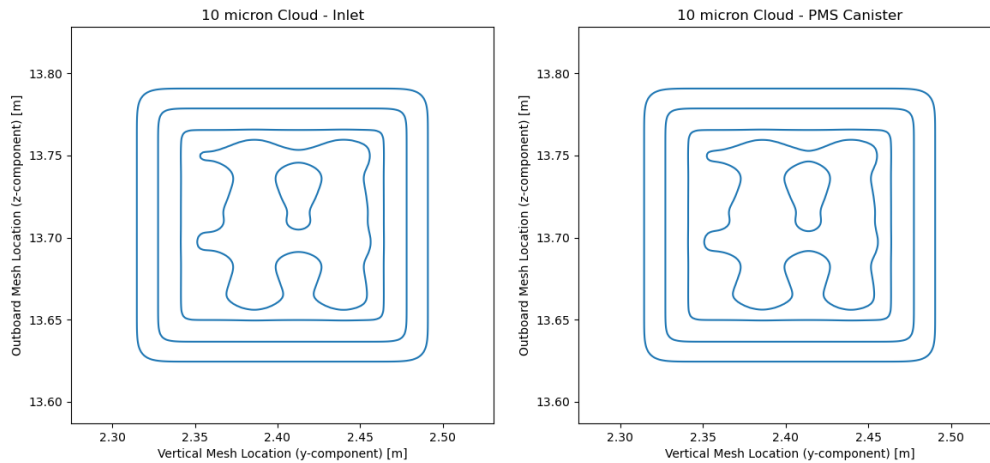


Figure 44: Kernel Density Estimation for simulated particles (10 microns, 100 #/cc) within the compressible flow simulation around the Navy Pylon configuration. Left side of figure contains kernel density for the simulation inlet, while right side of figure contains estimate for particles directly in front of the Cloud Droplet Probe canister. Contoured are 99% of all particles.

Through testing, it was determined that the University of North Dakota computational resources allowed for the processing of 50,000 Lagrangian particles for a single OpenFOAM simulation, a quarter of the particles simulated within Spanu et al. (2020). This single Lagrangian Particle simulation would require close to forty percent of the available memory of these computational resources. This memory usage was large enough to limit the processing to two simultaneous simulations for the Navy and Extended pylon during low usage by the rest of the research group. Finally, with a single processor, a single Lagrangian particle simulation would require ten days to converge to a solution. With the assumption that this analysis would be afforded the computational resources to run undisturbed, the computational cost would be nearly four years of continuously processing to simulate three particle diameters at four concentrations per flow simulation. With these computational restrictions, the size of Lagrangian Particles simulated were limited to ten microns in diameter and cloud droplet concentration number limited to 100 per cubic centimeter within this study.

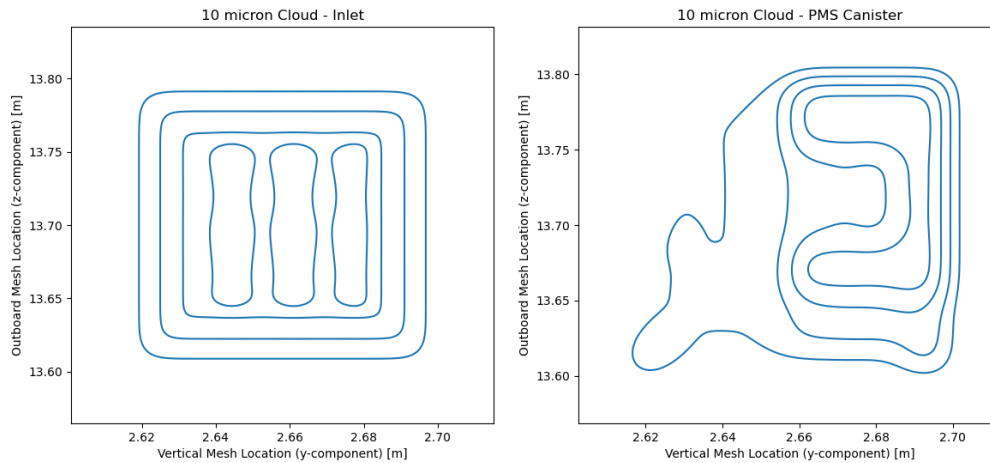


Figure 45: Kernel Density Estimation for simulated particles (10 microns, 100 #/cc) within the compressible flow simulation around the Extended Pylon configuration. Left side of figure contains kernel density for the simulation inlet, while right side of figure contains estimate for particles directly in front of the Cloud Droplet Probe canister. Contoured are 99% of all particles.

To determine the sampling efficiency of each pylon configuration, the ratio of the concentration of Lagrangian particles within the Cloud Droplet Probe sample volume to the concentration of particles released at the domain inlet is calculated. To compensate for the change in grid resolution at the inlet verse the Cloud Droplet Probe sample volume within the domain, kernel density estimation plots are shown for Lagrangian Particle simulations within Figure 44 and Figure 45. As shown in Figure 44, the kernel density estimation plot for the Navy Pylon configuration indicates no change within the probability density function for Lagrangian particles. For the simulation of fifty thousand particles at 100 per cubic centimeter initial concentration, the Navy Pylon was found to have 90% sampling efficiency. As for the Extended Pylon shown in Figure 45, a distortion within the probability density function is shown for the instrument location, with a larger density of Lagrangian particles found outboard of the initial configuration location. As the Extended Pylon simulations contain larger departures (and further extent of departure ahead of the leading edge) from freestream

conditions compared to the Navy Pylon simulations, this outboard shift within particle locations could be the result increase in outboard lateral flow along the aircraft wing as they decelerate ahead of the wing. Finally, in contrast to the Navy Pylon simulations, the Extended Pylon configuration was found to have a 70% sampling efficiency.

CHAPTER V DISCUSSION

THE MYTH OF IN-SITU FREESTREAM OBSERVATIONS

Prior to the ORACLES-2016 deployment to Namibia, and within the first week of instrument integration at NASA Wallops Flight Facility, concerns were raised about the location of University of North Dakota's in-situ cloud microphysical instrumentation on the NASA P-3 Orion. The concerns with the location of these instrumentation were raised by the Jet Propulsion Laboratory's Airborne Precipitation Radar Version 3 team, who were concerned about the location of the instruments with respect to the aircraft props and the potential for propeller wash to affect hydrometer distributions. This discussion spurred many additional conversations about the validity of the instruments, particularly with respect to the leading edge of the aircraft. At the time, intercomparison between the Droplet Measurement Technology Cloud and Aerosol Spectrometer and Atrium Dual Phase Interferometer revealed a relationship within cloud droplet number concentration that varied with aircraft pitch angle. With the prospect that original pylon configuration was influenced by the sawtooth maneuvers, the sampling profile used to observe the majority of cloud observations during ORACLES, efforts were made to create a new pylon that would sample as close to freestream environmental conditions. After consultation with international airborne research groups, it was determined that a pylon that allowed the instruments to sample as far beneath and ahead of the aircraft wing would achieve conditions as close to freestream.

While the ability to perform a computational fluid dynamics analysis was beyond the capabilities of the University of North Dakota – Cooperative Institute for Severe and High-Impact Weather Research and Operations team at the end of the ORACLES-2016 campaign, if conducted, the assumption to move the instruments further below and farther ahead of the

wing would have stood. As Fig. 13 indicates, the CDP sample volume on the Navy Pylon is near freestream conditions, with freestream conditions (based on velocity field contours) is just ahead and beneath the instrument. The simulations of the sawtooth maneuver through the changing of relative flow angle around the pylon assembly would have validated the `Cloud Probes team` concerns that the Navy Pylon was susceptible to the sawtooth profiles. Table 7 highlights this fact with a 14% departure in freestream conditions for the `sawtooth climb` portions and a 2% departure in freestream velocities for the `sawtooth decent` profiles. A 12% relative difference within the dataset between vertical profile maneuvers would have been cause of concern and adjustments to the pylon would have been requested.

With the creation of the Extended Pylon configuration for ORACLS-2017 and ORACLES-2018, as shown in Table 6, observation of freestream conditions was not achieved for this pylon assembly. However, minimization of the effects of the sawtooth maneuvers upon the velocity field sampled at the instrument location was achieved, with a 6% relative difference between `sawtooth ascent` and `sawtooth descent` profiles. Much of this departure from freestream conditions should be attributed to the width of the Extended Pylon configuration, which was required to provide structural integrity to place the instruments ahead of the leading edge of the aircraft. While achieving the objective of instrument placement, this structure provides increased surface area (and thus increased ram pressure) compared to the Navy pylon.

Even for the Extended Pylon, as shown in Fig. 26, the original hypothesis that freestream conditions are just ahead and beneath the instrument can be inferred. However, this hypothesis will always be inferable for sub-sonic aerodynamic flow. As described within Chapter 2, within subsonic aerodynamic flow, disturbances within the flow will propagate both upstream and downstream and will influence the entire flow field. Therefore, based on the results provided

within this analysis, a pylon configuration to achieve freestream atmospheric conditions for in-situ instrumentation (integrated into an aircraft moving at sub-sonic airflow) is not achievable.

LIMITATIONS IN INSTRUMENT PLACEMENT

For airborne atmospheric research, regardless of the scientific objectives, the quality of the observations will always assume a subsidiary role to the engineering and safety requirements of the aircraft. While one can theorize that an Extended pylon with slimer struts would help lessen the increase in Ram pressure (and thus decrease the velocity departure), this was not achievable for the NASA P-3 Orion. This is due to the engineering requirements that this new pylon assembly be able to withstand high gravitational loads as defined within the US Navy P-3 Orion aircraft technical documentation. Additionally, as the case with every aircraft, there are limited hardpoints, or locations designed into the airframe that can carry an external or internal payload, to instrument for atmospheric research. Every airborne atmospheric research aircraft (and realistically any moving observational platform) will share these issues. Therefore, it is critical that each observation platform undergo a computational fluid dynamic analysis to understand potential impacts of instrument location on the observations. Furthermore, as indicated with the analysis presented within, this analysis should include simulation of the typical flight maneuvers to characterize the airflow the in-situ instrumentation will encounter. It is the hope of this dissertation that the results, procedure, and appendices provided here will showcase that this is achievable with an interdisciplinary approach to the topic with university resources, graduate student funding, and patience.

LIMITATIONS WITHIN THE NASA P-3 MODEL

As with every numerical model, there are limitations to the physical characteristics and physical phenomena represented within the simulations. The NASA P-3 Orion with Navy and Extended Pylon configurations within this study are not a complete representation of the

aircraft and instrumentation and are not expected to be. The NASA P-3 CAD drawings supplied by the NASA Wallops Flight facility originally did not contain either pylon configuration. Subsequent conversations with NASA Wallops helped produce CAD drawings with associated instruments for both pylons, and these drawings were merged into the NASA P-3 model with the methodology described in Chapter 3. The NASA P-3 flown during the ORACLES 2016-2018 campaigns contained four separate pylons, with two pylons per wing location. For ORACLES-2016, all pylons were of the Navy Pylon configuration. For 2017 and 2018, the outboard pylon on the port side of the aircraft contained the Extended pylon configuration. Due to the limits of computational resources, only the port side outboard pylon was modeled within his study. This was deemed appropriate for these simulations as the Cloud Droplet Probe was located at the most outboard instrument on either wing during ORACLES-2018. As Fig. 19 and Fig. 27 indicate, the lateral flow along the wing (inboard outboard directions) extends roughly a meter to either side of the pylons. With similar expected flow distortion around a pylon situated further inboard on the port side of the aircraft, it is very likely these distortions interact. However, as Table 6 and Table 7 indicate, the percentage of the total velocity field within the Cloud Droplet Probe sample volume these lateral flow components contribute to is less than ten percent of the total flow. Therefore, as the primary signal within the along flight direction, the influence of the inboard pylon location is expected to be minimum.

Another major discrepancy between the actual NASA P-3 Orion and the modeled version within these simulations is the lack of propellers within the model geometry. While the P-3 CAD drawings provided by NASA Wallops Flight facility provided accurate descriptions of the four aircraft engines, these drawings did not contain propellers. Even if the NASA P-3

CAD drawings contained the propellers, in order to accurately simulate the rotation, the mesh would have to be rotated within these areas greatly increasing the complexity of the meshing process. Potentially, remeshing of propellers would be required for each iteration of the *rhoSimpleFoam* solver to simulate rotational movement, removing any possibility of achieving results for a variety of flow angles and boundary conditions due to processing time restrictions. Even a simplistic disk as a stand in would not have been sufficient to simulate the propellers as it would have had the opposite anticipated pressure effect, creating an area of increased pressure ahead of the propeller verse lower pressure expected. While there have been multiple computational fluid dynamic studies that performed successful simulation of propellers for various Reynolds flow regimes on aircraft and ships, the main focus of those simulations were the rotational efficiency of the propeller itself. Therefore, any effort taken to narrow in and produce a working simulation for the NASA P-3 Orion with appropriate propellers would have taken the focus away from the airflow around the pylon configurations.

Propellers are expected to create an area of low pressure directly ahead of the aircraft engines, producing an effect of dragging the aircraft forward. A tight gradient within the pressure field could be expected ahead of these locations, as the aircraft forward motion will also increase Ram pressure. Therefore, the impact on the pressure field must be contained near or directly in front of the propellers. It is possible this low pressure induces an inboard directed velocity component that could disrupt airflow ahead of the inboard pylons on the NASA P-3.

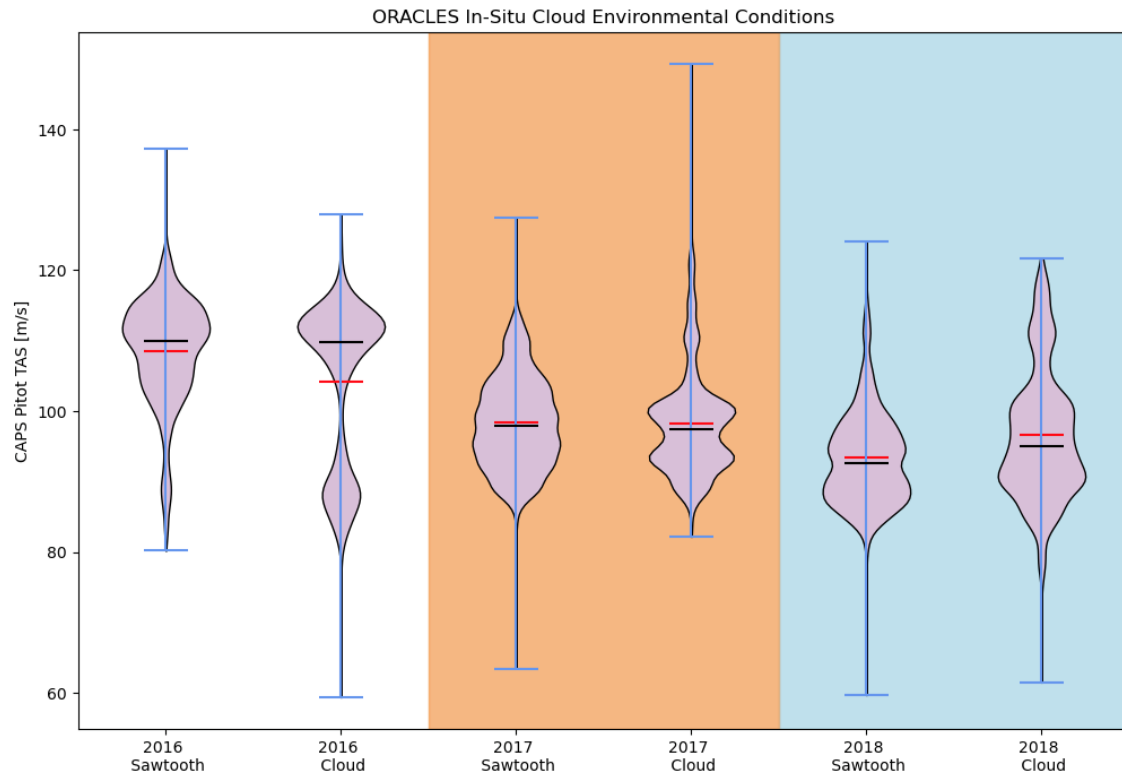


Figure 46: Distribution of observed true air speed (meters per second) from the Cloud, Aerosol, Precipitation Spectrometer during ORACLES for specific cloud sampling profiles. For ORACLES 2016, the Cloud, Aerosol, Precipitation Spectrometer was mounted on the Navy pylon configuration, while it was mounted on the Extended Pylon for ORACLES 2017 and ORACLES 2018.

However, at the air speeds tested within this study, Table 6 and Table 7 indicate these lateral velocity components are small portion of the velocity field in the direction of flight. Additionally, as the propellers are much further inboard than the pylons modeled within this study, the impact of the propellers within the Cloud Droplet Probe sample volumes are expected to be minimum.

RELATEABILITY OF SIMULATIONS TO OBSERVATIONS

Spanu et al. (2020) successfully modeled compressible flow around the Dassault Falcon 20E-5 (registration D-CMET) with a pylon configuration that placed the instruments ahead of the leading edge of the aircraft wing. While Spanu et al. (2020) did not perform compressible flow simulations with a pylon configuration behind the leading edge of the aircraft, or aircraft

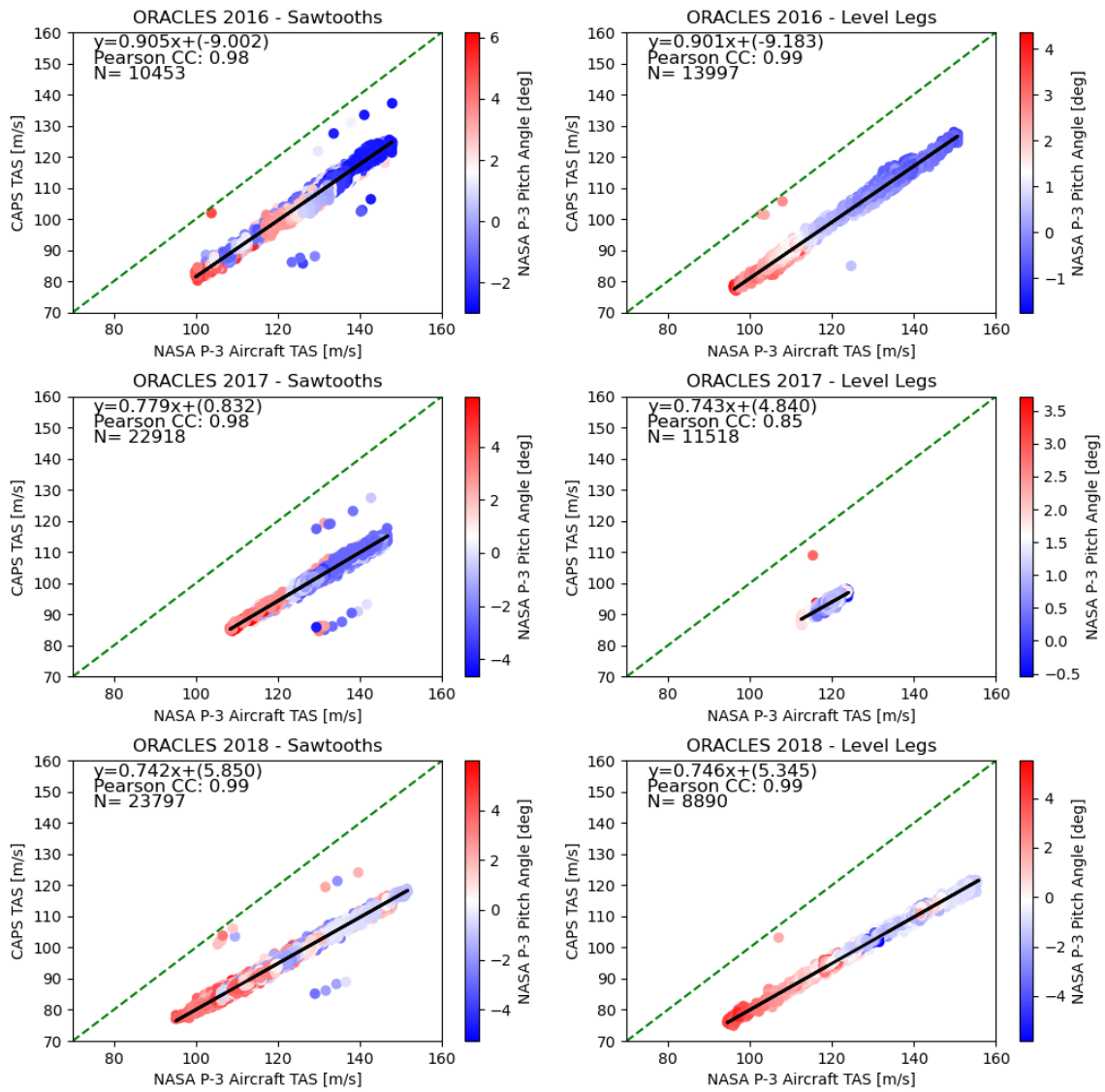


Figure 47: Comparison of true air speed observations between the Cloud, Aerosol, and Precipitation Spectrometer and NASA P-3 fuselage. For ORACLES 2016, the Cloud, Aerosol, Precipitation Spectrometer was mounted to the Navy Pylon on the port side outboard pylon. For ORACLES 2017, at the same location, the Cloud, Aerosol, Precipitation Spectrometer was mounted to the Extended Pylon.

maneuvers within their modeling framework, their simulations indicate a 15% - 20% departure from freestream conditions at the inlet of the Cloud, Aerosol, and Precipitation Spectrometer pitot static probe (Fig. 5 within the paper). A further departure from freestream conditions is

ORACLES 2018 - SAWTOOTHS - [5 #/cc cloud threshold]

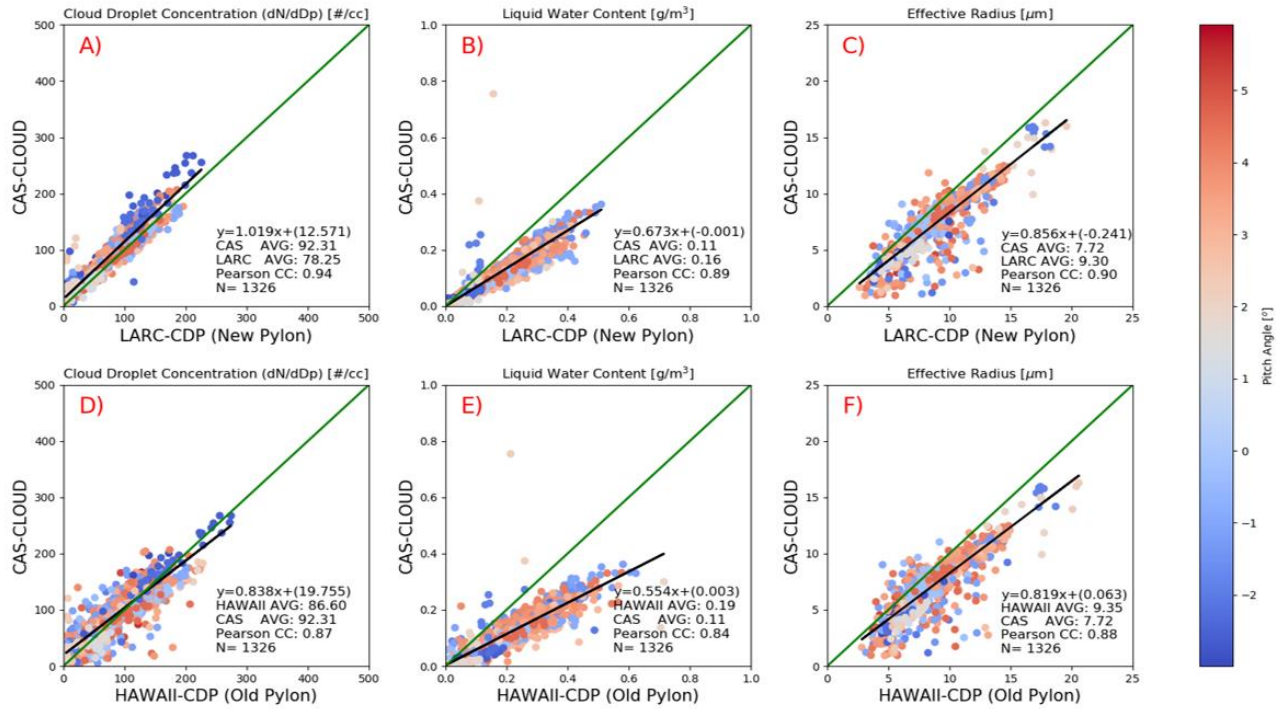


Figure 48: Comparison of Cloud and Aerosol Spectrometer with two Cloud Droplet Probes during the sawtooth cloud profiles from ORACLES 2018. Within this figure, New Pylon refers to the Extended Pylon configuration, while Old Pylon refers to Navy Pylon configuration.

shown as the distance narrows from the instrument head, where the Cloud Droplet Probe would be situated within the modeling framework defined within this study. Spanu et al. (2020) also indicate an underestimation of air speed by 26% compared to free stream values for the Cloud, Aerosol, and Precipitation Spectrometer pitot static probe. Additionally, Spanu et al. (2020) simulations also indicate a velocity field is independent of initial conditions, where similar departure from freestream is shown for five velocity-pressure combinations.

For ORACLES, the Cloud, Aerosol, Precipitation Spectrometer was installed onto the NASA P-3 Orion port-side outboard pylon for all three campaigns. During ORACLES-2016, the Cloud, Aerosol and Precipitation Spectrometer was installed onto the Navy Pylon and was installed into the Extended Pylon during ORACLES-2017 and ORACLES-2018. Thus, an estimate of the local flow impacts by this pylon change can be found through a comparison of

observed true air speed from the instrument the pitot static verse the observed true air speed from the NASA P-3 fuselage. Figure 45 contains the violin plots for the Cloud, Aerosol, Precipitation Spectrometer across all campaigns for the cloud sampling profiles. As indicated by highlight density distributions, there is a shift within the distributions towards slower airspeeds for ORACLES-2017 and ORACLES-2018, when the instrument was mounted to the Extended Pylon, supporting the simulated results within this study. Interestingly, for the ORACLES-2017 and ORACLES-2018 sawtooth distributions, the distribution mean (red line within figure) and median (black line within figure) are nearly identical, supporting simulation results that the Extended Pylon was nearly independent to flow angle. Figure 46 contains the direct comparison of true air speed between the Cloud, Aerosol, and Precipitation Spectrometer and the NASA P-3 fuselage observations. While the wing mounted instruments reported lower true air speed observations than the fuselage throughout all three campaigns, the relationship between locations changes after ORACLES-2016. Based on the flow simulations, an expected change from switching pylons is roughly 30% decrease in velocities for sawtooth profiles. Comparison of the slope of the best fit line between 2016 sawtooth profiles and 2017 sawtooth profiles subplots within Fig. 46 indicate half the anticipated effect.

Finally, with computational fluid dynamic simulations for the cloud sampling profiles observed during ORACLES, the observational comparison for the sawtooth profiles is shown between all forward scattering instrumentation (e.g. Cloud and Aerosol Spectrometer and two Cloud Droplet Probes) within Fig. 47. As the Cloud and Aerosol Spectrometer suffered a critical malfunction during the second half of ORACLES-2018, this comparison is only conducted for the first six flights of the campaign. Within the figure, the Extended Pylon is labeled as New Pylon and the Navy Pylon is labeled Old Pylon. Figure 47a compares cloud

droplet number concentrations from instruments both situated on the Extended Pylon and contains good agreement between instruments. In support of the flow simulations within this study, when furthering the cloud droplet number concentration comparison to include the Cloud Droplet Probe mounted to the Navy pylon, the Navy pylon observations contain higher concentrations as indicated by the slope of the best fit line. Additionally, comparison of the mean liquid water content between Cloud Droplet Probes between Fig. 47b to Fig. 47e 15% more mass observed at the Navy Pylon location compared to the Extended Pylon.

CHAPTER VI

CONCLUSION

ORACLES (ObseRvations of Aerosols above CLouds and their intEractionS) was a five-year NASA investigation into the climate impacts of Southern Africa's biomass burning aerosols (Redemann et al. 2021). Three separate airborne field campaigns were conducted to investigate the interactions of this biomass burning aerosol plumes on the semi-permanent marine stratocumulus region within the Southern Atlantic Ocean in September 2016, August 2017, and October 2018. Due to the remote nature of this region, ORACLES remains one of the only airborne field campaigns to study aerosol cloud interactions within this environment. The Southern Atlantic Ocean has critical importance for climate forcing within global climate models and aerosol cloud interactions continue to have one of the largest uncertainties remaining within this forcing. Therefore, it is of critical importance that the ORACLES cloud microphysical dataset has the highest possible quality to allow researchers to explore these interactions and understand the implications for future climate scenarios.

The combined University of North Dakota and The Cooperative Institute for Severe and High-Impact Weather Research and Operations at the University of Oklahoma research team have provided three quality-controlled datasets spanning all ORACLES campaigns (O'Brien et al. 2021). These cloud microphysical datasets contain the size distribution of clouds and aerosols from 0.1 microns to 1.95 centimeters in diameter, as well as, the liquid water content for hydrometeors observed during all ORACLES campaigns. As this combined Cloud Probes team operated a variety of in-situ instrumentation with overlapping observational ranges, the combined microphysical dataset represents the recommended instrument for use within additional studies. However, as indicated within O'Brien et al (2021), through intercomparison

between all cloud microphysical instrumentation, there are large discrepancies within cloud droplet concentrations and liquid water content between instrumentation. These discrepancies have long been included within airborne in-situ cloud microphysical datasets and often attributed to sampling techniques or relative airflow around instrument mounting locations.

The concern within the discrepancies in cloud droplet concentrations between the in-situ cloud microphysical instrumentation after ORACLES-2016 led questions on the accuracy of the measurements and the affects of mounting locations on the dataset. For ORACLES-2016, all instruments were placed on pylons such that the instruments were situated behind the leading edge of the NASA P-3 Orion wing. To compensate, a new pylon design was created for ORACLES-2017 and ORACLES-2018 that placed the Cloud and Aerosol Spectrometer and Cloud Droplet Probe as far ahead and beneath the aircraft wing as possible. For ORACLES-2018, an additional instrument intercomparison study was conducted with two Cloud Droplet Probes situated on both pylons. Yet, even with this intercomparison, questions on the airflow around these pylons remained, particularly if the dataset is representative of the ambient marine stratocumulus environment.

To compensate the instrumentation analysis, a computational fluid dynamics study of airflow around the NASA P-3 Orion with associated pylon configurations was shown within this analysis. Utilizing OpenFOAM, an open source computational fluid dynamics software, and FreeCAD, an open source computer-aided design software, models of the NASA P-3 Orion with the Navy and Extended pylon were incorporated into a complex, non-uniform grid consisting of hexagonal and triangle elements. With the compressible flow solver *rhoSimpleFoam*, twelve simulations of airflow around the NASA P-3 were conducted. Boundary conditions for the equations of motion were derived from mean environmental

conditions observed during ORACLES. Two sets of aircraft airspeed, temperature, and pressure combinations were chosen to determine the sensitivity of the solutions to input boundary conditions. This study, to the authors knowledge, was the first time in-situ aircraft sampling profiles were simulated. As the majority of ORACLES in-situ cloud profiles were taken in vertical maneuvers through the depth of the marine stratocumulus known as `sawtooths`, simulation of these profiles was conducted though altering the velocity field boundary condition.

To determine the affect of the pylon configuration on the relative airflow, the velocity field within the modeled Cloud Droplet Probe sample volume was extracted and compared to each simulation's boundary conditions. The Navy Pylon configuration was found to best agree with freestream conditions, with a 14% maximum departure from freestream. However, the Navy Pylon configuration was found to be dependent on the angle of the airflow and susceptible to sawtooth maneuvers with a relative 12% change in the departure from freestream when comparing sawtooth ascents verse sawtooth decent profiles. Overall, the sawtooth decent profiles were the closest to freestream conditions observed for either pylon configuration. The Extended Pylon configuration had a marked departure from freestream, with a minimum of any simulation with a 57% departure from freestream for the sawtooth decent profiles. However, in contrast to the Navy Pylon, the Extend Pylon was less dependent on the angle of the airflow with only a 5% relative change in the departure form freestream when comparing sawtooth ascents to decent profiles.

CONSIDERATIONS FOR FUTURE AIRCRAFT

To design modifications for aircraft to accommodate scientific research, significant resources are spent to ensure no harm to the crew, passengers or airframe occurs. In most cases,

these modifications are reviewed and approved by the Federal Aviation Administration. For the pylon configurations described within this dissertation, the NASA Wallops Flight Facility was required to engineer pylons that met specific requirements, such as gravitational and vibrational loads, as outlined within the Navy P-3 Orion B aircraft manual. Computational fluid dynamical simulations were necessary for engineering approval of these pylon configurations, particularly stress analysis of the material to verify it can withstand the specific engineering requirements. However, these simulations rarely consider the implications for scientific research and are designed to analyze stress coefficients that are not easily transferable to scientific research (i.e. airflow analysis).

As highlighted within, a single rule to decouple the engineering requirements from the scientific applications is impossible. The proposed general rule by the ORACLES cloud probes team to move the instrument ‘as far ahead and beneath the wing as possible’ did not result in a universal solution for wing mounted instrumentation, as the Extended Pylon configuration resulted in significant departures from freestream conditions. As shown in this analysis, significant departure from freestream conditions also resulted due to the profiling strategies defined by the ORACLES campaign, as the Navy Pylon configuration is shown to be dependent on the angle of attack of the aircraft. This suggests that different solutions are required for the different scientific objectives (i.e. profiling schemes). As only the main ORACLES cloud sampling profiles were considered within this study, efforts should be made to simulate all critical aircraft maneuvers for future campaigns. As Table 6 indicates a substantial outboard velocity component, the effect of a sustained roll maneuver (such as spiraled descents) on particle orientation within the instrument sample volumes should be explored. Additionally, flight profiles that contain sudden changes in velocities (such as

constant altitude flight speed increases) and small continuous changes within pitch should be explored. These procedures are common within the airborne research community to calibrate aircraft derived winds and vertical velocities. Understanding of the flow angle on the aircraft pitot static probes during these maneuvers may help to further reduce the uncertainties within these derived fields and give validity to any future simulation.

As the simulations within have shown, the relationship of airflow within the sample volume of the Cloud Droplet Probe to freestream conditions is found to be independent of initial freestream airspeed. Therefore, a single set of environmental conditions for sub-sonic aerodynamic airflow should suffice to accurately describe the three dimensional flow field around any future engineering effort or planned research aircraft. Emphasis should be placed on the relative angle of the airflow at the location of wing-mounted instrumentation, with a range of angle of attacks explored. It should be noted that this analysis only considers sub-sonic aerodynamical airflow. With the anticipated restart of the supersonic commercial flight industry, future work into the exploration of pressure-based aerodynamic solvers to resolve the shock waves generated by supersonic aerodynamic flight will be needed. It is not anticipated that such platforms will provide meaningful cloud in-situ microphysical observations. However, the pitot static probes could provide meaningful observations of stratospheric environmental observations and the exploration of the flow angle on these instruments during supersonic flight should be explored.

Lastly, this research did not consider mixed phase environmental or aircraft icing conditions. As aircraft icing has long been an area of active research within the atmospheric science community, special considerations should be given to these cases to understand the influence of the velocity field around these instrument locations on ice accumulation for new

engineering requirements. The techniques described within offer the potential to simulate ice accumulation with slight modifications to the boundary conditions of the Lagrangian particles simulated, allowing OpenFOAM to track the mass that encounters specific aircraft components.

For the NASA P-3 Orion pylon configurations, considerable resources were spent by both the engineering and science teams to create a pylon design to meet the necessary aircraft engineering requirements and to analyze the atmospheric airflow around these pylons to understand the implications to the observations. Due to the nature and timeline of ORACLES, these efforts were disjointed and not collaborative. Additionally, this analysis required immense training and tinkering with a variety of software and modeling frameworks to be completed. It is a sincere hope that the methodology and configuration files provided within will allow future endeavors to quickly summit this steep learning curve. However, for future aircraft, the path of least resistance to provide an adequate pylon configuration for atmospheric observations is through the inclusion of science requirements to all engineering computational fluid dynamics simulations. These requirements should include:

1. A design that results in airflow velocities within the instrumentation sample volume to be within 10% of freestream conditions.
2. A design that results in the independence of airflow within the instrumentation sample volume from aircraft maneuvers.
3. Simulations are provided to the science team for reference and future analysis.

REFERENCES

Ahrens, J., B. Geveci, and C. Law, 2005: *Paraview: An end-user tool for large data visualization*. Elsevier,.

Albrecht, B. A., 1989: Aerosols, cloud microphysics, and fractional cloudiness. *Science*, **245**, 1227+.

Andela, N., and Coauthors, 2017: A human-driven decline in global burned area. *Science*, **356**, 1356–1362, <https://doi.org/10.1126/science.aal4108>.

Anderson, J. D., 2003: Flight (Aerodynamics). *Encyclopedia of Physical Science and Technology (Third Edition)*, R.A. Meyers, Ed., Academic Press, 1–21.

Barrett, P. A., and Coauthors, 2022: Intercomparison of airborne and surface-based measurements during the CLARIFY, ORACLES and LASIC field experiments. *Atmospheric Meas. Tech.*, **15**, 6329–6371, <https://doi.org/10.5194/amt-15-6329-2022>.

Bellouin, N., and Coauthors, 2020: Bounding Global Aerosol Radiative Forcing of Climate Change. *Rev. Geophys.*, **58**, e2019RG000660, <https://doi.org/10.1029/2019RG000660>.

Bennett, C. J., G. J. Nott, A. Wellpott, N. Lawson, M. Delise, B. Woodcock, and G. B. Gratton, 2019: Characterizing Instrumentation Canister Aerodynamics of FAAM BAe-146-301 Atmospheric Research Aircraft. *J. Aerosp. Eng.*, **32**, 04019047, [https://doi.org/10.1061/\(ASCE\)AS.1943-5525.0001044](https://doi.org/10.1061/(ASCE)AS.1943-5525.0001044).

Boucher, O., and Coauthors, 2013: Clouds and Aerosols. *Clim. Change 2013 Phys. Sci. Basis Contrib. Work. Group Fifth Assess. Rep. Intergov. Panel Clim. Change*, 571–657.

Brioude, J., and Coauthors, 2009: Effect of biomass burning on marine stratocumulus clouds off the California coast. *Atmos Chem Phys*, **9**, 8841–8856, <https://doi.org/10.5194/acp-9-8841-2009>.

Chand, D., R. Wood, T. L. Anderson, S. K. Satheesh, and R. J. Charlson, 2009: Satellite-derived direct radiative effect of aerosols dependent on cloud cover. *Nat. Geosci.*, **2**, 181–184, <https://doi.org/10.1038/ngeo437>.

Chen, G., Q. Xiong, P. J. Morris, E. G. Paterson, A. Sergeev, and Y.-C. Wang, 2014: OpenFOAM for Computational Fluid Dynamics. *Not. Am. Math. Soc.*, **61**, 354, <https://doi.org/10.1090/noti1095>.

Coakley, J. A., and P. Chylek, 1975: The Two-Stream Approximation in Radiative Transfer: Including the Angle of the Incident Radiation. *J. Atmospheric Sci.*, **32**, 409–418, [https://doi.org/10.1175/1520-0469\(1975\)032<0409:TTSAIR>2.0.CO;2](https://doi.org/10.1175/1520-0469(1975)032<0409:TTSAIR>2.0.CO;2).

Fan, J., Y. Wang, D. Rosenfeld, and X. Liu, 2016: Review of Aerosol–Cloud Interactions: Mechanisms, Significance, and Challenges. *J. Atmospheric Sci.*, **73**, 4221–4252, <https://doi.org/10.1175/JAS-D-16-0037.1>.

Gardiner, B. A., and J. Hallett, 1985: Degradation of In-Cloud Forward Scattering Spectrometer Probe Measurements in the Presence of Ice Particles. *J. Atmospheric Ocean. Technol.*, **2**, 171–180, [https://doi.org/10.1175/1520-0426\(1985\)002<0171:DOICFS>2.0.CO;2](https://doi.org/10.1175/1520-0426(1985)002<0171:DOICFS>2.0.CO;2).

Goldman, R., 2018: Did a Small Metal Tube Bring Down an Indonesian Airliner? *The New York Times*, October 30.

Greenshields, C., 2017: OpenFOAM User Guide: CFD Direct, Architects of OpenFOAM. *CFD Direct*, <https://cfdirect.com/openfoam/user-guide/> (Accessed March 16, 2021).

Gupta, S., and Coauthors, 2021: Impact of the variability in vertical separation between biomass burning aerosols and marine stratocumulus on cloud microphysical properties over

the Southeast Atlantic. *Atmospheric Chem. Phys.*, **21**, 4615–4635, <https://doi.org/10.5194/acp-21-4615-2021>.

———, G. M. McFarquhar, J. R. O’Brien, M. R. Poellot, D. J. Delene, R. M. Miller, and J. D. Small Griswold, 2022: Factors affecting precipitation formation and precipitation susceptibility of marine stratocumulus with variable above- and below-cloud aerosol concentrations over the Southeast Atlantic. *Atmospheric Chem. Phys.*, **22**, 2769–2793, <https://doi.org/10.5194/acp-22-2769-2022>.

Hansen, J., M. Sato, A. Lacis, and R. Ruedy, 1997: The missing climate forcing. *Philos. Trans. R. Soc. B Biol. Sci.*, **352**, <https://doi.org/10.1098/rstb.1997.0018>.

Johnson, B. T., K. P. Shine, and P. M. Forster, 2004: The semi-direct aerosol effect: Impact of absorbing aerosols on marine stratocumulus. *Q. J. R. Meteorol. Soc.*, **130**, 1407–1422, <https://doi.org/10.1256/qj.03.61>.

King, W. D., 1984: Air Flow and Particle Trajectories around Aircraft Fuselages. I: Theory. *J. Atmospheric Ocean. Technol.*, **1**, 5–13, [https://doi.org/10.1175/1520-0426\(1984\)001<0005:AFAPTA>2.0.CO;2](https://doi.org/10.1175/1520-0426(1984)001<0005:AFAPTA>2.0.CO;2).

———, D. A. Parkin, and R. J. Handsworth, 1978: A Hot-Wire Liquid Water Device Having Fully Calculable Response Characteristics. *J. Appl. Meteorol. Climatol.*, **17**, 1809–1813, [https://doi.org/10.1175/1520-0450\(1978\)017<1809:AHWLWD>2.0.CO;2](https://doi.org/10.1175/1520-0450(1978)017<1809:AHWLWD>2.0.CO;2).

Knollenberg, R. G., 1970: The Optical Array : An Alternative to Scattering or Extinction for Airborne Particle Size Determination. *J. Appl. Meteorol. 1962-1982*, **9**, 86–103.

Lance, S., 2012: Coincidence Errors in a Cloud Droplet Probe (CDP) and a Cloud and Aerosol Spectrometer (CAS), and the Improved Performance of a Modified CDP. *J. Atmospheric Ocean. Technol.*, **29**, 1532–1541, <https://doi.org/10.1175/JTECH-D-11-00208.1>.

Lawson, R. P., 2011: Effects of ice particles shattering on the 2D-S probe. *Atmospheric Meas. Tech.*, **4**, 1361–1381, <https://doi.org/10.5194/amt-4-1361-2011>.

Lawson, R. P., D. O'Connor, P. Zmarzly, K. Weaver, B. Baker, Q. Mo, and H. Jonsson, 2006: The 2D-S (Stereo) Probe: Design and Preliminary Tests of a New Airborne, High-Speed, High-Resolution Particle Imaging Probe. *J. Atmospheric Ocean. Technol.*, **23**, 1462–1477, <https://doi.org/10.1175/JTECH1927.1>.

Liou, K. N., 2002: *An Introduction to Atmospheric Radiation*. Elsevier, 598 pp.

Lohmann, U., and J. Feichter, 2005: Global indirect aerosol effects: a review. *Atmos Chem Phys*, **5**, 715–737, <https://doi.org/10.5194/acp-5-715-2005>.

Moukalled, F., and M. Darwish, 2016: Fluid Flow Computation: Compressible Flows. *The Finite Volume Method in Computational Fluid Dynamics: An Advanced Introduction with OpenFOAM® and Matlab*, F. Moukalled, L. Mangani, and M. Darwish, Eds., *Fluid Mechanics and Its Applications*, Springer International Publishing, 655–690.

———, L. Mangani, and M. Darwish, 2016a: Introduction. *The Finite Volume Method in Computational Fluid Dynamics: An Advanced Introduction with OpenFOAM® and Matlab*, F. Moukalled, L. Mangani, and M. Darwish, Eds., *Fluid Mechanics and Its Applications*, Springer International Publishing, 3–8.

———, ———, and ———, 2016b: The Discretization Process. *The Finite Volume Method in Computational Fluid Dynamics: An Advanced Introduction with OpenFOAM® and Matlab*, F. Moukalled, L. Mangani, and M. Darwish, Eds., *Fluid Mechanics and Its Applications*, Springer International Publishing, 85–101.

———, ———, and ———, 2016c: The Finite Volume Mesh. *The Finite Volume Method in Computational Fluid Dynamics: An Advanced Introduction with OpenFOAM® and Matlab*,

F. Moukalled, L. Mangani, and M. Darwish, Eds., *Fluid Mechanics and Its Applications*, Springer International Publishing, 137–171.

———, ———, and ———, 2016d: The Finite Volume Method. *The Finite Volume Method in Computational Fluid Dynamics: An Advanced Introduction with OpenFOAM® and Matlab*, F. Moukalled, L. Mangani, and M. Darwish, Eds., *Fluid Mechanics and Its Applications*, Springer International Publishing, 103–135.

———, ———, and ———, 2016e: Fluid Flow Computation: Incompressible Flows. *The Finite Volume Method in Computational Fluid Dynamics: An Advanced Introduction with OpenFOAM® and Matlab*, F. Moukalled, L. Mangani, and M. Darwish, Eds., *Fluid Mechanics and Its Applications*, Springer International Publishing, 561–654.

———, ———, and ———, 2016f: Solving the System of Algebraic Equations. *The Finite Volume Method in Computational Fluid Dynamics: An Advanced Introduction with OpenFOAM® and Matlab*, F. Moukalled, L. Mangani, and M. Darwish, Eds., *Fluid Mechanics and Its Applications*, Springer International Publishing, 303–364.

Müller, D., and Coauthors, 2014: Airborne Multiwavelength High Spectral Resolution Lidar (HSRL-2) observations during TCAP 2012: vertical profiles of optical and microphysical properties of a smoke/urban haze plume over the northeastern coast of the US. *Atmospheric Meas. Tech.*, **7**, 3487–3496, <https://doi.org/10.5194/amt-7-3487-2014>.

Norment, H. G., 1988: Three-Dimensional Trajectory Analysis of Two Drop Sizing instruments: PMS* OAP and PMS* FSSP. *J. Atmospheric Ocean. Technol.*, **5**, 743–756, [https://doi.org/10.1175/1520-0426\(1988\)005<0743:TDTAOT>2.0.CO;2](https://doi.org/10.1175/1520-0426(1988)005<0743:TDTAOT>2.0.CO;2).

Redemann, J., and Coauthors, 2021: An overview of the ORACLES (ObseRvations of Aerosols above CLouds and their intEractionS) project: aerosol–cloud–radiation interactions

in the southeast Atlantic basin. *Atmospheric Chem. Phys.*, **21**, 1507–1563, <https://doi.org/10.5194/acp-21-1507-2021>.

Riegel, J., W. Mayer, and Y. van Havre, 2020: FreeCAD.

Spanu, A., M. Dollner, J. Gasteiger, T. P. Bui, and B. Weinzierl, 2020: Flow-induced errors in airborne in situ measurements of aerosols and clouds. *Atmospheric Meas. Tech.*, **13**, 1963–1987, <https://doi.org/10.5194/amt-13-1963-2020>.

Sullivan, C. B., and A. A. Kaszynski, 2019: PyVista: 3D plotting and mesh analysis through a streamlined interface for the Visualization Toolkit (VTK). *J. Open Source Softw.*, **4**, 1450, <https://doi.org/10.21105/joss.01450>.

Twohy, C. H., M. D. Petters, J. R. Snider, B. Stevens, W. Tahnk, M. Wetzell, L. Russell, and F. Burnet, 2005: Evaluation of the aerosol indirect effect in marine stratocumulus clouds: Droplet number, size, liquid water path, and radiative impact. *J. Geophys. Res. Atmospheres*, **110**, D08203, <https://doi.org/10.1029/2004JD005116>.

Twomey, S., 1977: The Influence of Pollution on the Shortwave Albedo of Clouds. *J. Atmospheric Sci.*, **34**, 1149–1152, [https://doi.org/10.1175/1520-0469\(1977\)034<1149:TIOPOT>2.0.CO;2](https://doi.org/10.1175/1520-0469(1977)034<1149:TIOPOT>2.0.CO;2).

Wilcox, D. C., 1993: *Turbulence modeling for CFD*. DCW Industries, Inc, 460 pp.

Wood, R., 2012: Stratocumulus Clouds. *Mon. Weather Rev.*, **140**, 2373–2423, <https://doi.org/10.1175/MWR-D-11-00121.1>.

Wu, W., and G. M. McFarquhar, 2016: On the Impacts of Different Definitions of Maximum Dimension for Nonspherical Particles Recorded by 2D Imaging Probes. *J. Atmospheric Ocean. Technol.*, **33**, 1057–1072, <https://doi.org/10.1175/JTECH-D-15-0177.1>.

2021: Former Boeing 737 MAX Chief Technical Pilot Indicted for Fraud.
<https://www.justice.gov/opa/pr/former-boeing-737-max-chief-technical-pilot-indicted-fraud>
(Accessed February 4, 2023).

APPENDIX A

snappyHexMesh CONFIGURATION FILE

```
/*-----*- C++ -*-----*\
=====
|
\\ / F i e l d      | OpenFOAM: The Open Source CFD Toolbox
\\ / O p e r a t i o n | Website: https://openfoam.org
\\ / A n d          | Version: 7
\\ \ M a n i p u l a t i o n |
\*-----*/
FoamFile
{
  version 2.0;
  format  ascii;
  class  dictionary;
  object  snappyHexMeshDict;
}
// ***** //

// Which of the steps to run
castellatedMesh true;
snap true;
addLayers false;

// Geometry. Definition of all surfaces. All surfaces are of class
// searchableSurface.
// Surfaces are used
// - to specify refinement for any mesh cell intersecting it
// - to specify refinement for any mesh cell inside/outside/near
// - to 'snap' the mesh boundary to the surface
geometry
{
  pmsCanister
  {
    type triSurfaceMesh;
    file "NASA_P3_extendedPylon_CDP_OAP_v5.obj";
  }

  refinementBox
  {
    type searchableBox;
    min (-40.0 -40.0 -40.0);
    max ( 40.0 40.0 -40.0);
    // original refinement box;
    //min ( -1.0 -0.7 0.0);
    //max ( 8.0 0.7 2.5);
  }
}
```

```

}
refinementBox2
{
    type searchableBox;
    min (13.5 2.5 13.0);
    max (15.5 4.0 15.0);
}
};

```

// Settings for the castellatedMesh generation.

```
castellatedMeshControls
```

```
{
```

```
    // Refinement parameters
```

```
    // ~~~~~
```

```
    // If local number of cells is >= maxLocalCells on any processor
```

```
    // switches from refinement followed by balancing
```

```
    // (current method) to (weighted) balancing before refinement.
```

```
    //maxLocalCells 100000;
```

```
    //maxLocalCells 2000000;
```

```
    maxLocalCells 4000000;
```

```
    // Overall cell limit (approximately). Refinement will stop immediately
```

```
    // upon reaching this number so a refinement level might not complete.
```

```
    // Note that this is the number of cells before removing the part which
```

```
    // is not 'visible' from the keepPoint. The final number of cells might
```

```
    // actually be a lot less.
```

```
    //maxGlobalCells 2000000;
```

```
    //maxGlobalCells 40000000;
```

```
    maxGlobalCells 80000000;
```

```
    // The surface refinement loop might spend lots of iterations refining just a
```

```
    // few cells. This setting will cause refinement to stop if <= minimumRefine
```

```
    // are selected for refinement. Note: it will at least do one iteration
```

```
    // (unless the number of cells to refine is 0)
```

```
    //minRefinementCells 20;
```

```
    minRefinementCells 200;
```

```
    // Allow a certain level of imbalance during refining
```

```
    // (since balancing is quite expensive)
```

```
    // Expressed as fraction of perfect balance (= overall number of cells /
```

```
    // nProcs). 0=balance always.
```

```
    maxLoadUnbalance 0.10;
```

```

// Number of buffer layers between different levels.
// 1 means normal 2:1 refinement restriction, larger means slower
// refinement.
nCellsBetweenLevels 3;
//nCellsBetweenLevels 15;

// Explicit feature edge refinement
// ~~~~~

// Specifies a level for any cell intersected by its edges.
// This is a featureEdgeMesh, read from constant/triSurface for now.
features
(
  {
    file "NASA_P3_extendedPylon_CDP_OAP_v5.eMesh";
    level 6;
  }
);

// Surface based refinement
// ~~~~~

// Specifies two levels for every surface. The first is the minimum level,
// every cell intersecting a surface gets refined up to the minimum level.
// The second level is the maximum level. Cells that 'see' multiple
// intersections where the intersections make an
// angle > resolveFeatureAngle get refined up to the maximum level.

refinementSurfaces
{
  pmsCanister
  {
    // Surface-wise min and max refinement level
    level (5 6);

    // Optional specification of patch type (default is wall). No
    // constraint types (cyclic, symmetry) etc. are allowed.
    patchInfo
    {
      type wall;
      inGroups (pmsCanisterGroup);
    }
  }
}

// Resolve sharp angles

```

```

//resolveFeatureAngle 30;
//resolveFeatureAngle 10;
resolveFeatureAngle 3;

// Region-wise refinement
// ~~~~~

// Specifies refinement level for cells in relation to a surface. One of
// three modes
// - distance. 'levels' specifies per distance to the surface the
// wanted refinement level. The distances need to be specified in
// descending order.
// - inside. 'levels' is only one entry and only the level is used. All
// cells inside the surface get refined up to the level. The surface
// needs to be closed for this to be possible.
// - outside. Same but cells outside.

refinementRegions
{
    refinementBox
    {
        mode inside;
        levels ((1E15 4));
    }
}

// Mesh selection
// ~~~~~

// After refinement patches get added for all refinementSurfaces and
// all cells intersecting the surfaces get put into these patches. The
// section reachable from the locationInMesh is kept.
// NOTE: This point should never be on a face, always inside a cell, even
// after refinement.
locationInMesh (3.0001 3.0001 0.43);
//locationInMesh (0.0 0.0 4.5);

// Whether any faceZones (as specified in the refinementSurfaces)
// are only on the boundary of corresponding cellZones or also allow
// free-standing zone faces. Not used if there are no faceZones.
//allowFreeStandingZoneFaces true;
allowFreeStandingZoneFaces false;
}

```

```

// Settings for the snapping.
snapControls
{
  //- Number of patch smoothing iterations before finding correspondence
  // to surface
  nSmoothPatch 3;

  //- Relative distance for points to be attracted by surface feature point
  // or edge. True distance is this factor times local
  // maximum edge length.
  tolerance 1.0;

  //- Number of mesh displacement relaxation iterations.
  //nSolveIter 30;
  nSolveIter 300;

  //- Maximum number of snapping relaxation iterations. Should stop
  // before upon reaching a correct mesh.
  nRelaxIter 5;

  // Feature snapping

  //- Number of feature edge snapping iterations.
  // Leave out altogether to disable.
  nFeatureSnapIter 50;

  //- Detect (geometric only) features by sampling the surface
  // (default=false).
  implicitFeatureSnap false;

  //- Use castellatedMeshControls::features (default = true)
  explicitFeatureSnap true;

  //- Detect points on multiple surfaces (only for explicitFeatureSnap)
  //multiRegionFeatureSnap false;
  multiRegionFeatureSnap false;
}

// Settings for the layer addition.
addLayersControls
{
  // Are the thickness parameters below relative to the undistorted
  // size of the refined cell outside layer (true) or absolute sizes (false).
  relativeSizes true;

  // Per final patch (so not geometry!) the layer information

```

```

layers
{
  "pmsCanister.*"
  {
    nSurfaceLayers 1;
  }
}

// Expansion factor for layer mesh
expansionRatio 1.0;

// Wanted thickness of final added cell layer. If multiple layers
// is the thickness of the layer furthest away from the wall.
// Relative to undistorted size of cell outside layer.
// See relativeSizes parameter.
finalLayerThickness 0.3;

// Minimum thickness of cell layer. If for any reason layer
// cannot be above minThickness do not add layer.
// Relative to undistorted size of cell outside layer.
minThickness 0.1;

// If points get not extruded do nGrow layers of connected faces that are
// also not grown. This helps convergence of the layer addition process
// close to features.
// Note: changed(corrected) w.r.t 17x! (didn't do anything in 17x)
nGrow 0;

// Advanced settings

// When not to extrude surface. 0 is flat surface, 90 is when two faces
// are perpendicular
featureAngle 60;

// At non-patched sides allow mesh to slip if extrusion direction makes
// angle larger than slipFeatureAngle.
slipFeatureAngle 30;

// Maximum number of snapping relaxation iterations. Should stop
// before upon reaching a correct mesh.
nRelaxIter 3;

// Number of smoothing iterations of surface normals
nSmoothSurfaceNormals 1;

// Number of smoothing iterations of interior mesh movement direction

```

```

nSmoothNormals 3;

// Smooth layer thickness over surface patches
nSmoothThickness 10;

// Stop layer growth on highly warped cells
maxFaceThicknessRatio 0.5;

// Reduce layer growth where ratio thickness to medial
// distance is large
maxThicknessToMedialRatio 0.3;

// Angle used to pick up medial axis points
// Note: changed(corrected) w.r.t 17x! 90 degrees corresponds to 130 in 17x.
minMedianAxisAngle 90;

// Create buffer region for new layer terminations
nBufferCellsNoExtrude 0;

// Overall max number of layer addition iterations. The mesher will exit
// if it reaches this number of iterations; possibly with an illegal
// mesh.
nLayerIter 50;
}

// Generic mesh quality settings. At any undoable phase these determine
// where to undo.
meshQualityControls
{
    #include "meshQualityDict"
}

// Advanced

// Write flags
writeFlags
(
    scalarLevels
    layerSets
    layerFields // write volScalarField for layer coverage
);

// Merge tolerance. Is fraction of overall bounding box of initial mesh.

```

```
// Note: the write tolerance needs to be higher than this.  
mergeTolerance 1e-6;
```

```
// *****//
```

APPENDIX B

thermoPhysicalProperties CONFIGURATION FILE

```
/*-----* C++ *-----*\
=====
\\ / F ield      | OpenFOAM: The Open Source CFD Toolbox
\\ / O peration  | Website: https://openfoam.org
\\ / A nd        | Version: 7
\\ \ M anipulation |
\*-----*/
FoamFile
{
    version    2.0;
    format     ascii;
    class      dictionary;
    location   "constant";
    object     thermoPhysicalProperties;
}
// *****

thermoType
{
    type        hePsiThermo;
    mixture     pureMixture;
    transport   const;
    thermo      hConst;
    equationOfState perfectGas;
    specie      specie;
    energy      sensibleInternalEnergy;
}

mixture // air at room temperature (293 K)
{
    specie
    {
        molWeight 28.9;
    }
    thermodynamics
    {
        Cp        1005;
        Hf        0;
    }
    transport
```

```
{
  mu    1.82e-05;
  Pr    0.71;
}
// ***** //
```

APPENDIX C

BOUNDARY CONDITIONS CONFIGURATION FILES

(0 DIRECTORY)

```
/*-----*- C++ -*-----*\
=====
\ \ / F i e l d      | OpenFOAM: The Open Source CFD Toolbox
\ \ / O p e r a t i o n | Website: https://openfoam.org
\ \ / A n d           | Version: 7
\ \ V M a n i p u l a t i o n |
\*-----*/
FoamFile
{
  version 2.0;
  format  ascii;
  class  volVectorField;
  object  U;
}
// ***** //
Uinlet      (120 0 0);

dimensions  [0 1 -1 0 0 0 0];

internalField  uniform $Uinlet;

boundaryField
{
  freestream
  {
    type      freestreamVelocity;
    freestreamValue  uniform $Uinlet;
    value      uniform $Uinlet;
  }

  wall
  {
    type      noSlip;
  }

  #includeEtc "caseDicts/setConstraintTypes"
}
}
```

// ***** //

```

/*-----*- C++ -*-----*\
=====
\ \ / F i e l d      | OpenFOAM: The Open Source CFD Toolbox
\ \ / O p e r a t i o n | Website: https://openfoam.org
\ \ / A n d          | Version: 7
\ \ M a n i p u l a t i o n |
\*-----*/
FoamFile
{
  version 2.0;
  format  ascii;
  class  volScalarField;
  object  p;
}
// ***** //
pOut      9e4;

dimensions  [1 -1 -2 0 0 0 0];

internalField  uniform $pOut;

boundaryField
{
  freestream
  {
    type      freestreamPressure;
    freestreamValue  uniform $pOut;
  }

  wall
  {
    type      zeroGradient;
  }

  #includeEtc "caseDicts/setConstraintTypes"
}

```

```

// *****

/*-----* C++ *-----*\
=====
|
\\ / Field | OpenFOAM: The Open Source CFD Toolbox
\\ / Operation | Website: https://openfoam.org
\\ / And | Version: 7
\\ Manipulation |
\*-----*/

FoamFile
{
    version 2.0;
    format ascii;
    class volScalarField;
    object T;
}
// ***** //
Tinlet 306;

dimensions [0 0 0 1 0 0 0];

internalField uniform $Tinlet;

boundaryField
{
    freestream
    {
        type inletOutlet;
        inletValue uniform $Tinlet;
        value $inletValue;
    }

    wall
    {
        type zeroGradient;
        //type fixedValue;
        //wallValue uniform $Tinlet;
        //value $wallValue;
    }

    #includeEtc "caseDicts/setConstraintTypes"
}

```

```

// *****

/*-----* C++ *-----*\
=====
|
\\ / Field | OpenFOAM: The Open Source CFD Toolbox
\\ / Operation | Website: https://openfoam.org
\\ / And | Version: 7
\\ Manipulation |
\*-----*/

FoamFile
{
    version 2.0;
    format ascii;
    class volScalarField;
    object omega;
}
// ***** //
omegaInlet 400000;

dimensions [0 0 -1 0 0 0];

internalField uniform $omegaInlet;

boundaryField
{
    freestream
    {
        type inletOutlet;
        inletValue uniform $omegaInlet;
        value uniform $omegaInlet;
    }

    wall
    {
        type omegaWallFunction;
        value uniform $omegaInlet;
    }

    #includeEtc "caseDicts/setConstraintTypes"
}

// ***** //

```

```

/*----- C++ -----*\
=====
\ \ / F i e l d   | OpenFOAM: The Open Source CFD Toolbox
\ \ / O p e r a t i o n   | Website: https://openfoam.org
\ \ / A n d   | Version: 7
\ \ V M a n i p u l a t i o n   |
\*-----*/
FoamFile
{
    version    2.0;
    format     ascii;
    class      volScalarField;
    object    k;
}
// ***** //
kInlet      10.00;

dimensions  [0 2 -2 0 0 0 0];

internalField  uniform $kInlet;
//internalField  uniform 100;

boundaryField
{
    freestream
    {
        type      inletOutlet;
        inletValue  uniform $kInlet;
        value      uniform $kInlet;
    }

    wall
    {
        type      kqRWallFunction;
        value      uniform $kInlet;
    }

    #includeEtc "caseDicts/setConstraintTypes"
}
// ***** //

```

APPENDIX D

SYSTEM DIRECTORY CONFIGURATION FILES

```
/*-----*- C++ -*-----*\
=====
|
\\ / F ield      | OpenFOAM: The Open Source CFD Toolbox
\\ / O peration  | Website: https://openfoam.org
\\ / A nd        | Version: 7
\\ \ M anipulation |
\*-----*/
FoamFile
{
  version 2.0;
  format  ascii;
  class   dictionary;
  object controlDict;
}
// ***** //

application rhoSimpleFoam;

startFrom    startTime;

startTime    0;

stopAt       endTime;

endTime      10000;

deltaT       1;

writeControl timeStep;

writeInterval 2000;

purgeWrite   0;

//writeFormat  ascii;
writeFormat  binary;

writePrecision 6;
```

```
writeCompression off;

timeFormat    general;

timePrecision 6;

runTimeModifiable true;

functions
{
  #includeFunc MachNo
  #includeFunc residuals
  #includeFunc cuttingPlane
}

// ***** //
```

```

/*-----*- C++ -*-----*\
===== |
\\ / F i e l d      | OpenFOAM: The Open Source CFD Toolbox
\\ / O p e r a t i o n | Website: https://openfoam.org
\\ / A n d          | Version: 7
  \\ V M a n i p u l a t i o n |
\*-----*/
FoamFile
{
  version 2.0;
  format  ascii;
  class  dictionary;
  object  blockMeshDict;
  Does anyone actually read dissertations?
}
// ***** //

domain
{
  // Hex A
  xMin -150;
  xMax  50;
  yMin -100;
  yMax 100;
  zMin -100;
  zMax 100;

  // Number of cells
  zCells 200; // aerofoil to far field
  xCells 200; // sum of previous spots
  yCells 200; // adding the dimension
}

vertices
(
  // Hex A
  ($domain.xMin $domain.yMin $domain.zMin) // vertice 0
  ($domain.xMax $domain.yMin $domain.zMin) // vertice 1
  ($domain.xMax $domain.yMax $domain.zMin) // vertice 2
  ($domain.xMin $domain.yMax $domain.zMin) // vertice 3
  ($domain.xMin $domain.yMin $domain.zMax) // vertice 4
  ($domain.xMax $domain.yMin $domain.zMax) // vertice 5
  ($domain.xMax $domain.yMax $domain.zMax) // vertice 6
  ($domain.xMin $domain.yMax $domain.zMax) // vertice 7
);

```

```

blocks
(
  hex (0 1 2 3 4 5 6 7) ($domain.xCells $domain.yCells $domain.zCells) simpleGrading
(1 1 1)
);

edges
(
);

boundary
(
  inlet
  {
    type patch;
    inGroups (freestream);
    faces
    (
      // Hex A
      (0 4 7 3)
    );
  }

  outlet
  {
    type patch;
    inGroups (freestream);
    faces
    (
      // Hex B
      (1 5 6 2)
    );
  }

  frontAndBack
  {
    type patch;
    inGroups (freestream);
    faces
    (
      // front
      (0 4 5 1)
      // back
      (3 7 6 2)
    );
  }
}

```

```
topAndBottom
{
  type patch;
  inGroups (freestream);
  faces
  (
    // top
    (4 7 6 5)
    // bottom
    (0 3 2 1)
  );
}
);

// ***** //
```

```

/*-----* C++ *-----*\
=====
\\ / F i e l d   | OpenFOAM: The Open Source CFD Toolbox
\\ / O p e r a t i o n   | Website: https://openfoam.org
\\ / A n d   | Version: 7
\\ \ M a n i p u l a t i o n   |
\*-----*/
FoamFile
{
  version 2.0;
  format ascii;
  class dictionary;
  object fvSolution;
}
// ***** //

solvers
{
  p
  {
    solver GAMG;
    smoother GaussSeidel;
    tolerance 1e-6;
    relTol 0.01;
  }

  "(U|k|omega|e)"
  {
    solver PBiCGStab;
    preconditioner DILU;
    tolerance 1e-6;
    relTol 0.1;
  }
}

SIMPLE
{
  residualControl
  {
    p 1e-4;
    U 1e-4;
    "(k|omega|e)" 1e-4;
  }

  nNonOrthogonalCorrectors 0;
  pMinFactor 0.1;
}

```

```
pMaxFactor 2;
}

relaxationFactors
{
  fields
  {
    p      0.7;
    rho    0.01;
  }
  equations
  {
    U      0.3;
    e      0.7;
    "(k|omega)" 0.7;
  }
}

// ***** //
```

```

/*-----* C++ *-----*\
=====
\ \ / F i e l d      | OpenFOAM: The Open Source CFD Toolbox
\ \ / O p e r a t i o n | Website: https://openfoam.org
\ \ / A n d          | Version: 7
\ \ V M a n i p u l a t i o n |
\*-----*/
FoamFile
{
  version 2.0;
  format  ascii;
  class  dictionary;
  object fvSchemes;
}
// *****

ddtSchemes
{
  default  steadyState;
}

gradSchemes
{
  default  Gauss linear;

  limited  cellLimited Gauss linear 1;
  grad(U)  $limited;
  grad(k)  $limited;
  grad(omega) $limited;
}

divSchemes
{
  default  none;

  div(phi,U)  bounded Gauss linearUpwind limited;

  turbulence  bounded Gauss upwind;
  energy      bounded Gauss linearUpwind limited;

  div(phi,k)  $turbulence;
  div(phi,omega) $turbulence;

  div(phi,e)  $energy;
  div(phi,K)  $energy;
  div(phi,Ekp) $energy;
}

```

```

div(phid,p) Gauss upwind;
div((phi|interpolate(rho)),p) bounded Gauss upwind;

div(((rho*nuEff)*dev2(T(grad(U)))) Gauss linear;
}

laplacianSchemes
{
  default Gauss linear corrected;
}

interpolationSchemes
{
  default linear;
}

snGradSchemes
{
  default corrected;
}

wallDist
{
  method meshWave;
}

// ***** //

```

```

/*-----*- C++ -*-----*\
=====
\ \ / F i e l d      | OpenFOAM: The Open Source CFD Toolbox
\ \ / O p e r a t i o n | Website: https://openfoam.org
\ \ / A n d          | Version: 7
\ \ V M a n i p u l a t i o n |
\*-----*/
FoamFile
{
  version 2.0;
  format  ascii;
  class  dictionary;
  object  surfaceFeaturesDict;
}
// ***** //

surfaces ("NASA_P3_extendedPylon_CDP_OAP_v5.obj");

// Identify a feature when angle between faces < includedAngle
includedAngle 15;

subsetFeatures
{
  // Keep nonManifold edges (edges with >2 connected faces)
  nonManifoldEdges no;

  // Keep open edges (edges with 1 connected face)
  openEdges yes;
}

// ***** //

```

```

/*-----*- C++ -*-----*\
=====
\ \ / F i e l d      | OpenFOAM: The Open Source CFD Toolbox
\ \ / O p e r a t i o n | Website: https://openfoam.org
\ \ / A n d          | Version: 7
\ \ M a n i p u l a t i o n |

```

File: singleGraph

Description

Writes graph data for specified fields along a line, specified by start and end points.

```

\*-----*/

```

```

start (10 2.72 13.75);
end (20.0 2.72 13.75);
fields (U p T rho Ma total(p));

```

```

// Sampling and I/O settings
#includeEtc "caseDicts/postProcessing/graphs/sampleDict.cfg"

```

```

// Override settings here, e.g.
setConfig
{
    type lineCell;
    axis xyz; // x, y, z, xyz
}

```

```

// Must be last entry
#includeEtc "caseDicts/postProcessing/graphs/graph.cfg"

```

```

// ***** //

```